A THREE DIMENSIONAL IMAGING SONAR

by

PETER BRIAN RUNCIMAN

Submitted in partial fulfilment of the
requirements for the degree of
Master of Science in Engineering

UNIVERSITY OF CAPE TOWN

September 1986

ABSTRACT

Most three dimensional imaging systems require two dimensional matrix arrays of transducer elements and sophisticated beamforming circuitry. This dissertation describes a much simpler technique based upon phase difference measurements of incident waveforms. The limitations of such a simplified approach are shown to be much less of a constraint than might be supposed on first consideration.

ACKNOWLEDGEMENTS

I would like to take this opportunity to thank Professor P.N. Denbigh, my supervisor, for his unreserved guidance and support throughout my investigations.

Thanks are also extended to the Institute for Maritime Technology for the use of their tank facility and their willing contribution to the creation of this document.

Finally I would like to extend my gratitude to those individuals, especially Adrian Horwitz, for their assistance in this project.

TABLE OF CONTENTS

LIST OF ILLUSTRATIONS

CHAPTER 1

INTRODUCTION

Low visibility is a condition frequently encountered in underwater situations hampering the activities of divers and remotely piloted vehicles. Efforts to probe the turbid and saline water of the sea with light and radio waves are frustrated by the high attenuation experienced for electro-magnetic energy.

Alternatively sound, for moderate frequencies, propagates virtually unattenuated in water, making it the preferred choice of radiated energy used in underwater instruments designed for communication, telemetry and imaging.

This dissertation describes an active three dimensional imaging sonar that was built and tested. Although physically small and inexpensive to produce, this short range sonar provides a real-time three dimensional stereoscopic display.

Unlike most three dimensional imaging sonar systems that require two dimensional matrix arrays of transducer elements and complex beamforming circuitry, this system employs a much simpler technique based upon phase difference measurements of incident waveforms.

Behind this simplified approach is the assumption that the echo field can be regarded as a series of discrete point scatterers or highlights. Theoretical substantiation is provided, along with photographed images obtained for water trials, supporting this assumption even under complex multiple target conditions.

Presented also in this document are the results of investigations into techniques for transducer evaluation and matching, low noise preamplifier design, phase measurement and three dimensional displays. In the appendix the reader will find a full set of circuit diagrams for the complete sonar system.

A published paper giving details of the three dimensional, 3-D, imaging sonar system and obtained results was presented at the Ultrasonics International 85 Conference (Reference 1) by its co-author, Professor P.N. Denbigh.

CHAPTER 2

CLIPPED-SIGNAL PHASE-ONLY SONARS

2.1. Introduction

Since World War II, the application of digital techniques in both radar and sonar systems has increased dramatically (Reference 2).

These applications can be placed in three main categories:

(a) Firstly, digital computers are used for the control of systems, for example tracking, where the function of data handling is considered rather than signal processing.

(b) Secondly, digitally realised signal processing elements are taking precedence over their analogue counterparts with advantages in cost, flexibility and stability of operation. Examples of this category include delay lines and correlators.

(c) Finally, the output of individual sensors are being digitally encoded and stored for subsequent processing. This has made the technique of aperture synthesis feasible, which is used extensively in echo seismology and radio astronomy.

The system described in this dissertation uses a sonar signal processing technique similar to the last category in that the output of the individual transducers is encoded directly into a digital form. This digitisation process, which is performed by infinitely clipping the output waveform from each transducer, shows advantages over conventional systems by eliminating two of the most difficult problems encountered in pulsed sonars, namely:

(a) It avoids the wide dynamic range of signal amplitudes experienced in active sonar, which at times exceeds 70 dB (Reference 3), thus obviating the implementation of time varying gain or automatic gain control in the input receiving stages.

(b) The subsequent encoding process, which samples the phase between signals on adjacent transducers, is reduced to a simple digital gating operation.

A small hard-wired data processor performs target detection on the temporarily stored phase samples and outputs the bearings of the detected targets to a display.

In the following subsections this work is placed in context with previous investigations into the application of clipped-signal processing in the field of sonar and signal processing.

2.2. Historical Overview of Clipped-Signal Processing : General

In 1952 Huggins (Reference 4) published details of a "phase filter" implemented with clipped-signal processing. Its purpose was to detect signals in the time domain against background noise and was achieved by observing the fluctuation in the periods of a time waveform about their mean.

Middelton (Reference 5), examined the performance of the phase filter and noted the application of this technique to systems where the absolute value of the signal plus background noise is subject to large dynamic range.

Webb et al (Reference 6), further demonstrated the viability of clipped-signal processing in an apparatus used to analyse the frequency spectra of heart sounds.

An early example of spatial signal detection is provided by Piggot et al (Reference 7) in their scanned line hydrophone method of determining the angle of arrival of sound in water. In this case the principle of the phase filter can be extended to the detection of spatial signals by observing the consistency of the measured phase sampled over an array aperture. (It is interesting to note that the DIMUS system (Reference 8), although developed much later, operates in a similar manner.)

Although the operation of the 3-D sonar can be regarded as a synthesis of the many existing notions mentioned above, its development was most influenced by the work performed at Birmingham University on the "Digital Sonar System".

The theoretical possibility of the digital sonar system was first examined by Nairn (Reference 9) in 1964 who later published results of tests carried out with a practical system (Reference 10). Further contributions to the development and evaluation of this system were provided by Griffiths, Creasy, Braithwaite and Hudson (Reference 11, 12 and 13).

Since the work presented in this dissertation has a great deal in common with Nairn's system, a thorough examination of its operation is presented in the following subsection.

2.3. Historical Overview of Clipped-Signal Processing : The Digital Sonar

The digital sonar is critically dependant on the single hypothesis that sufficient information can be gleaned from the echo field by treating it as a series of localised point targets or highlights, and discarding all other information.

In operation, this system differs from normal sonars in that bearing is measured by a phase sampling technique rather than the classical maximum amplitude response method.

Nairn's experimental system insonifies a broad sector with a narrow-band pulsed 47,5 kHz transmission. As the sound pulse travels outward, targets intersecting the annulus of the sector insonified at any moment in time produce an echo signal which is a copy of the transmission pulse.

Figure 2.1 shows a line array of seven equally spaced transducers receiving a single echo signal in the farfield. The phase difference ϕ_i between the sinusoidal outputs from each of the six adjacent transducer pairs is measured and the spatial deviation function D_s for these samples is calculated.

D_s is defined as;

$$D_s = \frac{1}{6} \sum_{1}^{6} |\phi_i - \bar{\phi}| \qquad (2.1)$$

where $\bar{\phi}$ is the mean phase difference, given by;

$$\bar{\phi} = \frac{1}{6} \sum_{1}^{6} \phi_i \ . \qquad (2.2)$$

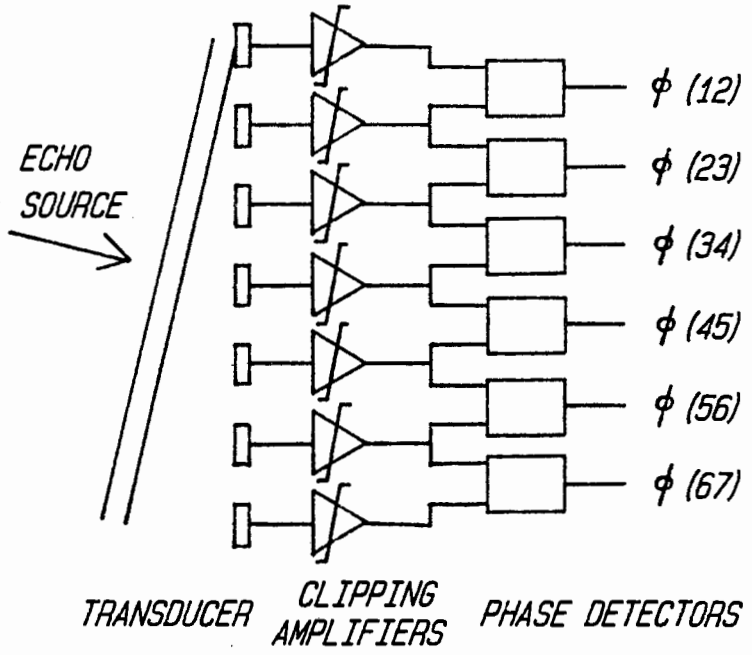

Figure 2.1: Schematic block diagram of the digital sonar system.

Obviously, for instances when a single noise-free echo signal is present at the array, there would be no deviation in the measured phases from the mean phase difference. In this case D_s would be zero.

If however, the signals at the individual transducers are contaminated with noise or multiple echoes, then D_s will assume a positive number. The magnitude of D_s is a measure of these perturbations and thus affords a method of detecting the presence of a single echo at the array. A threshold is placed on the values of D_s below which the signal is deemed suitable for further acquisition.

Samples of this phase-difference information are taken every 63 μs. Within this period the samples are encoded into digital form and the spatial deviation function D_s evaluated and subjected to the above primary threshold. The source bearing is immediately calculated from the average phase difference of the sample.

On the occurrence of a sample passing the primary threshold, a data-collection interval is initiated that continues for as long as successive samples satisfy it. When the primary threshold fails the accumulated bearing information is subjected to a secondary threshold before accepting the target for display.

The secondary threshold requires that at least a given minimum number of successive samples pass the primary threshold, thereby ensuring that a strong enough signal is received for long enough to ensure an accurate bearing measurement.

If the data is accepted then a spot of preset duration and brilliance is painted on the display screen at the sample bearing and range, which is indicated by the normal time-base sweep.

Encouraging results were reported for water trials of the digital sonar. While the system was successful in discarding noise samples, it was necessary to greatly relax the detection threshold levels in order to avoid excessive target rejection.

It was with the view to enhancing the probability of single target conditions, rather than excessive target rejection by stringent threshold hierarchies, that the 3-D sonar approached target detection.

2.4. System Overview

2.4.1. Introduction

The 3-D imaging sonar is a phase-only sonar departing from classical sonar operation in a similar manner to the digital sonar.

However, a major difference between these systems is that the 3-D sonar can make measurements of elevation, as well as of bearing and range, while using a simplified logic algorithm operating on fewer transducers. Furthermore it recognises that the greatest problem is not detection in the presence of noise, but the overlapping echoes from multiple targets. An attempt is made in this system to increase the likelihood of single target conditions.

2.4.2. Principle of Operation

Like Nairn's system the basic principle of this pulsed sonar lies in treating the sound field as a series of point targets or highlights. The location of these points is determined solely by the phase information of the narrow-band echo signal.

The angles of the incident wavefront are determined by measuring the phase difference between the sinusoidal outputs of two closely spaced adjacent transducer elements. Two azimuth measurements are made using two parallel transducer pairs (AB and CD in Figure 2.2). Similarly, two orthogonal transducer (AC and BD) determine the elevation.

The phase differences are measured continuously as a function of time and, in this way, the angles of the targets in successive range cells are determined one after the other as the transmitted pulse propagates outwards. The average of the two azimuth measurements and the average of the two elevation measurements are then displayed in real time on a CRT.

Up to this point the system described is exceedingly simple relative to most other 3-D imaging systems but, since the system can only determine the angle of incidence of a single wavefront at any time, there is a requirement that there be only one dominant echo source in each range cell. The ability to extract single point target echoes and reject overlapping or very weak echoes is the function of a data processor operating on the bearing measurements.

The above constraint tends, however, to be much less of a disadvantage than would be supposed from an experience of optical images. This is due to the nature of echo formation (Reference 14) where, due to the much larger wavelength, many large solid bodies appear only as a series of discrete echoes originating from various cross-sectional discontinuities of the body. Chapter 3 enlarges on this aspect and demonstrates with example the highly specular nature of targets which may well yield only one dominant echo in any range cell.

It is also interesting to note that the image detail is sometimes better than expected. When there are multiple echoes within a range cell, the individual highlights may scintillate independently, such that only one echo is dominant, but that the dominant echo changes with time. This could come about due to fluctuations in the medium or due to small movements in the transducer or target orientations (Reference 13).

The data processor performs echo discrimination based on four criteria that must be simultaneously met, in any range cell, for a target to be displayed.

(a) Range Gate:

This simplifies the image by limiting targets displayed to those lying between an inner and outer range radius and is easily realised for active sonars by a simple time blanking signal.

(b) Variations in azimuth measurements:

The existence of the required singe wavefront condition is checked by ensuring that the two azimuth measurements, as measured by the two parallel transducer pairs thus orientated, are closely the same. An adjustable threshold is applied to set a maximum permissible difference.

(c) Variations in elevation measurements:

Similarly, multiple wavefront conditions arising from targets at the same range but with different elevation are rejected.

(d) Backscatter amplitude threshold:

In determining the phase, the outputs of the individual transducers are infinitely clipped and the phase digitised by gated counters. However, before the clipping stage, where all amplitude information is lost, there is a linear front-end amplifier of nominal but constant gain. An output, taken from one channel at this point, is envelope detected and compared against an amplitude threshold set a little above the noise voltage. This serves to impose a quality threshold on the angle information measured for signals whose signal-to-noise ratio would prohibit reliable and accurate phase measurement.

The operation of the whole system is summarised by the schematic diagrams shown in Figure 2.3(a) and Figure 2.3(b).

In order to minimise degradation in image quality by excessive target rejection, short transmission pulses were used thus enhancing the likelihood of a single target condition in each range cell. In the experimental system a 20 μs pulse duration with centre frequency of 490 kHz was used.

Both the azimuth and elevation bearings of detected targets are shown along with the range information in a synthetically generated stereoscopic pair of images giving the observer a three dimensional "as the eye would see it" display.

2.4.3. Conclusion

Chapter 4 describes, in detail, the practical realisation of the 3-D sonar system while Appendix B gives full circuit diagrams and explains its electronic operation. Results obtained for water trials of the system are presented in Chapter 5 demonstrating the sonar's performance for situations not necessarily exhibiting the ideal single target conditions.

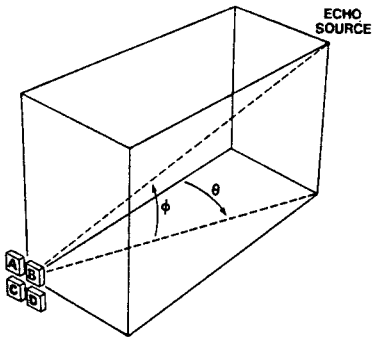

Figure 2.2: Transducer geometry.

a)

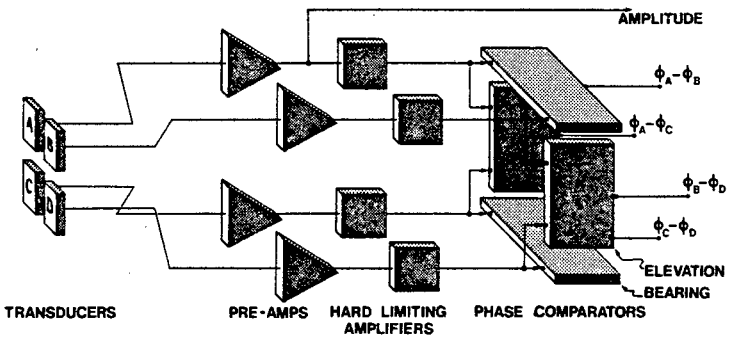

b)

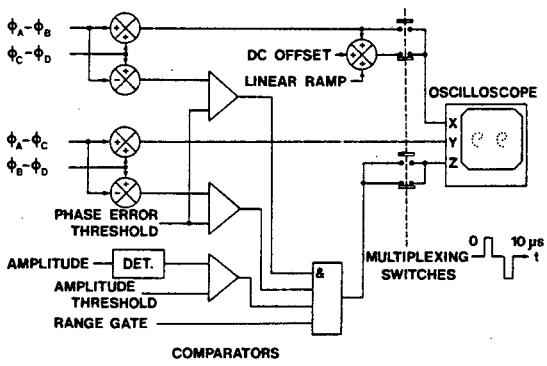

Figure 2.3: Schematic block diagram of the 3-D imaging sonar system.

CHAPTER 3

ECHO FORMATION

3.1. Introduction

Urick (Reference 15) introduces echo formation as the subject of catacoustics, defined as "that part of acoustics which treats reflected sound or echoes."

In this chapter, it will be shown theoretically that the backscatter from solid objects is in general composed of a small number of highlights. This highly specular response of targets to ultrasonic waves will often give rise to only one dominant echo from each range cell at any instant. Thus the limitation imposed for this system by the required single target condition, would tend to place less of a constraint on its operation than would initially be assumed.

A comparison is made of the expected imaging performance of this system to the performance of other systems based on a knowledge of the structure of the returning echo.

3.2. Theory of Echo Formation

Freedman (Reference 14) examined the backscatter from rigid bodies insonified by an incident pulse of ultrasonic sound. He showed that the echo was composed of a number of discrete pulses, each a replica of the transmission pulse, and hence termed an "image pulse".

An image pulse is generated whenever there is a discontinuity with respect to range r in;

$$W^{(n)}(r) = \frac{d^{(n)} W(r)}{dr^{(n)}} \qquad (3.1)$$

where W(r) is the solid angle subtended by that part of the scattering body within range r of the transmitter/receiver transducers. (n may be zero or any positive integer.)

To comply with the conditions of Freedman's analysis, the following must be assumed:

(i) The rigid body is seen to be immersed in an ideal fluid medium.

(ii) The illuminating sound is composed of small amplitude acoustic waves.

(iii) The component of "creeping waves" is ignored for the small wavelength considered.

(iv) The spectrum of the transmission signal does not contain appreciable components outside a bandwidth which is small compared with the mean transmission frequency f_0.

Apart from (iv) above, the transmission pulse is deemed to be an amplitude modulated pulse with an arbitrary envelope v(t).

Let r_l and r_f be the range of the nearest and the furtherest directly insonified part of the scattering body. The echo is then given by the summation:

$$E = \sum_{g=l}^{f} Eg \qquad (3.2)$$

Where Eg is the image pulse, at range r_g, at which a finite discontinuity occurs in Equation 3.1, and is given by;

$$Eg = i \frac{Mg}{\lambda} \exp [- i2k (r_g - r_l)] \sum_{n=0}^{\infty} \frac{D(W, g, n)}{(i2k)^n} \qquad (3.3)$$

where

$$Mg = V(t - \frac{2r_g}{c}) \text{ P.H. } \exp [i (\omega t - 2kr_l)] . \qquad (3.4)$$

In the above;

λ_m is the mean wavelength, ($k = \frac{2\pi}{\lambda_m}$)

P, the transmission sensitivity, set to unity

H, the receiver sensitivity, set to unity

c, the velocity of sound in the medium and

D(W, g, n), the discontinuity in $W^{(n)}(r)$, at range r_g .

Provided that r_m, the mean range, satisfies;

$$r_m \gg r_f - r_l \tag{3.5}$$

then Equation 3.3 simplifies to:

$$Eg = i \frac{Mg}{\lambda r_m^2} \exp[-i2k(r_g - r_l)] \sum_{n=0}^{\infty} \frac{D(A, g, n)}{(i2k)^n} \tag{3.6}$$

Where D(A, g, n) is the discontinuity in $A^{(n)}(r)$ at range r_g and A(r) is the area of projection towards the transducers of the scattering body within range r.

In applying this technique to practical examples, the transducers are assumed to be sufficiently removed from the scattering bodies to satisfy Equation 3.5. Furthermore, the waves impinging on the targets are assumed to locally approximate plane wave fronts, of uniform intensity, over the whole target crossection.

3.3. Examples of Echo Structure and a Comparison in Resulting Images

3.3.1. Table Tennis Ball

Figure 3.1 illustrates the echo formation for a table tennis ball insonified by a short pulse of high frequency sound.

INCIDENT SOUND PULSE		THIS CASE $r_f = r_2$		
(a) TABLE TENNIS BALL	n	$A^n(r)$ $r_1 \le r \le r_2$	D(A, 1, n)	D(A, 2, n)
(b) $A^0(r)$	0	$\pi a^2 [1-(\frac{a-(r-r_1)}{a})^2]$	0	0
(c) $A^1(r)$	1	$2\pi [a-(r-r_1)]$	$-2\pi a$	0
(d) $A^2(r)$	2	-2π	2π	-2π
(e) $A^3(r)$	3	0	0	0
(f) E(t)				
(g) E(t)				

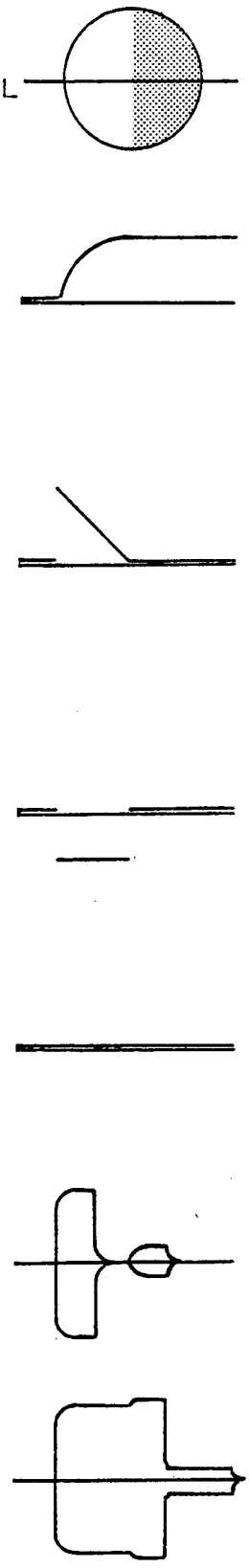

Figure 3.1: Echo formation for a table tennis ball.

The returning echo is comprised of two image pulses originating at ranges r_1 and r_2. From the table in Figure 3.1 the resulting image echo strength generated at r_1 can be found by substituting into Equation 3.6:

$$\frac{E_1}{M_1} = i \frac{1}{\lambda r_m^2} \exp[-i2k(r_f - r_1)][\frac{-2\pi a}{i2k} + \frac{2\pi}{(i2k)^2}]$$

$$= i \frac{1}{\lambda r_m^2} (-\frac{2\pi a}{2ki})[1 - \frac{1}{2aki}]$$

Substituting $k = \frac{2\pi}{\lambda}$:

$$\frac{E_1}{M_1} = -\frac{1}{r_m^2} \frac{a}{2}[1 + \frac{i}{2ak}] \quad (3.7)$$

Similarly, the image echo strength from r_2 is:

$$\frac{E_2}{M_2} = i \frac{1}{r_m^2} \exp[-i2ak] \frac{1}{4k} \quad (3.8)$$

For the above;

$$M_1 = V(t - \frac{2r_1}{c}) \exp[i(\omega t - 2kr_1)] \quad (3.9)$$

and

$$M_2 = V(t - \frac{2r_2}{c}) \exp[i(\omega t - 2kr_1)] . \quad (3.10)$$

where $r_2 = r_1 + a$.

Figure 3.1(F) gives the schematic echo structure for non-overlapping image pulses. If however, the duration of the transmission pulse is greater than $(t_2 - t_1)$, then the overlapping regions of the image pulses interfere according to their relative phases. Figure 3.1(G) shows such a pair of interfering image pulses.

For a table tennis ball imaged by a 490 kHz sonar system;

$a = 18.75$ mm

$k = 2053$ RAD M^{-1}

Substituting these values into Equation 3.7 and Equation 3.8 yields:

$$\left|\frac{E_1}{M_1}\right| = \left| -\frac{1}{r_m^2}\ 0.0094\ (1 + 0.013i) \right|$$

$$= \frac{1}{r_m^2}\ 0.0094$$

$$\left|\frac{E_2}{M_2}\right| = \left| -\frac{1}{r_m^2}\ 0.00012 \right|$$

The ratio of these image echo magnitudes, in dB, is:

$$20 \log \frac{E_1}{E_2} = 38 \text{ dB} .$$

In this case the relative amplitudes of E_1 and E_2 are such that E_2 can, with minimal error, be ignored in the overlapping region.

Consider the images formed by the echo returning from this table tennis ball via two different sonar imaging techniques, namely:

(a) The 3-D sonar system described in this dissertation.
(b) A classical beam-forming sonar.

Image (a): Figure 3.2 shows how the bearing of the returning echo wavefront is measured by two adjacent transducers.

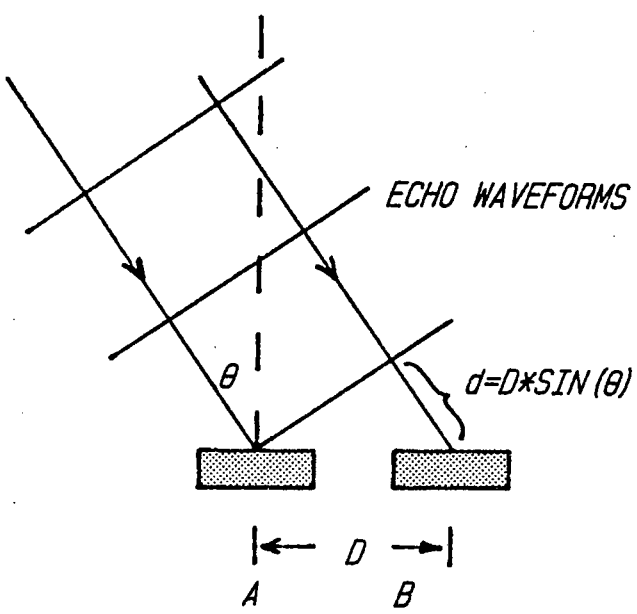

Figure 3.2: Bearing measurement by two transducers.

The returning echo arrives at transducer B delayed, relative to transducer A, by the time taken for the sound to travel the distance δ. Since both image pulses arrive at B delayed by the same amount, relative to A, a single bearing will be output from the system for the whole echo structure.

It is important to note that the dynamic range of echo amplitudes can be ignored since, in the measurement of the bearing, the amplitude information is discarded. Hence the bearing output for this system is equally valid for both image pulses and is displayed sequentially.

Figure 3.3 represents the image of the table tennis ball displayed by this system showing a single screen highlight where the image pulses coincide one on top of the other. (A full description of the display technique is presented in Section 4.8.)

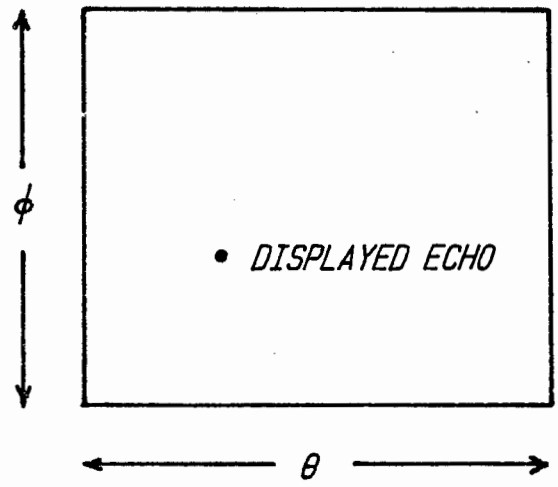

Figure 3.3: Image of a table tennis ball for the 3-D sonar system.

Image (b): The display, for the beam scanning sonar chosen for comparison, is a plan position indicator type with the following characteristics:

(i) The display is a polar representation of range and azimuth.

(ii) The screen intensity is modulated by the acoustic backscatter amplitude present at the output of the beamformer.

(iii) The acoustic backscatter as detected by the beamformer is however modulated by not only the echo strength, but also the directional sensitivity ($H(\Theta)$) of the formed beam.

Figure 3.4 shows the directional sensitivity of a linear array that is amplitude shaded by an approximation of the cosine-on-pedestal weighting function intended to minimise sidelobe sensitivity.

If, for the sake of clarity, the display intensity is assumed to be a binary function compressing 60 dB of backscatter dynamic amplitude to an "ON" value, then the image displayed by this sonar system, of the table tennis ball, would appear as shown in Figure 3.5.

Note the similarity in the displayed sidelobes of the first image pulse and the displayed second image pulse itself.

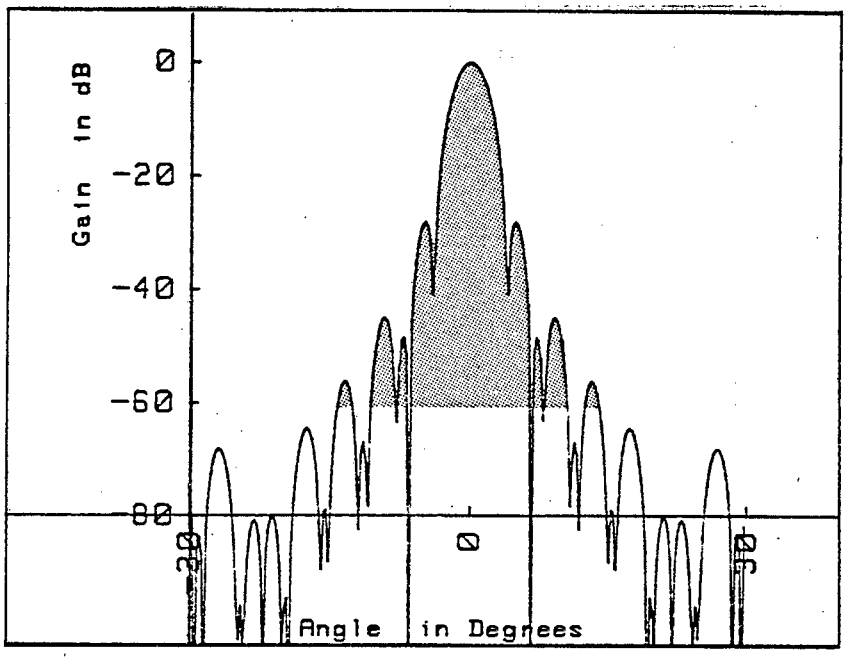

Figure 3.4: An example of the directional sensitivity for a line array.

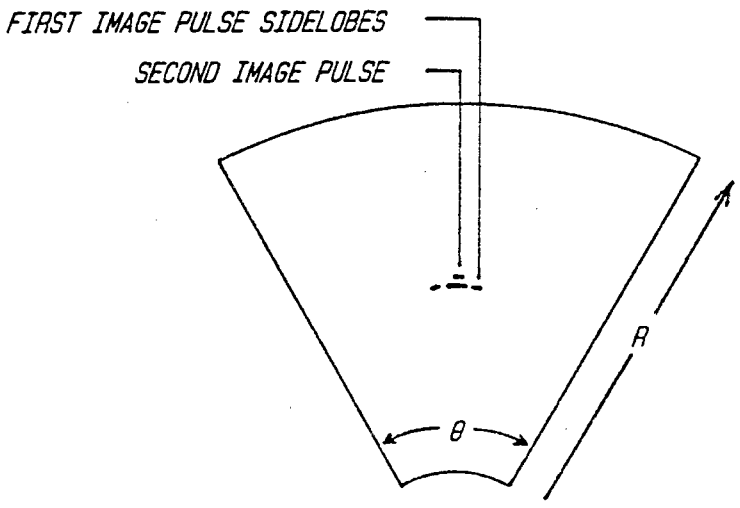

Figure 3.5: Image of a table tennis ball for the beamforming sonar.

3.3.2. Brick

As a second example demonstrating the structure of the returning echo from, in this case, a large insonified object, consider a smooth closed-cell foam block similar in dimensions to a building brick. Figure 3.6 shows the orientation of the brick to be imaged.

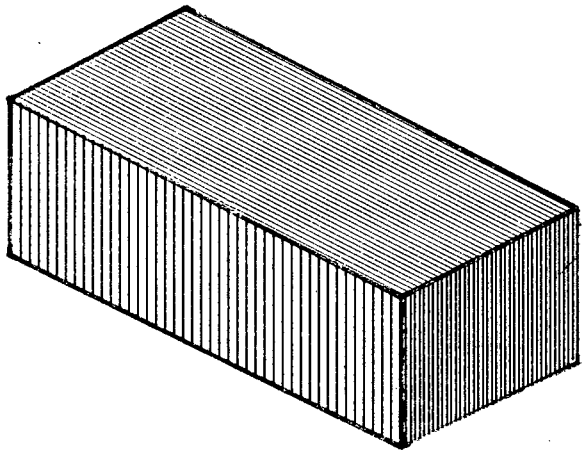

Figure 3.6: Imaged brick.

Summarised in Figure 3.7 and Table 3.1 are the results arrived at in Appendix A, which describes in detail the prediction of the returning echo for the brick using Freedman's analytical method.

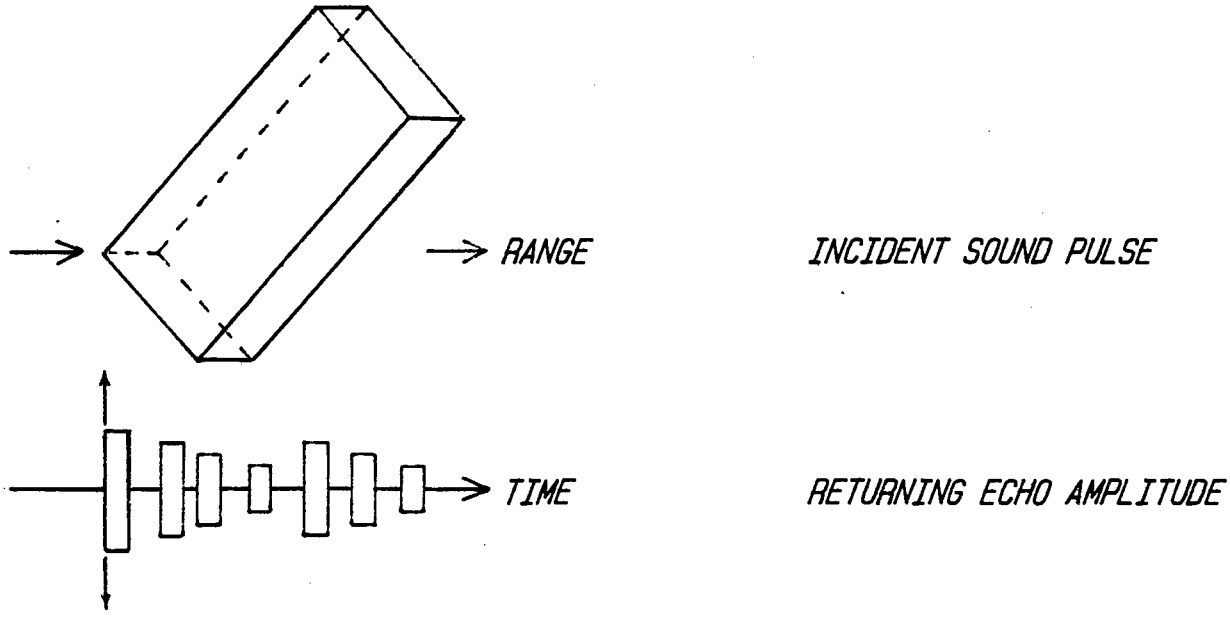

Figure 3.7: Echo structure for the imaged brick.

TABLE 3.1:

	$\left\lvert \frac{E r_m^2}{Mi} \right\rvert$ [x 10^{-4}]	Relative Image Pulse Range $(r_m - r_1)$ [mm]	Relative Image Pulse Strength for each Target $20 \log (\frac{E_i}{E_1})$ [dB]	Relative Image Pulse Strength for both Targets $20 \log (\frac{Ei}{E_1 (Ball)})$ [dB]
Table Tennis Ball E1	94	0	0	0
E2	1.2	18.75	-37.9	-37.9
Brick E1	1,0	0	0	-39.5
E2	0.75	35	- 2.5	-42
E3	0.63	60	- 4	-43.5
E4	0.38	95	- 8,5	-48
E5	0.63	135	- 4	-43.5
E6	0.38	169	- 8.5	-48
E7	0.25	195	-12	-51.5

The echo from the brick comprises of only seven discrete image pulses. These would be displayed by the previously mentioned imaging systems as shown in Figures 3.8 and 3.9 respectively.

Image (a)

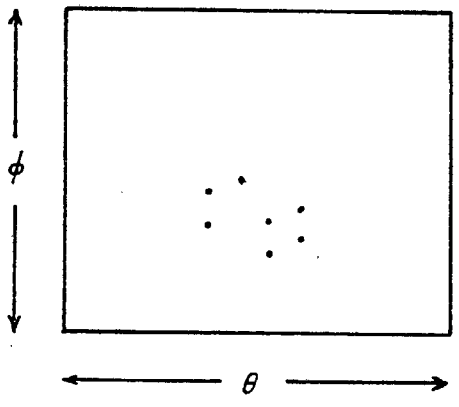

Figure 3.8: Brick imaged by 3-D sonar system

Image (b)

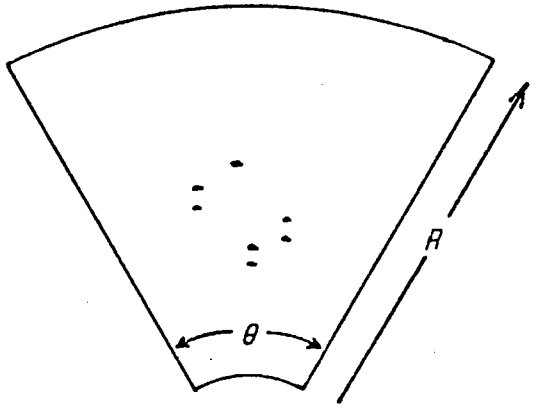

Figure 3.9: Brick imaged by beam scanning system

There is no loss of target information in either of the above displays where, in each case, all seven highlights appear. This comparable performance demonstrated by the 3-D imaging sonar stems from the fact, as shown in the above example, that even complex targets appear as a relatively few dominant highlights spatially distributed across the body.

The resemblance to a brick in either of the above system displays in not what one would expect with an experience in optical images. Whereas the foam brick is optically rough, at acoustic wavelengths the faces of the brick are smooth and reflect without scattering the incident sound.

In the examples thus far no loss of information has been experienced due to overlapping echoes. This situation is demonstrated by a third example combining both the table tennis ball and the brick.

3.3.3. Composite target

Consider the "worst case" combination of these two targets. That is, let the ball be attached to the brick in such a manner that the closest surface of the ball coincides in range with the strongest (and closest) highlight of the brick.

Figure 3.10 sketches two elevations of this complex combination.

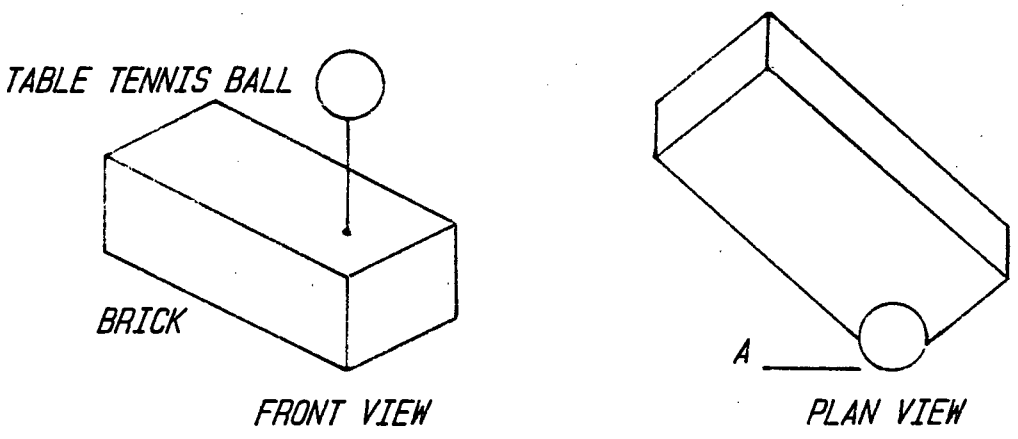

Figure 3.10: Composite target comprising of a table tennis ball and a brick.

Included in Table 3.1 are columns giving the ranges of the individual highlights and their relative echo strengths. Figure 3.11 attempts to demonstrate the composite echo structure by means of an artificial oscilloscope representation showing the amplitude of the received image envelope in time. (The envelope of the transmission pulse is assumed to be an idealised pulse with a 20 μs duration.)

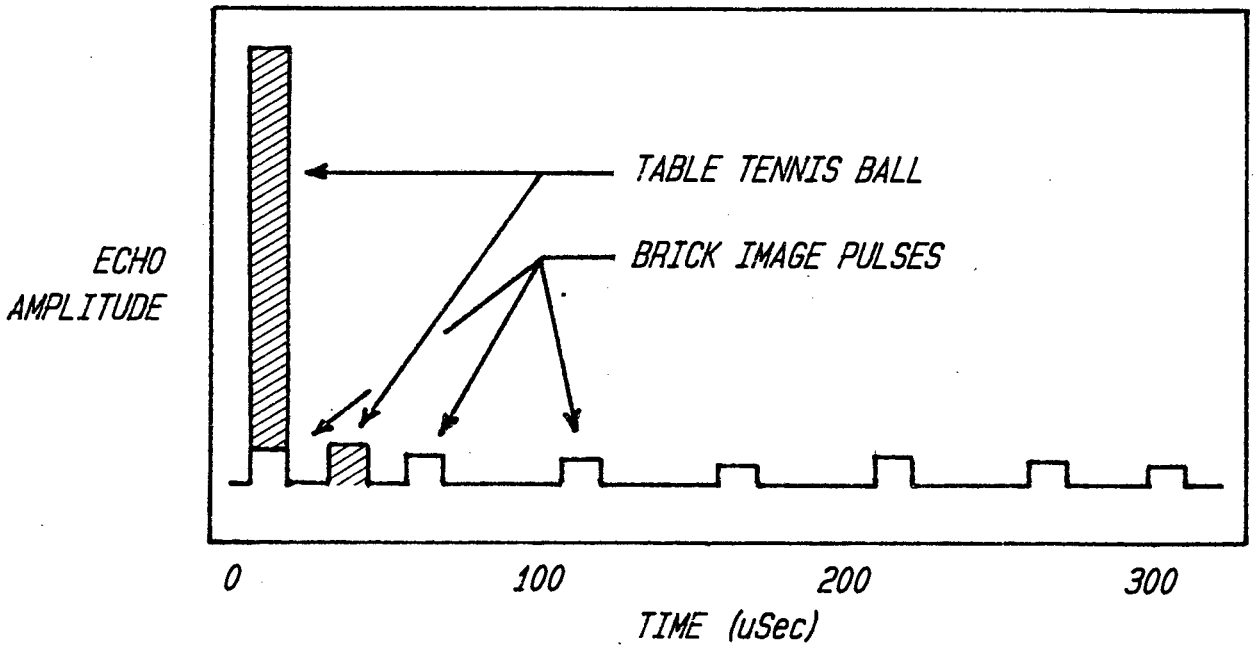

Figure 3.11: Envelope of the echo waveform for the composite target.

Image (a): Since the amplitude of the echo originating from the table tennis ball exceeds the overlapping echo from the brick by such a margin, the measured bearing samples at this range would pass the detector thresholds and would thus be displayed.

The maximum phase error measured at point A would be:

$$\begin{aligned} \Delta\Phi_{max} &= \text{arc tan } (10^{-39.5/20}) \\ &= 0.61° \\ &< 0.2\%. \end{aligned}$$

In Figure 3.12 the displayed image of the combined target for the 3-D sonar system shows clearly the exclusion of a target highlight.

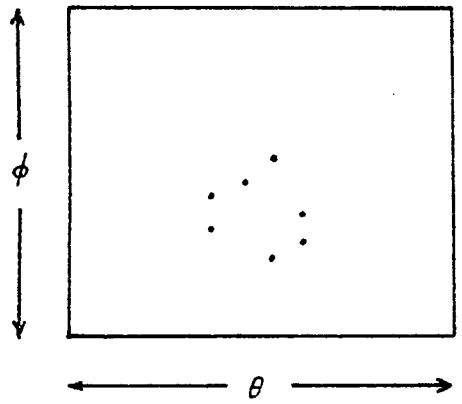

Figure 3.12: Composite target imaged by 3-D sonar system.

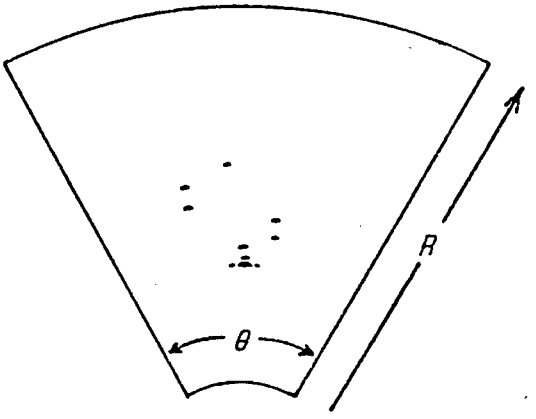

Figure 3.13: Composite target imaged by beamforming sonar.

Image (b): Assuming once again the screen intensity compression (allowing a dynamic range of 60 dB of backscatter amplitudes to be displayed), the target would then ideally appear as shown in Figure 3.13.

Relative to the 3-D sonar, the beamforming sonar does not fare much better when operating in environments where overlapping echoes of a large dynamic range are encountered. In practice there is a reasonable chance that weaker image pulses will be masked by the dominant echo sidelobes resulting in a corresponding loss of image information.

3.4. Conclusion

It has been shown in this chapter that the returning echo from targets, even large solid objects, is composed of only a small number of highlights. The simplicity of the 3-D sonar system is thus achieved by recognising that the limitation of the non-overlapping echo condition is less of a constraint than would first be supposed.

The fundamental assumption for the operation of this system regarding the echo structure does therefore not put this system at a disadvantage relative to a beamforming sonar since, whatever the imaging technique, a typical sonar image consists mostly of target highlights.

CHAPTER 4

3-D IMAGING SONAR SYSTEM

4.1. Introduction and System Block Diagram

This chapter describes the hardware realisation of the 3-D imaging sonar. A schematic of the sonar system is presented in block diagram form in Figure 4.1 and the constituent block element, comprising the system, are listed below.

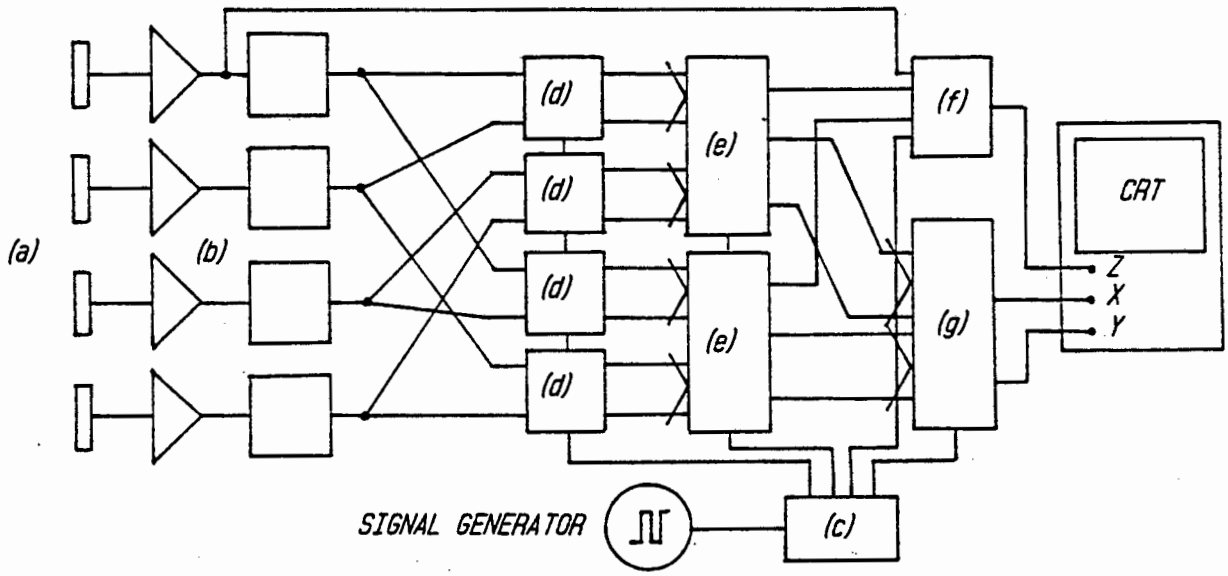

Figure 4.1: Schematic block diagram of the 3-D imaging sonar system.

(a) Transducer array
(b) Preamplifier and zero-crossing detector
(c) System sequencer
(d) Digital phase meter
(e) Data processor
(f) Amplitude threshold detector
(g) Display generator.

Since the reader has been introduced to the system's operation (Section 2.4) this chapter endeavours only to deal with the design and operation of each of the above listed elements.

Appendix B gives full circuit diagrams and discusses the electronic operation of each subsection.

4.2. Transducer Array

4.2.1. Introduction

The transducer array consists of five identical piezoelectric transducer elements as shown in the photograph in Figure 4.2.

Four of these elements are arranged in a square forming the receive array. It is the function of these elements to convert the impinging acoustic energy into electrical signals.

The remaining element, the transmitter, is placed adjacent to the receive array and its function is to convert a gated, high amplitude, electrical oscillation into an energetic acoustic tone burst.

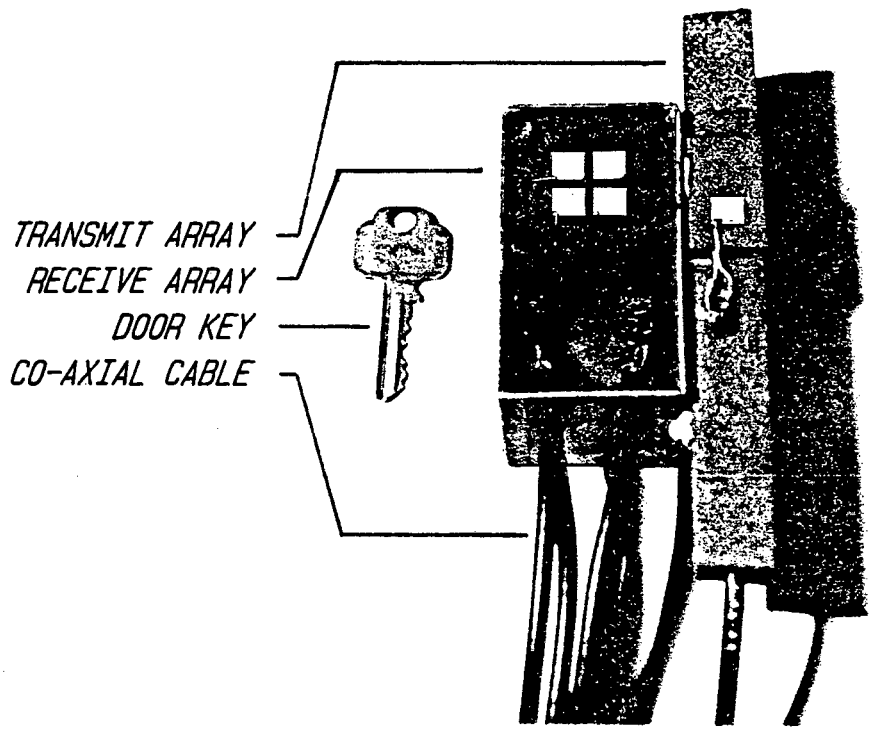

Figure 4.2: The receiver and transmitter array.

4.2.2. Method of Construction

The construction of the array and the mounting of each transducer element is illustrated in the crossection depicted in Figure 4.3.

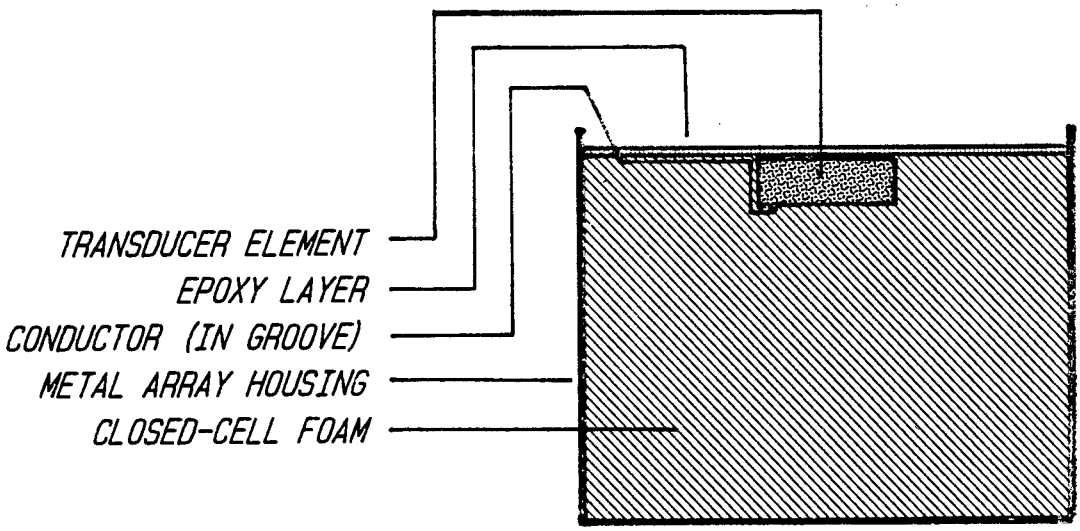

Figure 4.3: Transducer construction.

Briefly, recesses of dimensions equal to the individual elements were milled into the top surface of a block of closed-cell rigid PVC foam. A thin wire conductor was soldered to each of the silvered faces of the transducers and the elements inserted in their respective recess. The wires were led to the edge of the foam block in shallow grooves where they were connected to co-axial cables. (Care was taken that the elements were similarly orientated with respect to their polarity.)

The foam block was laid horizontally, elements up, in an open-topped metal array housing. The housing was then filled with a low viscosity Ciba Geigi epoxy until the elements were covered with a thin layer of epoxy.

When this slow curing epoxy had hardened, the resulting air-backed transducer was characterised by a circle diagram, the significance of which is explained in Section 4.2.3.

4.2.3. *Theory* : Development of the Equivalent Electrical Circuit

The circle diagram is an important analytical representation of the electrical admittance characteristics of resonant circuits. When applied to electro-mechanical transducers it is sometimes referred to as the motional admittance diagram (Reference 16). As such it plots the locus of admittance (of the device under test) for a sweep of frequencies.

This is achieved by driving the load with a voltage of constant amplitude and measuring the magnitude and phase of the resultant current at each frequency. The results are plotted on a graph with the axes conductance and susceptance, where the real and imaginary components of the suitability scaled current measurements are represented respectively.

In order to predict the trend of this locus it is important to introduce an equivalent two-port electrical circuit for the transducer. Mason (Reference 17) provides a convenient electrical model for piezo-electric transducers using lumped electrical components as shown in Figure 4.4.

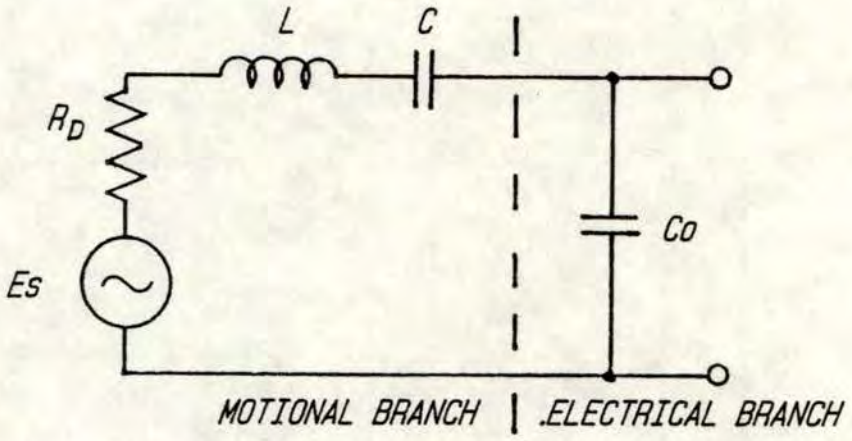

Figure 4.4: Equivalent electrical circuit for a resonant transducer.

Where;

E_s is the open circuit signal voltage source

R_D is the dynamic resistance, representing the total of both the radiation resistance and the electro-mechanical losses

L is an inductor relating to the mechanical mass of the element

C is a capacitor relating to the mechanical compliance of the element and

C_0 is the electrical clamp capacitance arising from the physical structure of the transducer.

The mechanical resonant frequency is by definition;

$$\omega_m = \sqrt{\frac{1}{LC}} \qquad [\text{RAD } S^{-1}] \tag{4.1}$$

The equivalent circuit in Figure 4.4 is a simplified representation of the general model for a block of piezo-electric material and thus only holds under the following conditions:

(a) This model allows for only one mechanical resonance in the frequency band of interest and therefore only holds over this band.
(b) The transducer element is air-backed.
(c) The front face of the transducer is unmatched and in perfect contact with the water.
(d) Leakage resistance and dielectric losses are ignored.

The electrical admittance of the motional branch of Figure 4.4 can be expressed as a function of frequency as follows:

$$Y = \frac{1}{R + jX}$$

$$= \frac{1}{R_D + j(\omega L - \frac{1}{\omega C})}$$

$$= G + jB$$

where

$$G = \frac{R_D}{R_D + j(\omega L - \frac{1}{\omega C})} \qquad \text{and} \qquad B = \frac{-(\omega L - \frac{1}{\omega C})}{R_D + j(\omega L - \frac{1}{\omega C})}$$

However the magnitude of the motional branch admittance can also be written as:

$$|Y|^2 = G^2 + B^2 = \frac{1}{R^2 + X^2} \tag{4.2}$$

By substituting in for R, X, G and B and adding $(\frac{1}{2R_D})^2$ to both sides, Equation 4.2 simplifies to:

$$(G - \frac{1}{2R_D})^2 + B^2 = (\frac{1}{2R_D})^2 \tag{4.3}$$

Equation 4.3 describes a circle, plotted on the admittance plane, with a radius of $\frac{1}{2R_D}$ and a centre at $(\frac{1}{2R_D}, 0)$ as shown in Figure 4.5(a).

Since the electrical branch of Figure 4.4 is purely susceptive, its contribution to the circle described by Equation 4.3 is to effectively "lift" the circle by an amount $(j\omega c_0)$ on the B axis.

Figure 4.5(b) shows the form of a typical circle diagram measured over a narrow frequency band around the frequency of resonance for a transducer. At the mechanical resonant frequency, indicated as f_0 on the diagram, the admittance is $(\frac{1}{R_D}, j\omega C_0)$.

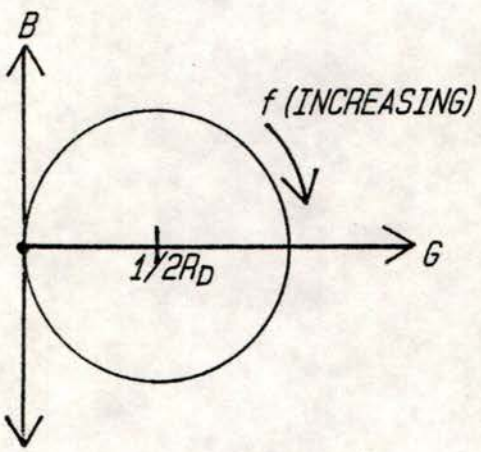

Figure 4.5(a): Circle diagram for the motional branch of the transducer equivalent circuit.

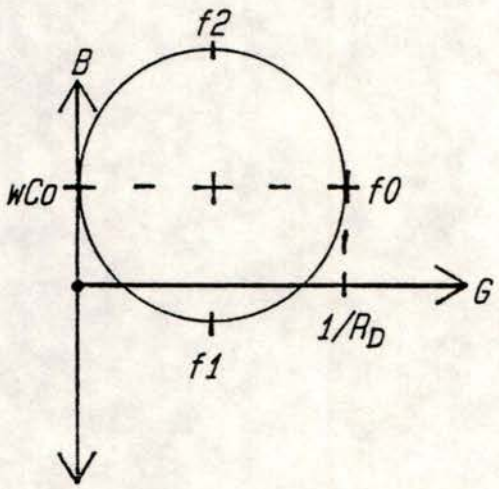

Figure 4.5(b): Circle diagram for a piezo-electric transducer.

It is easily shown that the frequencies indicated as f_1 and f_2 in Figure 4.5(b) represent the half-power points on the transducers response which, together with the

centre frequency, enables the Q of the transducer to be graphically determined:

$$Q = \frac{f_0}{f_2 - f_1} \tag{4.4}$$

Referring to the equivalent circuit, the electrical Q of an RLC series resonant network is defined as;

$$Q = \frac{\omega L}{R_D} \tag{4.5}$$

Equating 4.4 and 4.5 (at the centre frequency) yields:

$$\frac{2\pi f_0 L}{R_D} = \frac{f_0}{f_2 - f_1}$$

$$\therefore \quad L = \frac{R_D}{2\pi (f_2 - f_1)} \tag{4.6}$$

Since R_D is the reciprocal of the conductance at f_0, the value of the inductor L in the equivalent electrical circuit can easily be found and hence the value of the capacitor C can be calculated using Equation 4.1.

Finally, the clamp capacitance C_0 can be measured on an AC impedance bridge operating at a suitably low frequency.

At this point in the analysis the transducer is fully characterised by its electrical equivalent circuit with component values determined as described above.

4.2.4. Results

Figure 4.6(a) gives the circle diagram of one element with the transducer array immersed in water. The equivalent circuit was evaluated and is shown in Figure 4.6(b).

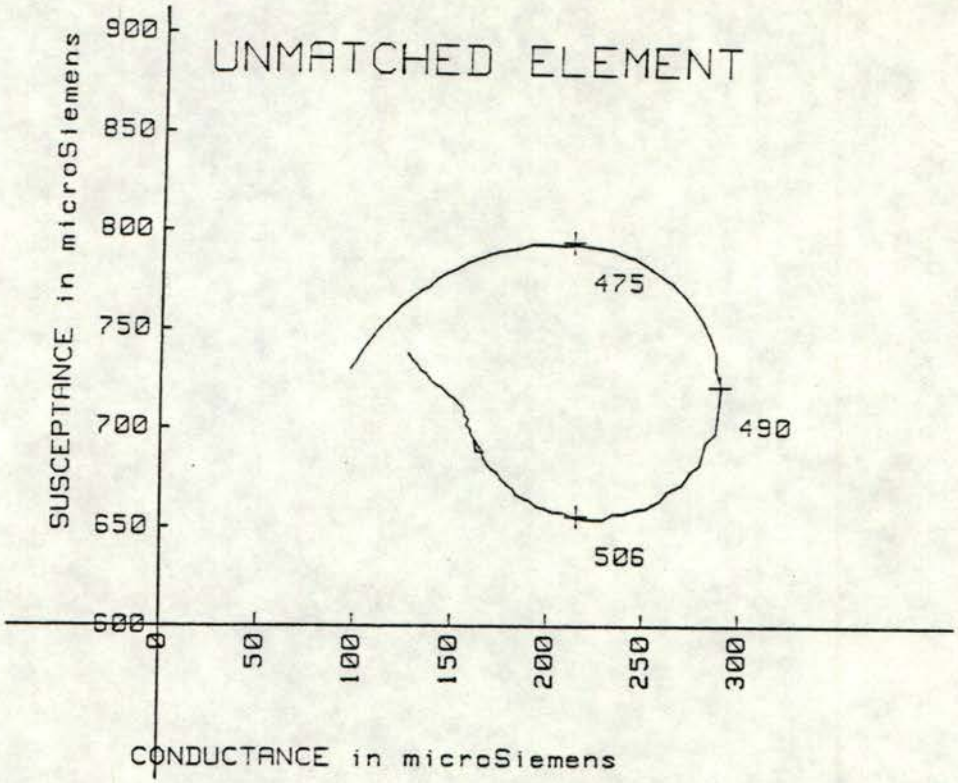

Figure 4.6(a): Measured circle diagram for a single transducer element.

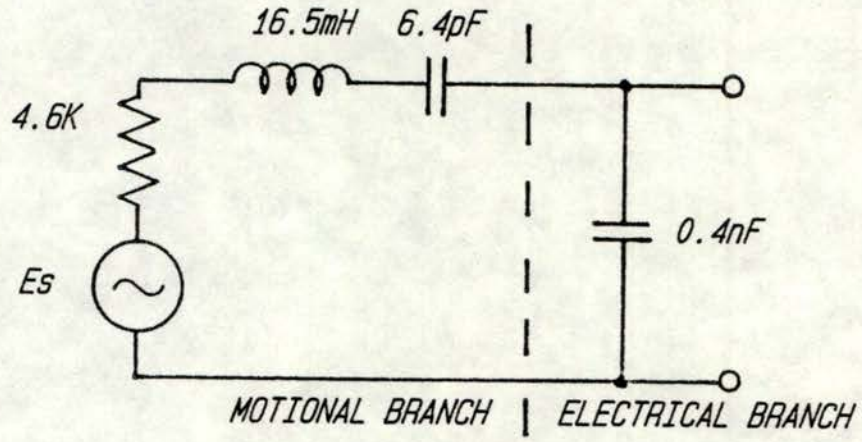

Figure 4.6(b): The equivalent circuit, with component values, for the transducer element.

Further results of measurements made on the array are listed below. It must however, be stressed that the results summarised in Figure 4.6 are all that are required for matching to the preamplifier and optimising the transducers performance.

Receiver voltage sensitivity:

Figure 4.7 shows the on-axis open circuit receiver voltage sensitivity of an unmatched element, as a function of frequency, using one array element as a hydrophone.

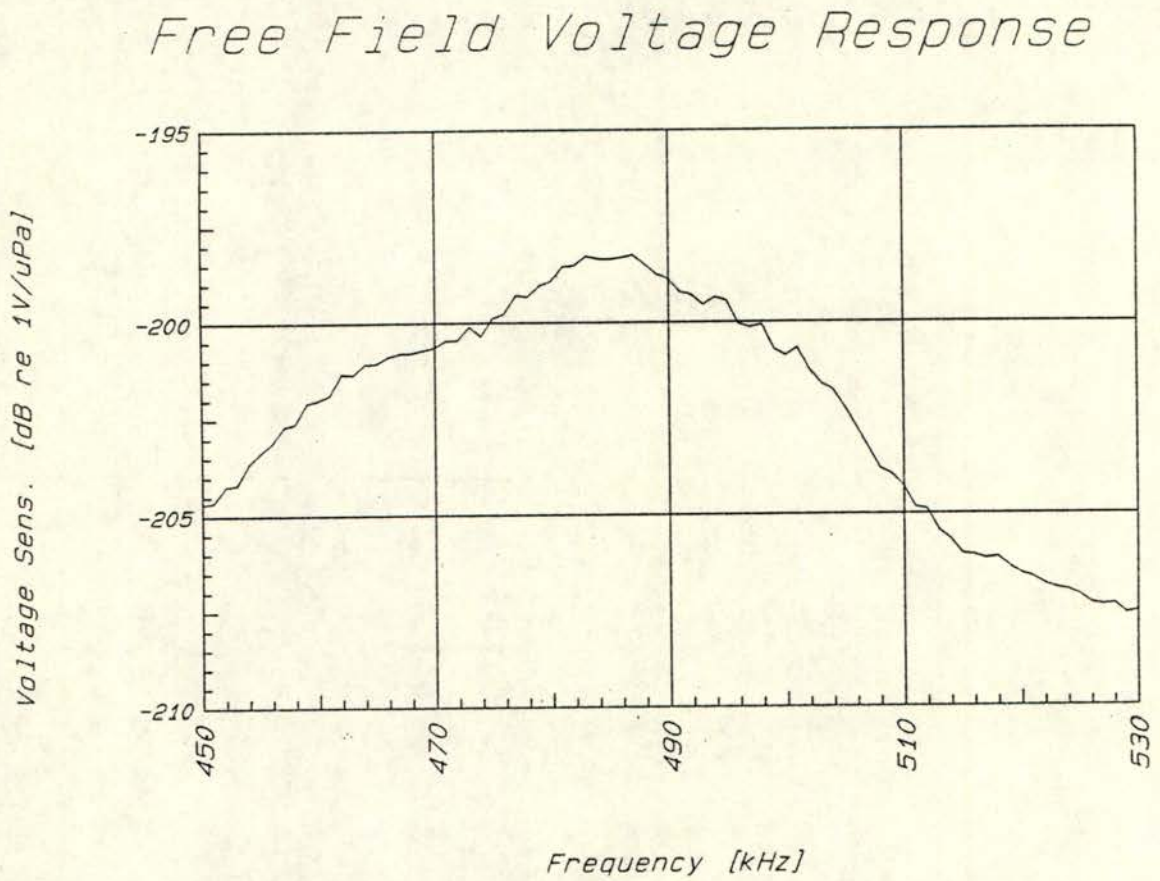

Figure 4.7: Sensitivity of a single array element.

Directivity response:

The directional sensitivity of a single element operating as a transmitter is shown in Figure 4.8 which is assumed, due to the reciprocal nature of the array, to be identical to the receiving directivity response.

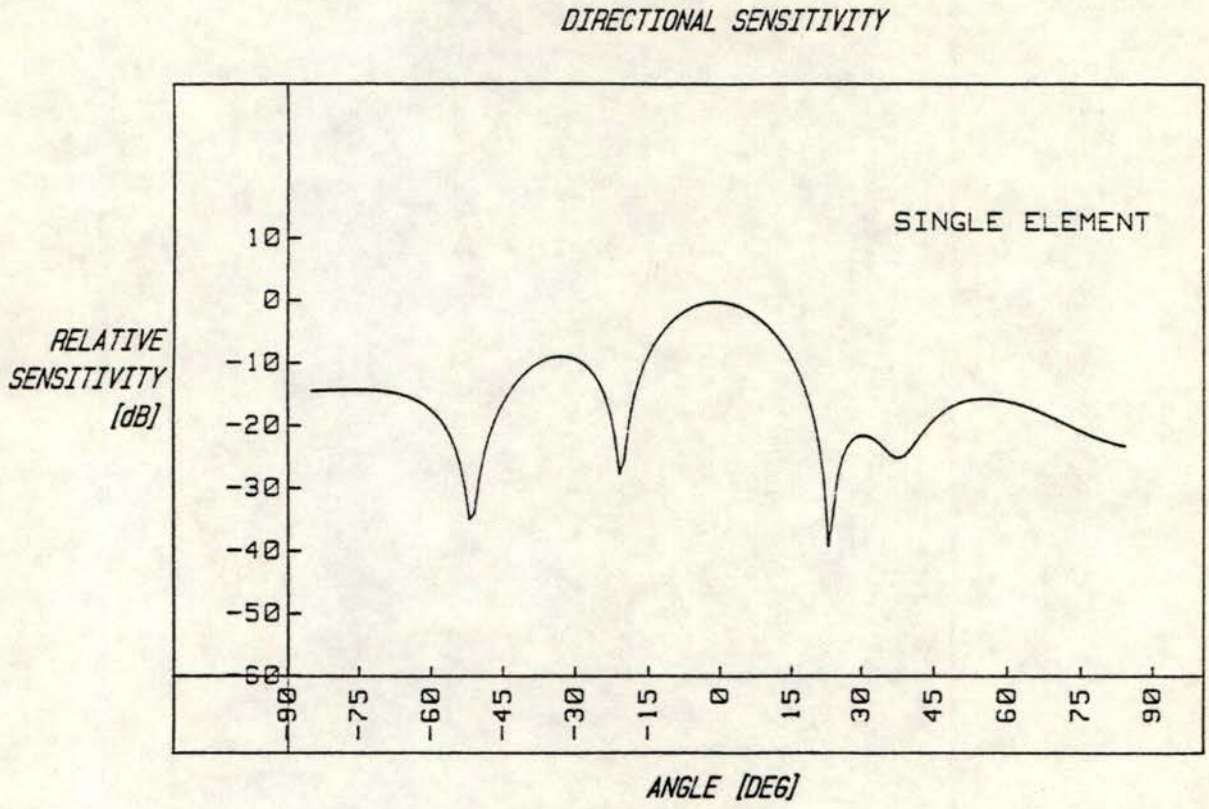

Figure 4.8: Directional sensitivity of a transducer element.

4.2.5. Conclusion

The arrays, as described above, were used throughout the practical evaluation of the system and performed satisfactorily.

A parameter that was not examined until well after completion of the receive array was that of mutual coupling between adjacent transducer elements. Roy (Reference 18) had reason to examine this problem and suggests possible solutions. Fortunately, as will be shown in Section 4.5, there was sufficient acoustic decoupling between elements of this array for this phenomenon not to present significant effects.

4.3. Preamplifier and Zero-crossing Detector

4.3.1. Introduction

In the system overview (Section 2.4) the reader was introduced to the principle of operation of the 3-D imaging sonar. Like Nairn's "digital sonar" this system extracts

the bearing information of targets exclusively from the phase of the signals present at the transducer elements.

Of the numerous methods of phase determination, the phase measuring device chosen for implementation required, as input, waveforms preserving only the instant of zero-crossing of the signal amplitudes. It is therefore the function of the input stage to amplify and condition the signals from the transducers to a format compatible with the phase meter requirements.

Figure 4.9(a) illustrates the operation of this input stage which can be likened to the action of a voltage comparator as shown in Figure 4.9(b).

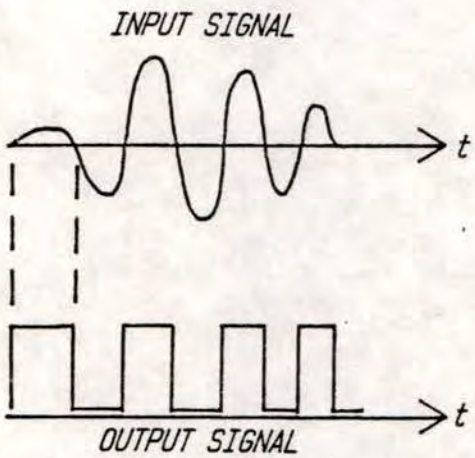

Figure 4.9(a): Time waveforms illustrating the operation of the zero-crossing detector.

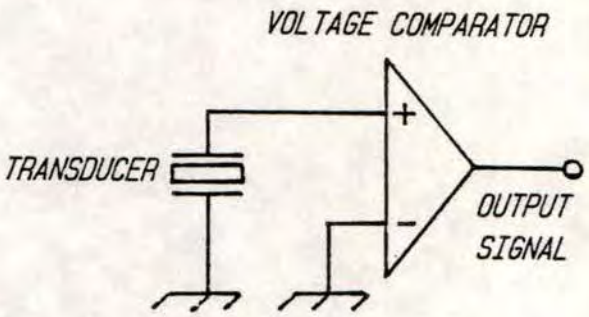

Figure 4.9(b): Schematic diagram demonstrating the principle of operation.

Figure 4.10 gives a schematic block diagram of the input amplifier and zero-crossing detector described in this section. Its operation is as follows:

The signal from the transducer is linearly amplified with a minimum of signal-to-noise degradation by a low-noise preamplifier. The subsequent wideband and high gain amplifier performs a clipping action on the signal, thereby serving to increase the slope of the waveform in the region of its zero-crossing. Finally a fast comparator with a TTL compatible output conditions the signal for the ensuing digital processing.

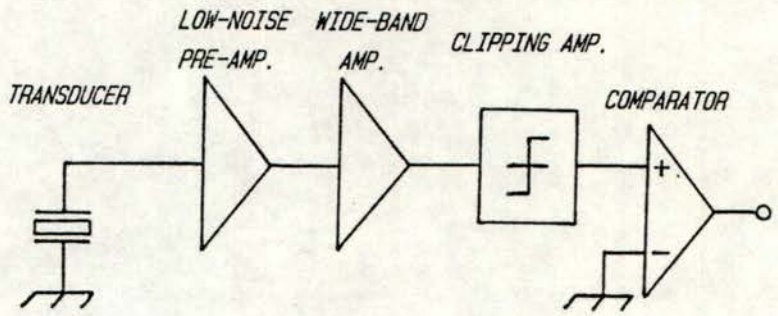

Figure 4.10: Schematic block diagram of the input amplifier and zero-crossing detector.

4.3.2. Preamplifier Noise Considerations

To understand the noise contraints imposed on this design consider first the sources of noise appearing at the preamplifier input.

(a) Sea State Noise:

Urick (Reference 15) states that the ambient noise spectra in the water at 500 kHz is overwhelmed by thermal noise and that the contribution by sea state noise can thus be neglected.

(b) Thermal Noise:

Here Urick quotes Mellen (Reference 19) as having shown that the thermal noise of the molecules of the water place a limit on the minimum observable pressure level in the sea at high frequencies.

For an omnidirectional hydrophone, with perfect acousto-electric conversion efficiency, the equivalent noise spectrum level is;

$$NL = -15 + 20 \log f \qquad \text{dB re } 1\mu\text{Pa} \qquad (4.7)$$

where f is the frequency in kilohertz.

Given the hydrophone directivity index DI and the efficiency E, both expressed in decibels, the equivalent thermal noise spectrum level becomes:

$$NL = -15 + 20 \log f - DI - E \qquad \text{dB re } 1\mu\text{Pa} \qquad (4.8)$$

This noise is however the same as the thermal or Nyquist noise developed in the radiation resistance of the hydrophone immersed in water. The output noise level sourced by the transducer can thus be estimated by considering the noise voltage due to the dynamic resistance R_D.

In general, the thermal noise voltage produced by a resistance R is given as;

$$V_{NOISE} = \sqrt{(4\ kTR)} \qquad V_{RMS} / \sqrt{Hz} \qquad (4.9)$$

where k is Boltzmann's constant and T the absolute temperature.

Substituting into Equation 4.9 the value of R_D yields a system source noise of:

$$V_{NOISE} = \sqrt{(1.62 \times 10^{-20} \times 4\ 600)}$$

$$= 8.6\ nV_{RMS} / \sqrt{Hz}$$

$$= -161 \text{ dB re } 1\ V_{RMS} / \sqrt{Hz}$$

Having established the source noise level, attention can now be focussed on the noise performance of the preamplifier itself. This is particularly significant since, if in excess, the amplifier noise sets the lower limit on the noise voltage in the detector as a whole.

Figure 4.11 gives the noise model for a multiple stage amplifier with noise present at its input.

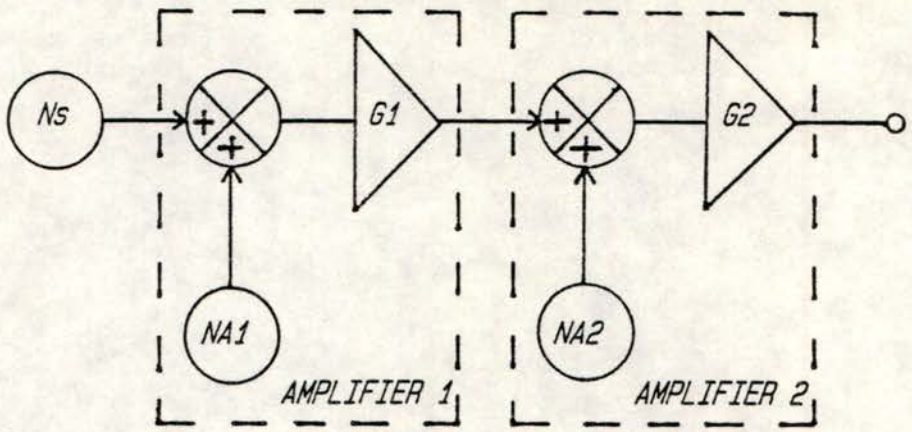

Figure 4.11: A noise model for a multiple stage amplifier.

Each amplifying stage is represented here by a perfect "noiseless" amplifier of gain G_i with its own noise contribution, referred to its input, of N_{Ai}.

The noise figure for an amplifier is simply the ratio, in decibels, of the output of the real amplifier with source noise at its input, to the output of a noiseless amplifier with equal gain and the same source noise present at its input.

For the first stage, the noise figure NF is:

$$NF_1 = 10 \log_{10} \left[\frac{G_1 [N_s + N_{A1}]}{G_1 N_s} \right]$$

$$= 10 \log_{10} \left[1 + \frac{N_{A1}}{N_s} \right] \qquad (4.10)$$

For both stages, referring NA_2 to the input of stage 1:

$$NF_{12} = 10 \log_{10} \left[\frac{G_1 G_2 [N_s + N_{A1} + N_{A2} / G_1]}{G_1 G_2 N_s} \right]$$

$$= 10 \log_{10} \left[1 + \frac{N_{A1}}{N_s} + \frac{N_{A2}}{G_1 N_s} \right] \qquad (4.11)$$

From Equation 4.11 it is clear that the relative contribution to the total noise performance by the second gain stage, or any subsequent stage, is rendered insignificant by the gain of the first stage.

To summarise thus far two points have emerged:

(a) Firstly, the source of the system input noise has been identified and its magnitude theoretically estimated.

(b) Secondly, the onus rests on the first gain stage to ensure a low overall system noise.

Consequently the first objective in the realisation of the preamplifier is the design of the initial gain stage, aptly named the low-noise front-end.

The requirements of this device are; that it be electrically matched to the transducer, that it provide at least a moderate gain (20 dB), and that its equivalent input noise be of the same order of magnitude as that sourced by the immersed transducer.

4.3.3. Low-noise Front-end

(a) Matching to the Transducer:

In Section 4.2.4 the electrical equivalent circuit of the transducer was examined and its component values were established. This circuit simplifies, when operated at the mechanical resonant frequency, to a signal voltage source of source resistance R_D loaded with the clamp capacitor C_0.

The first objective in transducer matching is to remove the effect of the reactive loading presented by the clamp capacitance. This can be achieved by adding, in parallel with the transducer, a matching indicator L_0 such that the parallel resonant frequency of L_0 and C_0 equal the mechanical resonance.

That is:

$$\frac{1}{LC} = \frac{1}{L_0 C_0} = (2\pi f_0)^2 \qquad (4.12)$$

Figure 4.12(a) shows the implementation of just such a matching inductor which, when considering the electrical network as a whole, is in effect a second order bandpass filter. If the condition imposed by Equation 4.12 holds, then the equivalent circuit can be transformed to a lowpass filter, as depicted in Figure 4.12(b), by simply removing C and L_0.

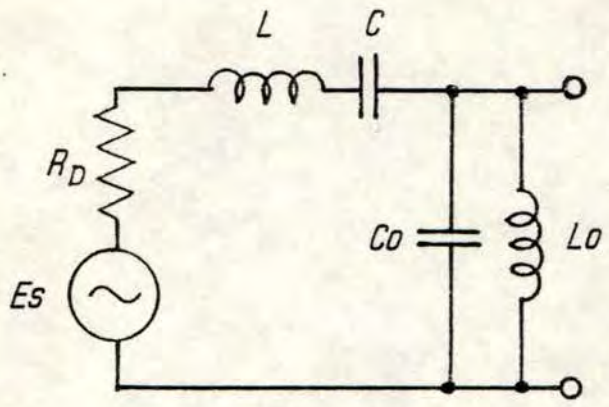

Figure 4.12(a): Equivalent circuit of an inductor matched transducer.

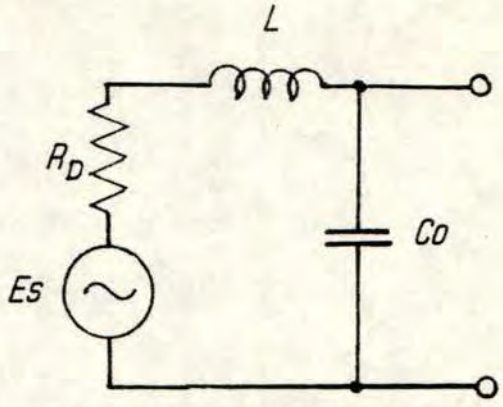

Figure 4.12(b): Lowpass transform for the equivalent circuit of a matched transducer

It is a property of the bandpass to lowpass transform that the half-power bandwidth of the filters remains the same. Thus the 3 dB breakpoint for the lowpass filter, approximated here as:

$$f_{LP} = \frac{1}{2\pi\sqrt{LC_0}} \qquad (4.13)$$

specifies the band of frequencies over which the matched transducer displays greatest sensitivity.

There is however, implicit in this matching technique, the ability to modify the bandwidth specified by Equation 4.13. If the value of the clamp capacitance is increased by the addition of a parallel capacitor then, as long as the matching inductor still satisfies Equation 4.12 for the new capacitor value, the transducer bandwidth will effectively be reduced. Since the value of L is constant for a given transducer and the capacitance is a minimum when equal to the clamp capacitance C_0, the broadest frequency response of the receiver remains that in Equation 4.13.

Plotted in Figure 4.13 is the theoretical frequency response of the lowpass transformed equivalent circuit for a transducer with an increasing amount of additional capacitance. (These curves are based on the component values measured for the transducer elements used in the 3-D sonar system, i.e. C_0 = 0.4nF and

L = 16.5mH.) Besides decreasing the transducer's operating bandwidth, there is a decrease in the overshoot in the transducer's response with added capacitance.

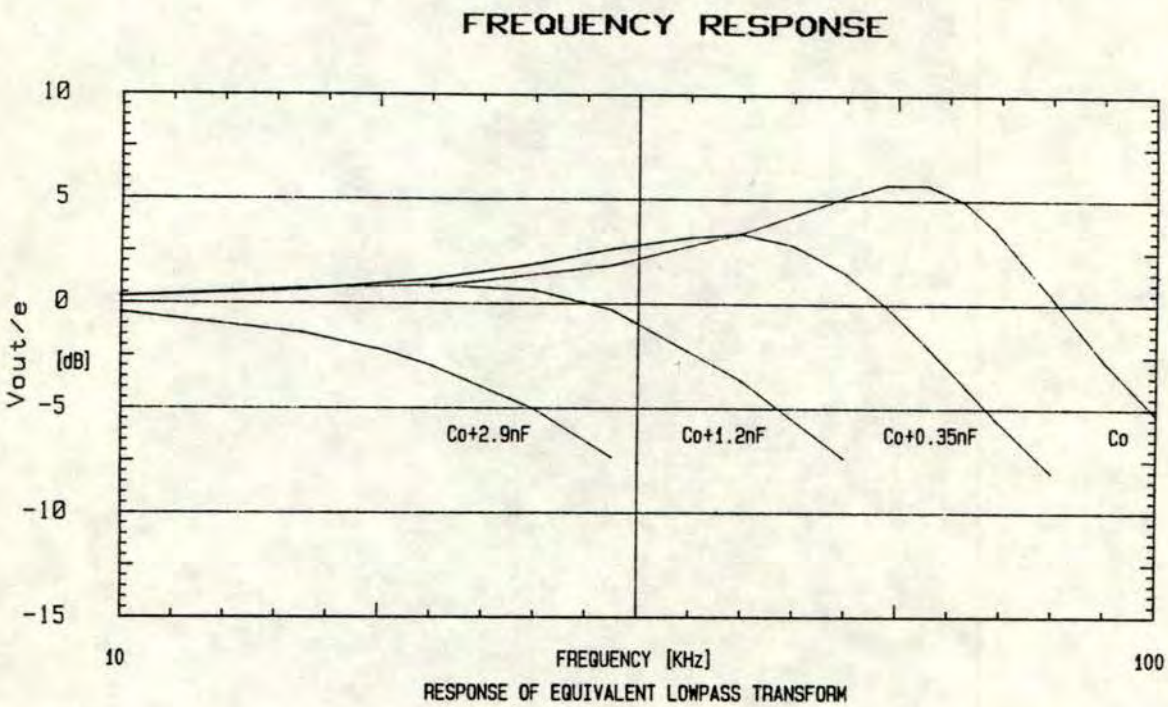

Figure 4.13: Frequency response of the lowpass transform for different values of capacitance.

In the interests of a broad-band frequency response, with the aim of detecting correspondingly shorter transmission pulses, matching was implemented with a minimum additional "trimming" capacitance.

There is a price paid for broad-band matching in that large inductance values for L_0 are required. This need for increased inductance introduces the limitation imposed on turn-numbers by the self-resonance of the winding capacitance with the inductor value itself. Figure 4.14(a) summarises the results of an experiment performed to evaluate the winding limitations, for various winding wires, of the only available ferrite potcore that operated over the frequency band of interest. (Figure 4.14(b) shows the test circuit used in the experiment.)

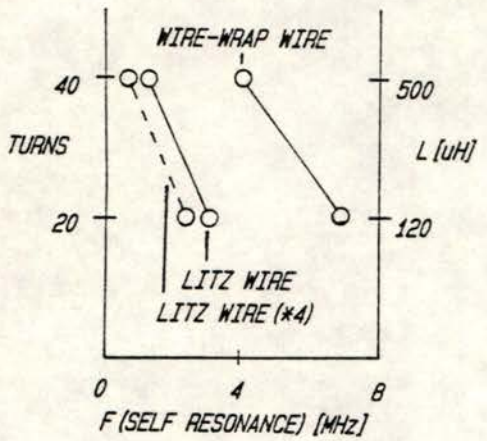

Figure 4.14(a): Graph summarising frequency limitations for various inductor values and types of winding wire.

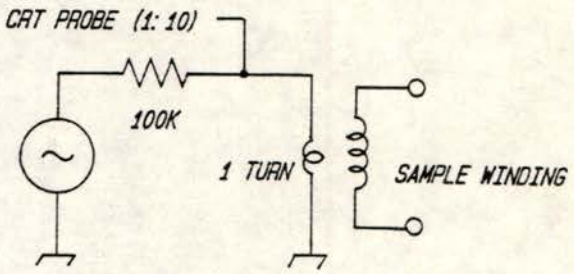

Figure 4.14(b): Test circuit used to evaluate winding self-resonance.

In order to isolate the subsequent preamplifier from the transducer, and hence avoid ground loops, the inductor chosen was in the form of a transformer where the primary inductance fulfills the matching requirements.

The primary inductance chosen was 140µH (20 turns on the transformer bobbin) requiring an additional trimming capacitor of 0.75 nF to be added. The lowpass equivalent circuit predicts, for this choice of matching, a bandwidth of 63 kHz and a passband ripple of no more than 3 dB. Purely for the purposes of theory validation, a second matching termination was implemented with a primary inductance of 32µH and a trimming capacitance of 3.3nF with a predicted 20 kHz bandwidth and no passband ripple.

Practical verification could only be carried out on these matching configurations after the development of the front-end amplifier.

(b) Low-noise Front-end:

The choice of the input active element in the front-end amplifier was the first question addressed in this design. Given the noise present at the input and the electrical impedance of the source (Section 4.2.3) an optimum (noise performance) solution was sought.

A simple noise model for a transistor gain stage is given in Figure 4.15, where e_n is the equivalent noise voltage looking in series with the base of the transistor and i_n, the equivalent input noise current in parallel with the source resistance R_s. The amplifier is assumed noiseless and provides a voltage gain of G.

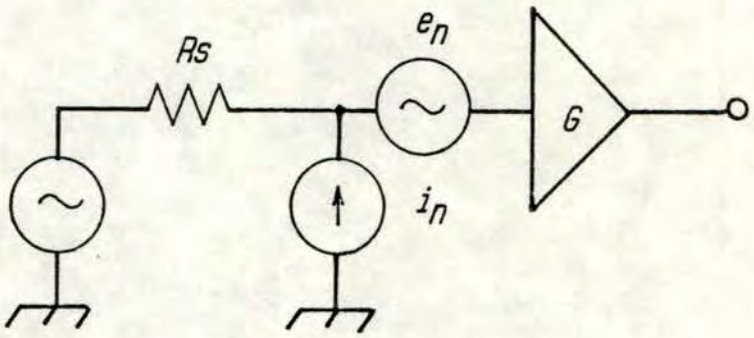

Figure 4.15: Simple noise model for a transistor gain stage.

The front-end amplifier thus contributes a total noise voltage e_a, referred to the input, of

$$e_a = [e_n^2 + (R_s\, i_n)^2]^{1/2} \quad V_{RMS}/\sqrt{Hz} \qquad (4.14)$$

Equation 4.14 contains two noise sources, the amplifier input noise voltage and the noise voltage generated by the amplifier noise current passing through the source resistance. Since these two noise sources are assumed uncorrelated, the total noise is simply the root sum of the square of these voltages.

Optimum noise performance is obtained when the source resistance R_s equals the "noise resistance" of the transistor. Noise resistance is not in fact a resistor or an equivalent circuit element, but rather a convenient tool defined to assist in the matching of transistors to given source resistances.

R_n is defined for a transistor as: (Reference 21)

$$R_n = \frac{e_n}{i_n} \qquad (4.15)$$

The value of this noise resistance is not constant for a transistor since e_n and i_n change independently with varying collector (or drain) currents. However, having selected a transistor the optimum bias condition can thus be set.

The nomogram in Figure 4.16 shows the spread of noise resistance values typically associated with the individual types of transistors. It should be bourne in mind that the source resistance, as seen by the transistor, can be altered by means of a transformer to accommodate more than one type of transistor.

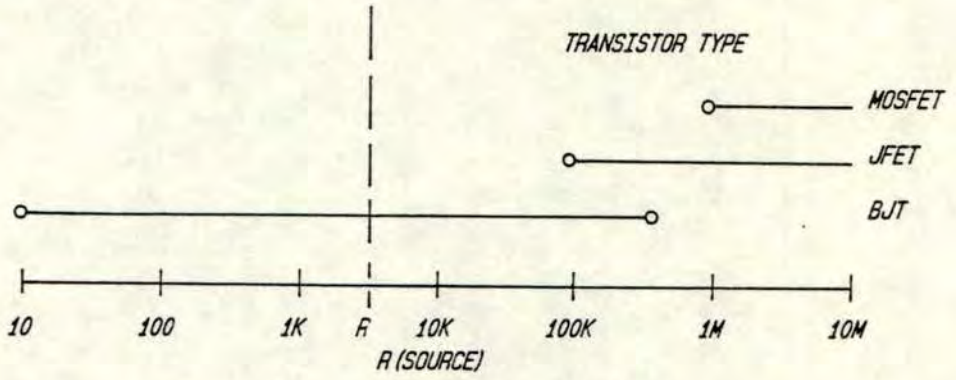

Figure 4.16: Typical spread of noise resistance values for various transistor types.

However in this case, due to the winding limitations, the transformer was unable to provide significant source impedance changes, the transformer was therefore used only for isolation purposes over and above transducer matching by means of its primary winding inductance.

Under these circumstances, the bipolar transistor was chosen as the input amplifying element for its excellent noise performance at noise resistance values in the region of the dynamic resistance of the transducer. In Figure 4.17 the optimum collector current for the BC107A with a source resistance of 4k7 ohms is given as 2mA with a specified noise figure of 2 dB. (Reference 20)

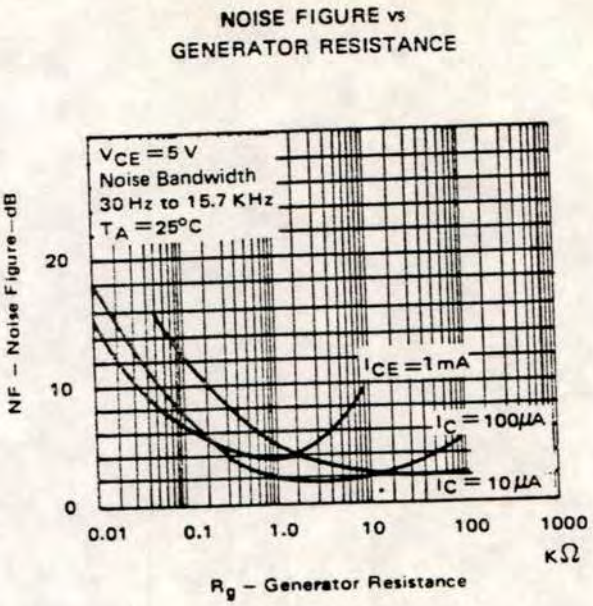

Figure 4.17: Graph of specified noise figures as a function of bias current and source resistance for the BC 107A transistor.

The front-end amplifier, the circuit of which is shown in Figure 4.18(a), was constructed and used in conjunction with the transducer array to verify the theoretically predicted frequency band of operation for the system. This was achieved using a technique similar to self-reciprocity as described by Urick (Reference 15), where a single reciprocal transducer is calibrated by making use of the image sound source in the water surface reflection as a second transducer. Figure 4.18(a) shows the experimental setup and physical layout for this test, and Figure 4.18(b) summarises the results obtained for two different matching networks.

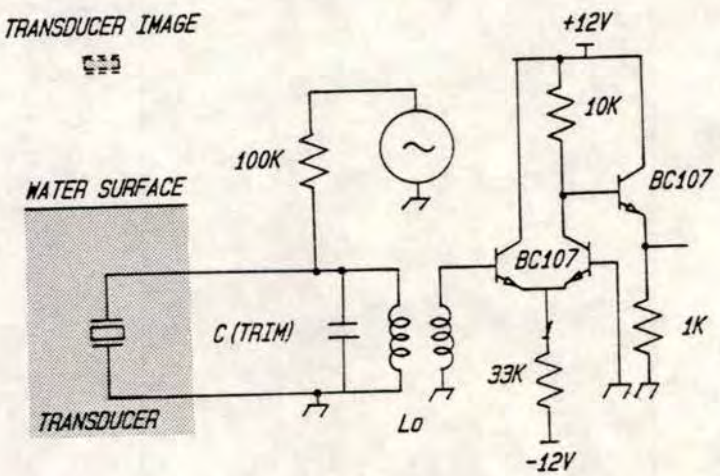

Figure 4.18(a): Experimental setup to measure the self-reciprocity of a matched transducer.

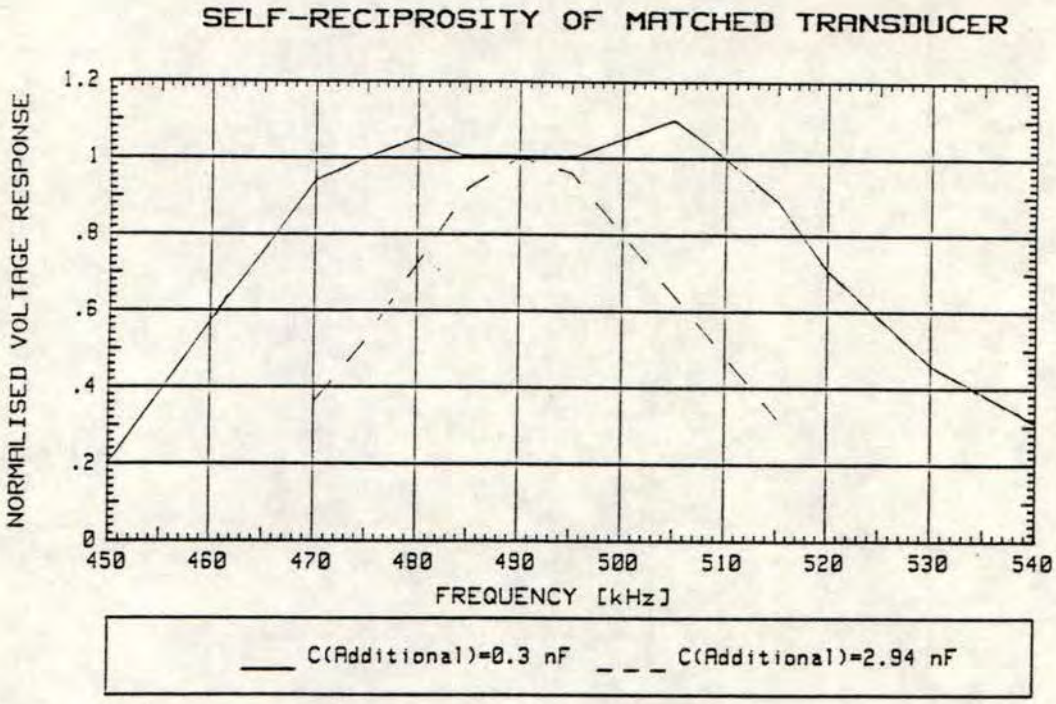

Figure 4.18(b): Frequency response of tranducer for different matchings.

These results compare favourably with the predicted bandwidths as shown in Table 4.1

TABLE 4.1:

MATCHING INDUCTANCE	TRIMMING CAPACITANCE	EXPERIMENTAL BANDWIDTH	THEORETICAL BANDWIDTH
140 µH	0.35 nF	57 kHz	63 kHz
32 µH	3.01 nF	22 kHz	20 kHz

The noise performance of the front-end amplifier was difficult to assess with any great accuracy. However, measurements made indicate a noise figure of approximately 2 dB which is that specified for the input transistor.

4.3.4. Preamplifier and Zero-crossing Detector

Due to the similarity in operation of the wideband amplifier and hard-limiting device for this system to standard frequency-modulated radio subsystems, minimal further development was required. The preamplifier and zero-crossing detector, shown in the

schematic block diagram form in Figure 4.19 and described in detail in Appendix B, consists of three commercially available integrated circuits.

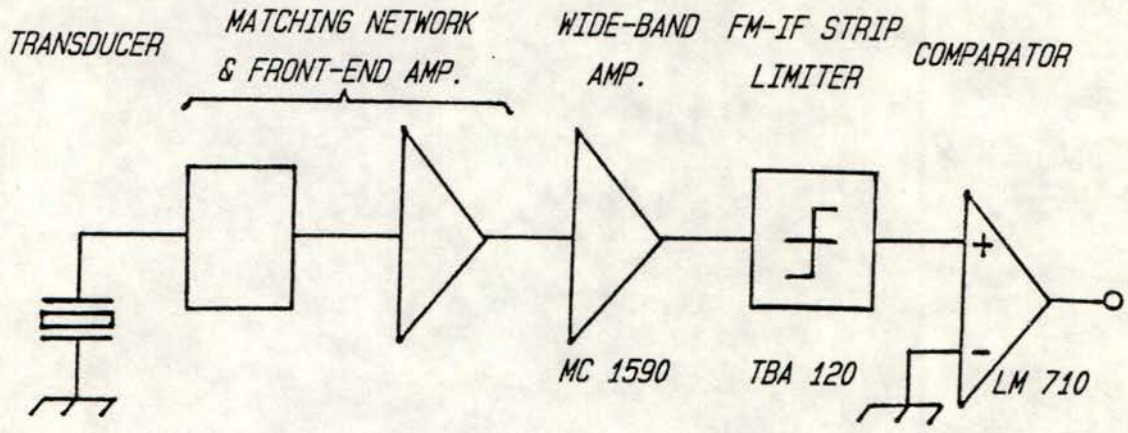

Figure 4.19: Schematic diagram of the whole preamplifier and zero-crossing detector circuit.

4.3.5. Conclusion

The techniques described for matching and low-noise front-end amplifier design proved to be very successful and have been used in the development of other sonar systems in the Central Acoustics Department, UCT.

The photograph in Figure 4.20 illustrates the operation of the amplifier and zero-crossing detector on band-limited noise. The bottom trace shows the clipped signal resulting front zero-crossing detection of the linearly amplified noise shown in the top trace.

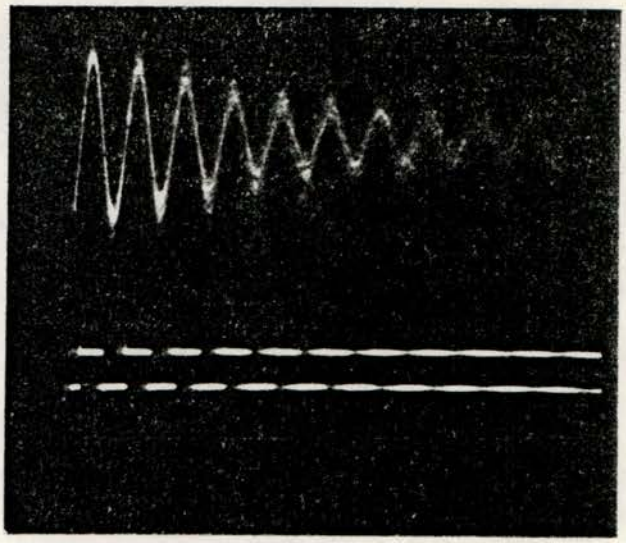

Figure 4.20: Photograph illustrating the operation of the zero-crossing detector on bandlimited noise.

4.4. System Sequencer

4.4.1. Introduction

Active sonar system are said to echo-range on their targets. That is, the range is inferred from the time elapsed between transmission and echo returns.

The simple relationship;

$$t = \frac{2r}{c} \tag{4.16}$$

where t is the elapsed time, r the range and c the sound speed in water relates range to the two way propagation time implicit in active sonar. Equation 4.16 also embodies the trade-off of maximum operating range and the minimum delay between transmissions.

For a maximum operating range of R_{max} clearly a second transmission pulse delayed by less than;

$$T_{min} = {}^{2}/_{c}\ R_{max} \tag{4.17}$$

would result in ambiguous range measurements.

There is thus a need for a device that controls the interpulse period and in general provides an accurate timebase for ranging and synchronisation of the entire system.

4.4.2. System Sequencer

The requirements of the sequencer were extended to provide the following timebases:

(a) Interpulse period
(b) Transmission pulse period
(c) Receive gate delay
(d) Receive gate width.

The nature of these time intervals must be examined in the context of their application before committing the design procedure to any analogue time circuit.

What is in question at this point is the degree to which these periods are to be synchronised to the sampling intervals.

For the purposes of system synchronisation this subsystem provides two synchronising signals.

(a) System clock
(b) Sample pulse.

The system clock is provided by an external 16 MHz square wave signal generator. The sequencer conditions this input to a TTL compatible clock signal with a Schmitt trigger inverter which drives a further hierarchy of inverters to increase the fanout.

The sampling pulse is derived from the system clock, as shown in Figure 4.21, and initiates the acquisition of a sample every 10μs.

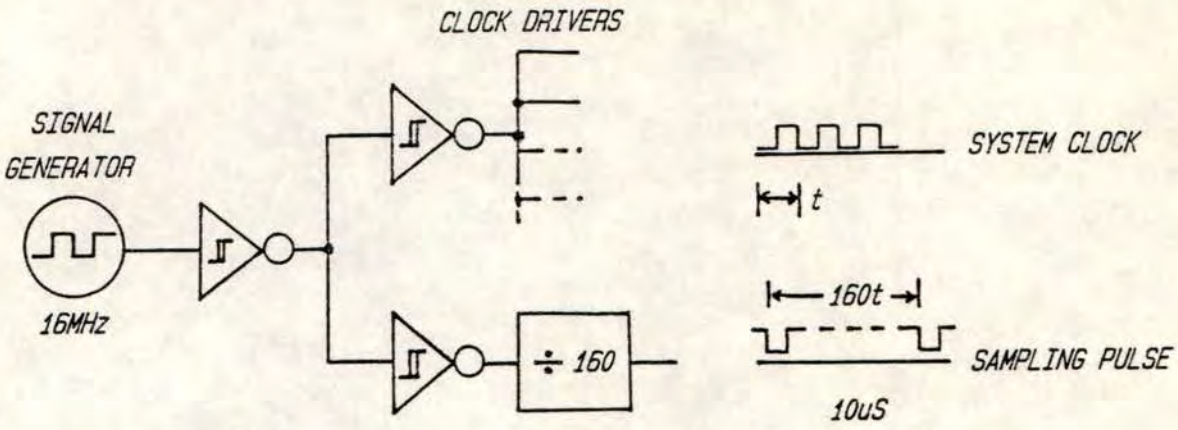

Figure 4.21: System synchronisation signals.

Returning to the question of sequencer synchronisation, the approach adopted in the generation of each time interval is discussed below:

(a) The interpulse period is generated by a digital monostable timer with an analogue time constant that can be varied over a 50 to 1 ratio. This variation in pulse repetition frequency is achieved by adjusting a potentiometer available as a sonar operating control.

Despite the dependence of the time constant duration on analogue circuitry, synchronisation with the sample signal is achieved simply by synchronous triggering and sampling of the timer.

This in effect results in an interpulse period lasting an integral number of sample intervals which commences at a sampling instant.

(b) The transmission pulse period is initiated by the onset of the interpulse period and is sustained for the required time by a monostable timer. No requirement for further synchronisation was deemed necessary.

(c) The function of receiver time gating has been introduced in Chapter 2. The receiver gate delay is synchronised with respect to both the start of transmission and the sample signal. The timer, triggered by the already synchronised transmit period is sampled by the sample signal to ensure that the receiver gate delay ends precisely at the beginning of a phase sample interval.

(d) The width of the receiver gate signal was chosen to be an integral number of samples long and is initiated at the end of the gate delay period. Synchronisation of the timer is acieved once again by sampling its output at the sampling interval.

Table 4.3 below shows the ranges over which each of the above intervals are adjustable and Figure 4.22 demonstrates the interrelation of the above sequencer outputs.

TABLE 4.3:

SYSTEM INTERVAL	TIME PERIOD	
	MIN	MAX
Interpulse period	4 ms	200 ms
Transmission pulse period	2 μs	100 μs
Receiver gate delay	2 ms	100 ms
Receiver gate width	100 μs	5 ms

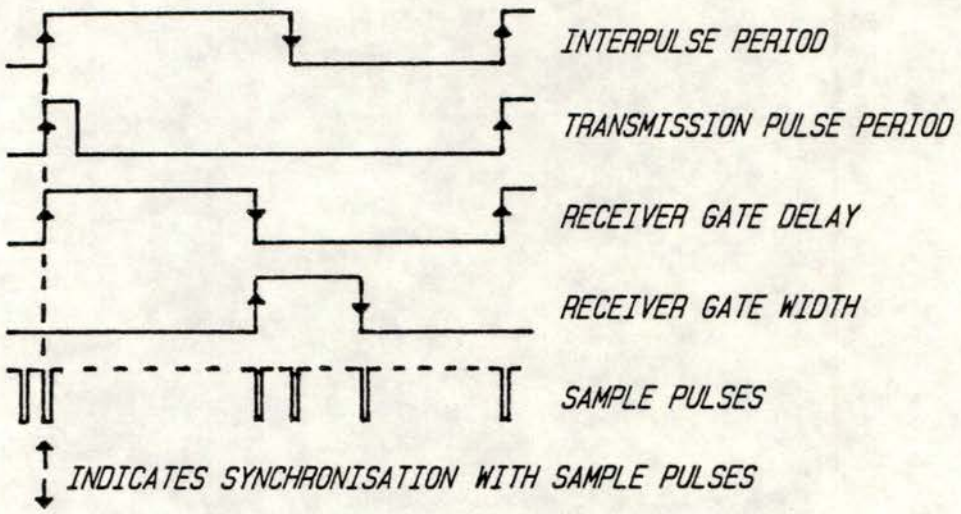

Figure 4.22: Timing diagram for the system sequencer.

4.4.3. Conclusion

Appendix B contains the detailed circuit diagram of the system sequencer with the algorithm controlling its operation.

4.5. Digital Phase Meter

4.5.1. Introduction

The rapid and accurate measurement of electrical phase angle is crucial to the operation of this sonar system since the location of targets is determined solely by the phase information of the narrow-band echo signals.

This section will consider the requirements of the phase measuring device, review alternate phase measuring techniques and describe the operation of the final subsystem utilised.

First however, a constraint in the definition of phase should be introduced and put in perspective with respect to the applicability of "phase measurement" in this system (Reference 22).

Strictly, relative phase is only defined for two sinusoidal waveforms of identical frequency. For example, two signals A cos $(\omega t+\phi)$ and A cos (ωt) have a relative phase angle of ϕ. The phase angle ϕ is in fact periodic in 2π radian intervals since ϕ and $(\phi + 2\pi n)$, n an integer, are indistinguishable for sinusoidal functions.

Consider on the other hand an arbitrary waveform, f(t), repeated at intervals of duration T. That is, for all n:

$$f(t) = f(t+nT) \tag{4.18}$$

A second signal described by the equation $f(t-\tau)$ would be identical to the original signal except for a time translation τ.

A mutual phase displacement could be said to exist and is defined as:

$$\phi = 2\pi \frac{\tau}{T} \tag{4.19}$$

Analogous to sinusoidal functions there is a periodic mutual phase displacement between two time translated signals, again with a 2π radian interval. This phenomenon will be returned to later is this section since it could lead to ambiguity in bearing measurement.

For this system, the nature of the shape of the waveform (f(t)) and the zero-crossing method of mutual phase displacement measurement makes it possible to ascribe the quantity "phase angle" meaningfully.

4.5.2. Phase Measurement Requirements

An insight was gained in Chapter 3 into the structure of the returning echo signal where it was seen to be composed of a series of image pulses, each originating from a highlight in the insonified field.

In an attempt to increase the probability of non-overlapping echoes the transmission pulse is, at times, shortened to a tone burst of twelve wavelengths. The duration of a received image pulse is thus approximately 25μs. In view of this it was considered adequate to sample the measured phase difference every 10μs. (This time sampling corresponds to a range sample no larger than half the range resolution of the system.)

Returning to the structure of the acoustic echo. Due to the discrete nature of image pulses, the spatial separation (in both range and bearing) of successively illuminated highlights, could result in the relative phase angle of the signals for a pair of receiver elements varying rapidly from one echo to the next.

While the phase angle changes for successive highlights, it remains constant for the duration of the individual image pulses. Thus the phase measuring device is required to retain no information of the angles measured over previous sample periods, however throughout the sample window the instantaneous phase measurements should be integrated.

Figure 4.23 shows a hypothetical example illustrating the concepts of discrete image pulses, phase sampling and phase integration over single sample periods, while retaining no phase history of previous samples.

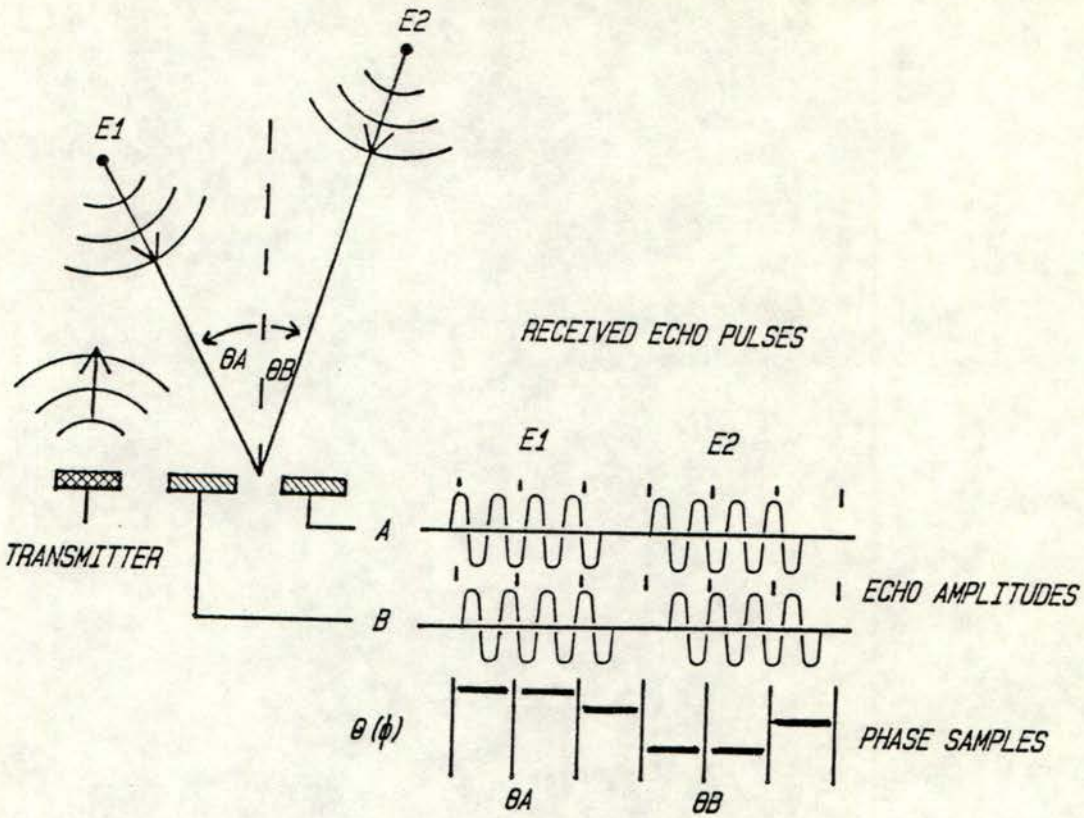

Figure 4.23: A diagramatic illustration of the operation of the phase meter.

The above examples is no more than a conceptual demonstration of the operation of the phase meter. It should be bourne in mind that the signals present at the input to the phase measuring device are square waves retaining only the phase information of the received echo.

4.5.3. Review of Alternate Phase Measurement Techniques

There are many approaches to extracting phase information from two signals, for convenience they have been divided into three categories:

(a) Analogue methods
(b) Compensation/null method
(c) Phase to duty cycle method.

(a) Analogue method

These include the classical phase detectors which make use of either analogue multiplication or differential quadrature vector addition. An advantage of these techniques is that all the information of the input waveform is utilised.

It is the very fact that the output is critically dependant on input signal amplitudes that precludes these methods from being used in this sonar system where the signal amplitude has been destroyed.

(b) Compensation/null method

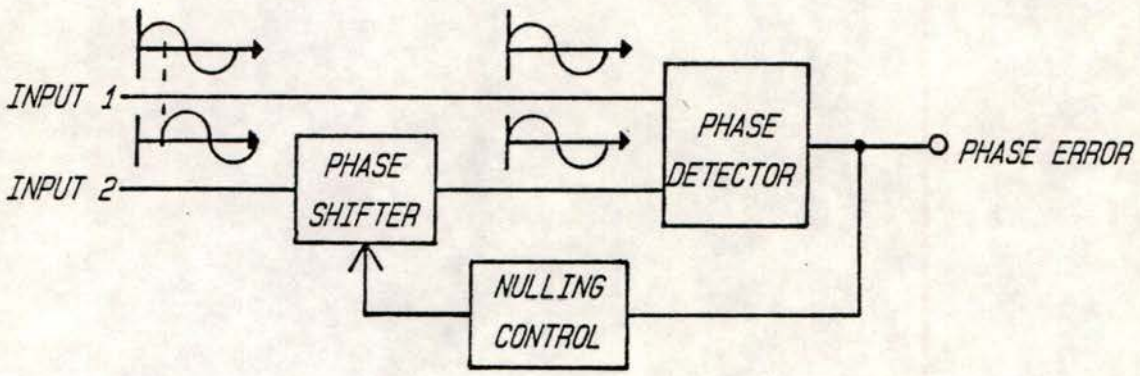

Figure 4.24: Schematic block diagram of a compensation/null phase meter.

The operation of this technique requires that one signal be phase shifted by a known amount until both signals have no relative phase angle or "phase error". The degree of minimisation of this error output contributes to the accuracy of the phase measurement.

To detect the null phase condition usually requires some form of time integration of the phase error signal. This would result in slower response times for the device and introduce an inherent "memory" to the phase measurement, neither of these effects satisfy the requirements expressed in Section 4.5.2.

(c) Phase to duty cycle method

This method is ideally suited to the measuring of mutual phase displacement of hard-limited signals where the phase information is contained in the instants of zero-crossing. The technique offers three distinct advantages:

(i) Linear conversion of phase.
(ii) Direct conversion to a digital phase output.
(iii) The "instantaneous" nature of the phase measurement allows flexibility in overall phase sampling.

The phase to duty cycle conversion is achieved by causing the rising edge of one of the two signals to set a latch while the rising edge of the other signal resets the same latch. The duration of the latch set period is thus equal to the phase delay of the second signal with respect to the first signal.

The phase is, in effect, sampled at the signal frequency since the conversion occurs once for every cycle of the received signals. Direct digitisation of the phase follows by gating a high frequency clock with the latch output and counting the number of clock pulses in a duty cycle.

Figure 2.25 shows a schematic diagram of the phase detector and illustrates its operation by means of a timing waveform.

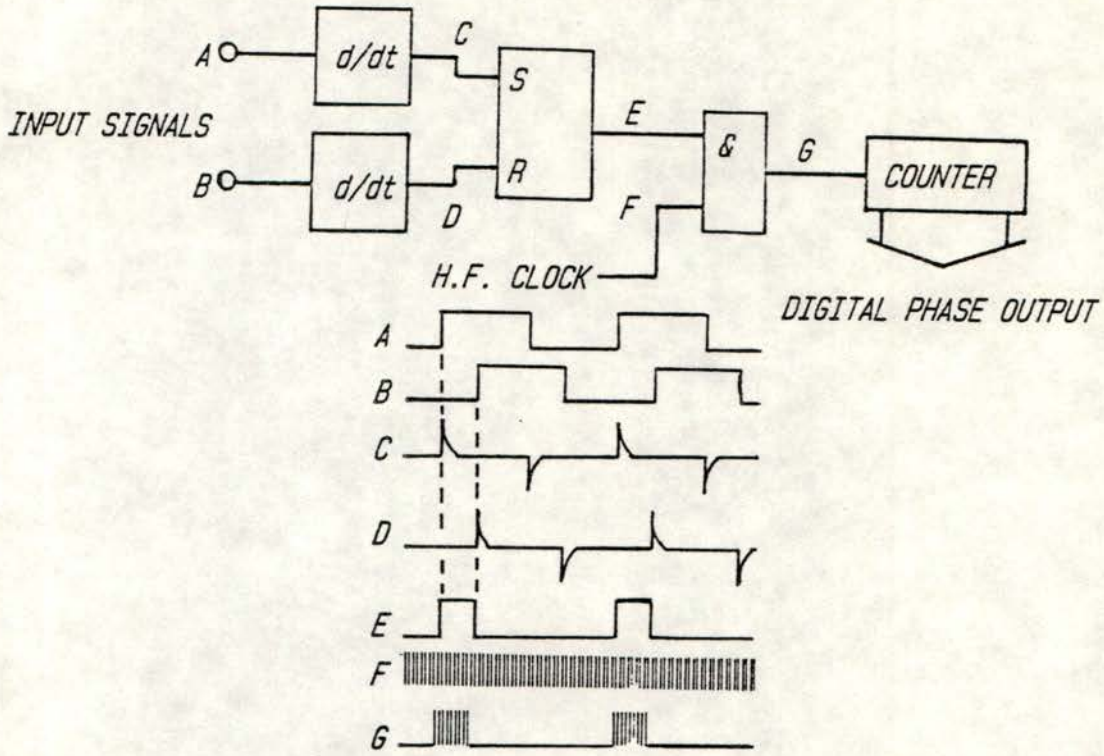

Figure 4.25: Schematic diagram illustrating the operation of the duty cycle method of phase measurement.

4.5.4. Digital Phase Meter

Several points should be noted with regard to the phase measurement as depicted in Figure 2.24, especially when considering its practical implementation.

(a) A reading of the "instantaneous" phase is available at the output roughly every two microseconds.

(b) The phase conversion occurs concurrent with the input signals, which arrive at the receiver asynchronous with respect to the systems internal sample timebase.

(c) The requirements of this device (Section 4.5.2) call for the synchronisation of the phase data with respect to the sample interval.

This need, and the integration requirement for the phase data, are both met in the final design by summing the phase of the first three delay duty cycles in each sample interval. At the end of the system sampling interval the total phase output is stored in a register for subsequent processing while the phase counter is reset in preparation for the next interval.

Figure 4.26 shows the measured phase as a function of the mutual phase displacement of the signals. The output has a 2π periodicity, as previously explained, and reaches a maximum phase value when signal B is delay by $2n\pi$ radians relative to Signal A. At this point the high frequency clock would virtually be ungated for the duration of three signal cycles. Since the signal frequency is 490 kHz, the maximum clock count would be:

$$\Phi_{max} = 3\left[\frac{1}{490\ kHz}\right] \quad 16\ MHz$$

$$= 98 \text{ counts.}$$

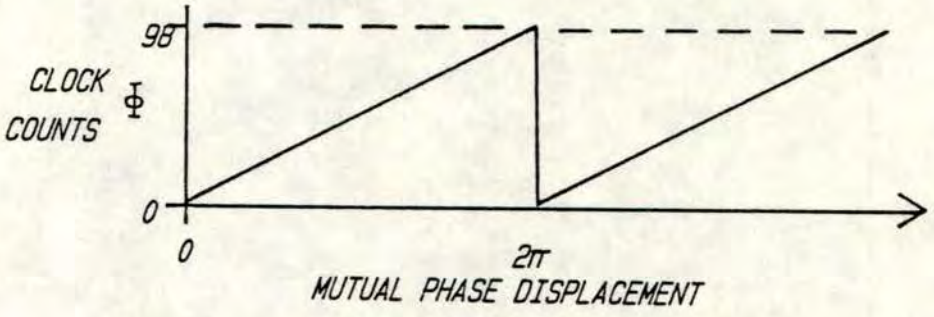

Figure 4.26: Phase meter output as a function of mutual phase displacement.

(d) The following observations require a knowledge of the relationship between target bearing and phase information.

Figure 4.27 shows a plane wave incident on a transducer pair where, owing to the angle of incidence, there is a delay in the time of arrival of the wavefront at transducer B with respect to transducer A.

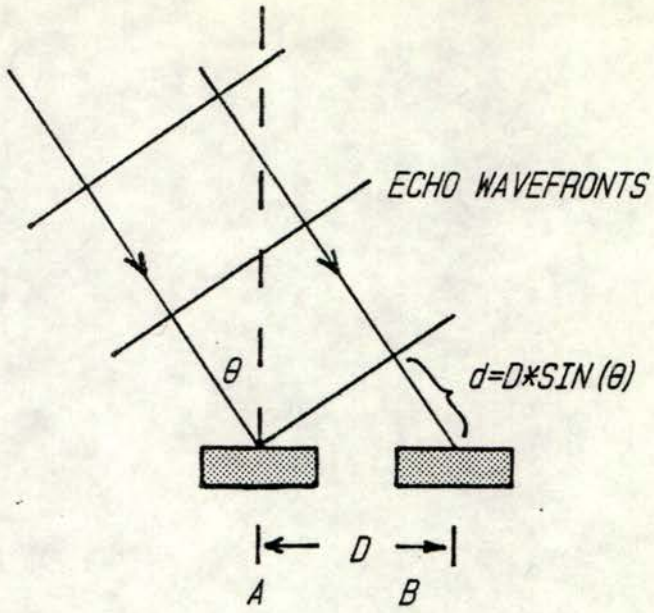

Figure 4.27: Mutual phase displacement for a transducer pair.

The mutual phase displacement in this case would be;

$$\Phi_{AB} = \frac{2\pi}{\lambda} D \sin \Theta \qquad (4.20)$$

where D is the distance between the centres of adjacent transducers, λ is the wavelength of the signal in water and Θ the bearing of the incident plane waves.

Figure 4.26 could easily be modified by rescaling the x-axis to relate the output measured phase to the angle of incidence of echoes at the transducer face.

(i) The first observation is that no unique bearing can be inferred from an output phase measurement for the two signals should the signals vary in phase by more than 2π radians.

To prevent this ambiguity in bearing determination, it was required to limit the source of echoes to a sector over which the mutual phase displacement is limited to 2π radians. This is achieved by using a transmitter with a directional illumination pattern.

(ii) The second observation assumes that the output phase does not exceed one cycle. (In fact for a symmetrical sector of operation the input phase would vary from $-\pi$ to $+\pi$ radians.)

Consider the output of the phase meter for a target echo lying on the transducer boresight, that is, at a bearing of zero degrees. Ideally the resulting measurement should yield zero clock counts. However, in the presence of noise the resulting jitter in the moment of zero-crossing of the amplified transducer signals could cause the measured phase to rapidly fluctuate between zero and maximum clock counts.

This potentially inconsistent bearing output was avoided by prebiasing the input phase angle of one signal by $-\pi$ radians.

From Eqn 4.19 it is seen that a delay of τ where;

$$\tau = \frac{T}{2}$$
$$\approx 1\ \mu s \qquad (4.21)$$

will yield the required bias.

Implementing all of the above modifications yielded a final design as shown in block form in Figure 4.28.

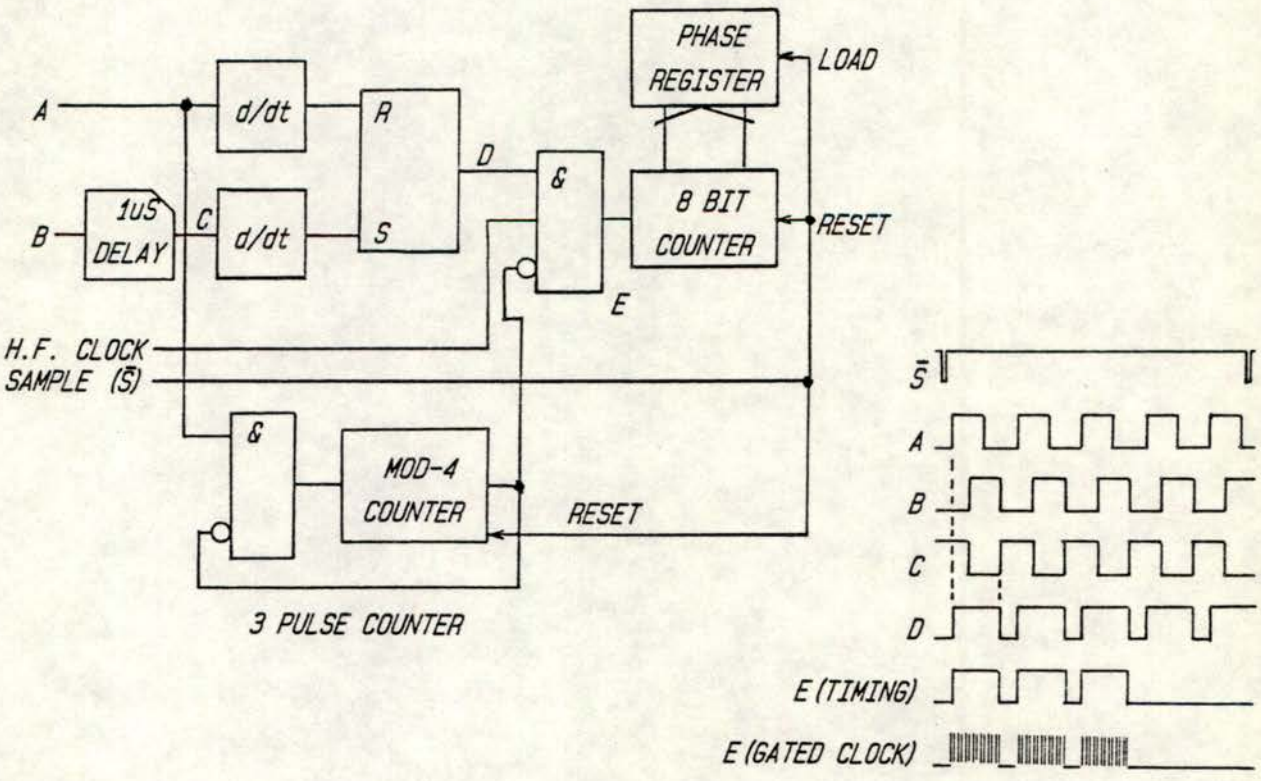

Figure 4.28: Schematic block diagram illustrating the operation of the digital phase meter.

(e) This final point expresses the angular limitation of the sonar operating sector outside of which bearing ambiguity arises.

The phase angle between the two input signals is limited to π or $-\pi$ radians which, by substituting into Eqn 4.20, corresponds to a maximum unambiguous bearing of:

$$|\theta_{max}| = \arcsin\left(\phi_{max}\frac{\lambda}{2\pi D}\right)$$

$$= 8.8°$$

Thus the measured output phase is proportional to the sine of the echo bearing. However, since the largest bearing deviation is relatively small, this measurement is (within acceptable error) directly proportional to the bearing itself.

To demonstrate this point the worst-case error introduced by this assumption, expressed as a ratio of the true bearing, is calculated below:

$$\in(\theta_{max}) = \frac{\theta_{max} - \arcsin(\theta_{max}))}{\arcsin(\theta_{max})}$$

$$= 0.004$$

Using this simplification, the bearing of an echo is simply:

$$\theta = 8.8\left[\frac{\phi-49}{98}\right] \quad [DEG]. \tag{4.21}$$

Figure 4.29 shows the relationship between bearing and phase meter output over the unambiguous sector. Note that this relationship is in fact a staircase function where the step size is the minimum quantisation increment of the meter, which is related to clock counts.

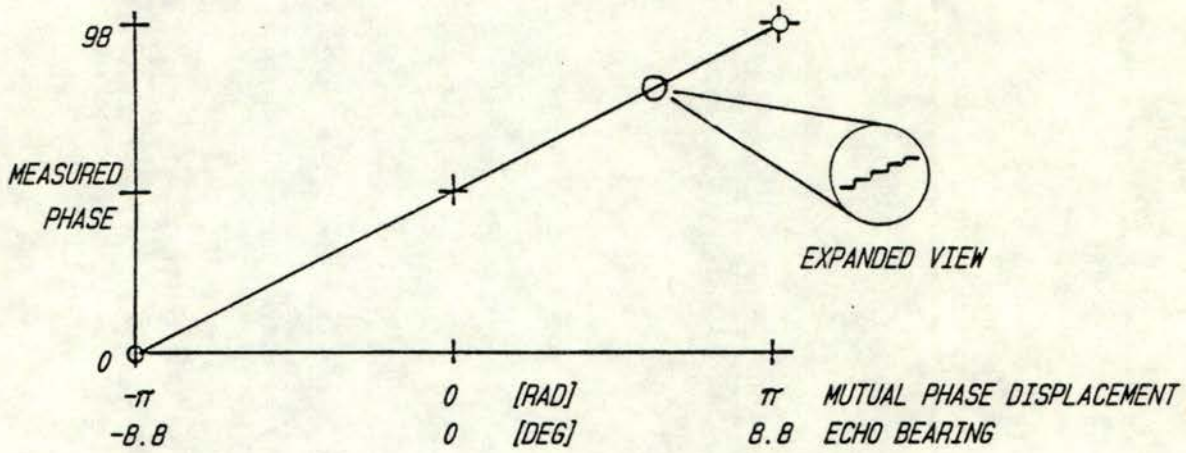

Figure 4.29: Graph showing the relationship between bearing, or mutual phase displacement, and the output from the phase meter.

4.5.5. Results

The operation of the phase meter was verified by testing it "in situ" with the sonar as developed thus far. The experimental setup is outlined in Figure 4.30 and the results obtained from two azimuth-measuring pairs of adjacent transducers are shown in Figure 4.31(a) and Figure 4.31(b).

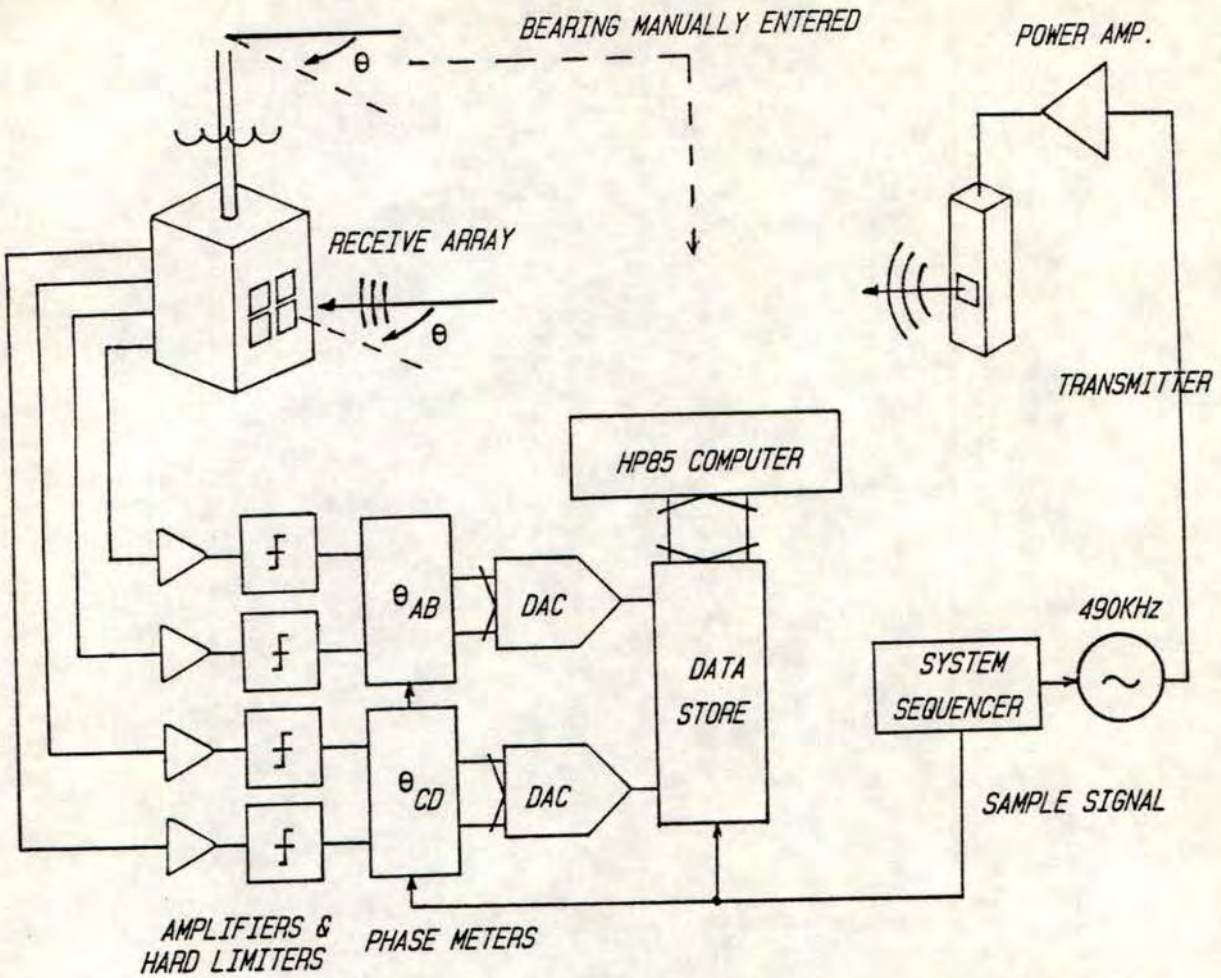

Figure 4.30: Experimental setup used to verify the operation of the phase meter.

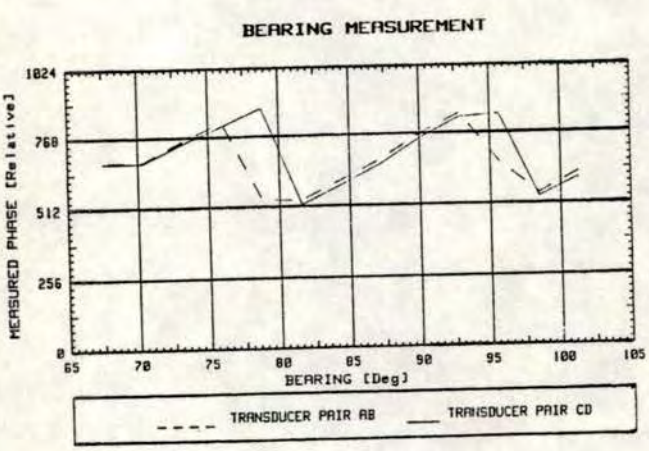

Figure 4.31(a): Phase output over a broad sector.

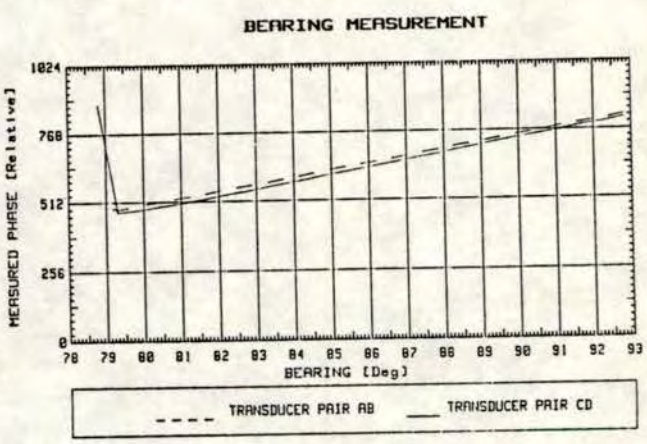

Figure 4.31(b): Phase output over the unambiguous sector only.

Figure 4.31(a) shows clearly the periodicity of the phase measurements and hence ambiguity arising from an insonified target outside the limited operating sector of the system. Figure 4.31(b) demonstrates, in finer detail, the performance of the phase meter for the sector of interest.

The following characteristics of the meter's operation are noteworthy:

(i) Excellent linearity over a sector of about 14°.

(ii) Excellent agreement between the two parallel pairs of transducers.

(iii) There is an offset of about 0,9° between the two lines, or sets of results. This systematic error is probably due to slight variations in the depth of mounting of the individual transducer elements in the array and non-alignment is the electrical phase of the various channels. (Provision is made in the subsequent data processor to correct constant offset errors.)

(iv) Since this is the first opportunity to examine the transducer and receiver operating together, it is important to note that there is minimal mutual coupling between elements of the transducer array. Furthermore no difficulties with electrical coupling in the high gain amplifier and hard-limiter combinations were encountered. These observations are supported by the linearity of the measured phase with bearing variation.

4.5.6. Conclusion

As far as could be established the phase measuring circuit fulfilled the criteria set in the requirements section (Section 4.5.2).

The detailed operation of the digital phase meter is presented in Appendix B.

4.6. Data Processor

4.6.1. Introduction

Whereas the phase meter performs location on the received signals, it is the function of the data processor to undertake the detection of signals present in the measured phase sample.

The performance of a sonar system is heavily dependant on the operation of its detection process. Detection threshold, for instance, determines the probability of detection and of false alarm. Given a relaxed threshold the image generated on a sonar display would be noise cluttered, whereas a stringent detection threshold could lead to excessive target rejection.

Detection in this system takes place in the form of a decision-making process operating in real time on the four simultaneously available phase samples. This section deals with the decision strategy/criteria and its implementation in a small hard-wired digital data processor.

4.6.2. Detection: A Decision Strategy

What should be bourne in mind when considering the operation of this detector is the functional element that it replaces in the conventional sonar system.

Figure 4.32 shows, in block form, elements of two sonar system:

(a) A conventional sonar with post-beamforming detection using an amplitude threshold.

(b) The 3-D sonar data processor operting as a detector on time dependant bearing inputs.

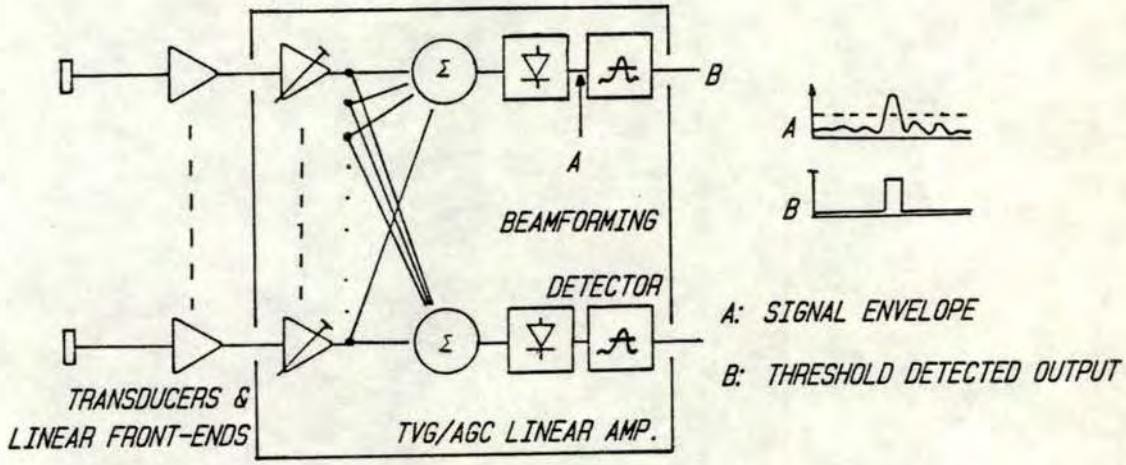

Figure 4.32(a): Schematic block diagram of a conventional beamforming sonar.

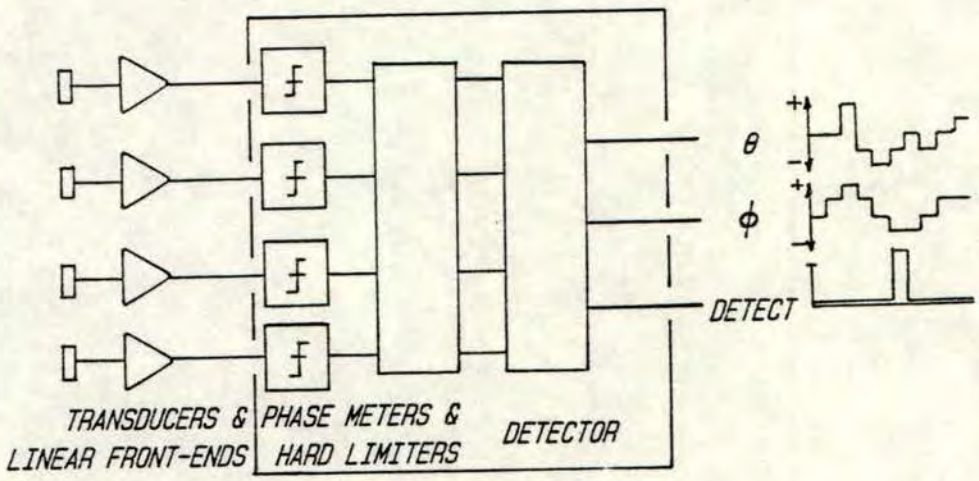

Figure 4.32(b): Comparative schematic block diagram of the 3-D sonar.

A superficial comparison of these systems shows clearly the difference in the requirements of their respective detectors.

(i) In Figure 4.32(a) the preformed beam of steering angle Θ_i has output information pertaining (mainly) to echoes lying on bearing Θ_i. It is then the function of the detector to differentiate, and possibly enhance, the presence of a signal against the background noise usually on an amplitude basis.

(ii) In Figure 4.32(b) similar detection is made difficult by the phase measuring technique adopted in this system. When the hard-limiting amplification destroys the amplitude information it is no longer immediately obvious whether a phase sample is derived from an echo signal or from clipped random amplifier noise.

(iii) Since no prior beam forming in the signal processing of the received signal has been undertaken detection implies more a test of validity of bearing information, than merely the presence of a target.

(iv) The operation is further aggravated by the broad sector insonification found in this system which results in overlapping return echoes yielding false bearing measurements.

(v) The benefit of simplicity is however very obvious when comparing the equivalent functional blocks delineated.

A nomenclature change has been introduced in Figure 4.32(b) which will be followed throughout this and subsequent sections. In assigning variables to the phase measurements made by the phase meter, bearing values describing azimuth are denoted by the angle θ. Similarly elevation angles are denoted by ϕ.

The assessment of "validity" of the bearing measurements must be seen in terms of both what should be accepted and what should be rejected in the decision process.

An acceptable sample would consist of bearing values measured in the presence of a single target echo at the receiver, of sufficient signal strength to ensure a relatively noise free sample. Under these conditions the two azimuth measurements made on the parallel pairs of transducers should be identical. The same holds for the elevation measurements.

On the other hand, invalid bearing information could be the result of either of the following two conditions, both displaying characteristic effects on the phase measurements.

(i) A very weak signal buried in noise at the input would yield uncorrelated and meaningless phase measurements. This condition would be indicated by random fluctuations in the difference in phase measured for parallel pairs of transducers.

(ii) Multiple overlapping echoes incident at the transducer array would yield phase measurements gleaned from the resultant of the interfering acoustic fields. Bearings measured in such a field would vary from point to point across the array.

In both cases the process of spacial sampling over the array aperture highlights the presence of unacceptable bearing information.

4.6.3. Detection: Implementation of the Decision Strategy

The action of the detection process can be summarised as follows:

The existence of the required single wave-front condition is checked by ensuring that the pair of azimuth measurements, as measured on the two parallel pairs of transducers, are closely the same. An adjustable threshold is applied to set a maximum permissible difference. Similarly the pair of elevation measurements are subject to the same maximum deviation beyond which the bearing information is regarded as unreliable.

Detection only takes place if, for a sample, both pairs of bearing data satisfy the threshold requirement.

A small hard-wired data processor was designed to implement the above strategy. Figure 4.33 summarises the operation of the processor by means of a schematic diagram.

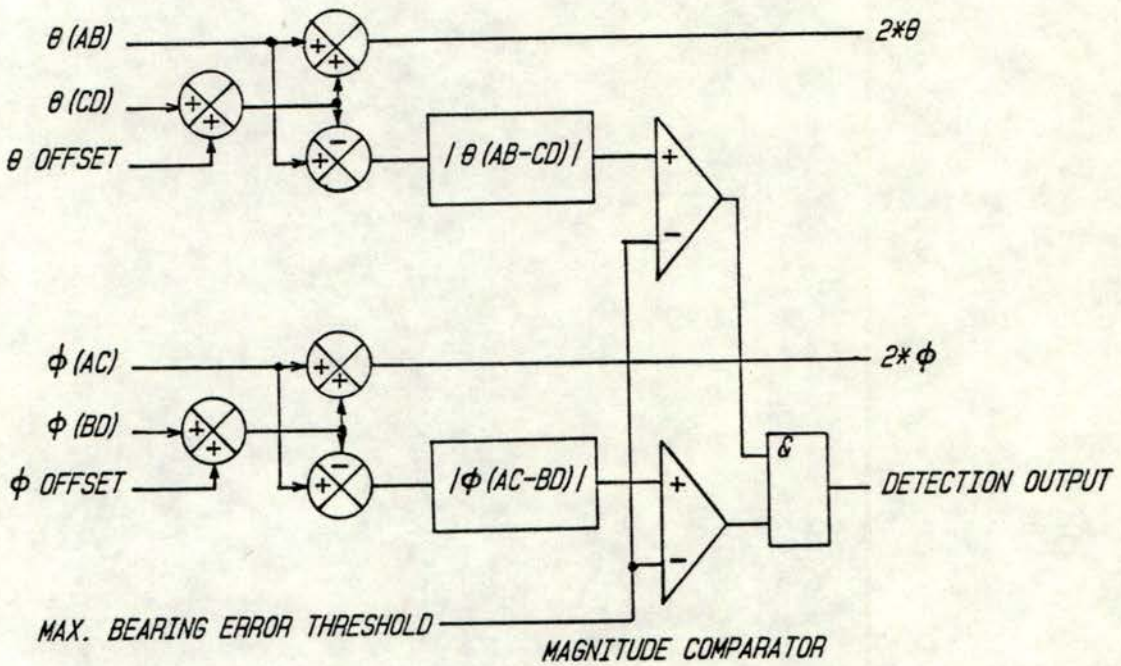

Figure 4.33: A schematic diagram illustrating the operation of the data processor.

Although Appendix B gives a detailed account of the design and circuit operation of the processor, certain features warrant mention at this point.

(i) Provision is made for the correction of a small systematic offset in parallel phase measurements.

(ii) Since this is a combinational-logic digital device, it requires no synchronisation. Apart from a short settling time for gate propagation delays the output can be considered to be instantly available.

(iii) To improve the accuracy of the bearings output to the display module, the azimuth and elevation measurements are averaged.

4.6.4. Conclusion

No attempt was made at the point to assess the "noise" rejection of the detector. Its binary operation was rigorously tested and the operation of the system as a whole was examined.

4.7. Amplitude Threshold Comparator

4.7.1. Introduction

Besides the input preamplifier, this is the only circuit to operate on the amplitude of the acoustic backscatter. As such its task is to assist in the detection of the echoes by the rejection of phase information measured on amplifier background noise in the absence of acoustic signals.

Its application also helps to discriminate against acoustic glint from large targets (Reference 23). The phenomenon arises when "crinkled" backscatter wavefronts appear to originate from a bearing other than that of the target. (A similar mechanism occurs in radar tracking from which the term glint is borrowed.) The effect becomes most significant when the resultant of the contributing echoes is small in magnitude and can therefore be rejected along with noise.

The limited amplitude dynamic range of operation required by this circuit extends only from the noise level to the amplitude threshold level. It does therefore not compromise the inherent advantage of the phase-only sonar in the presence of a large echo amplitude dynamic range.

4.7.2. Amplitude Threshold Comparator

To determine phase, the outputs of the individual transducers are infinitely clipped and the phase digitised by gated counters. However before the clipping stage, where all the amplitude information is lost, there is a linear front-end amplifier of nominal but constant gain. At this point an output is taken from one channel, envelope detected, and then compared against an amplitude threshold settable from 0 to 20 dB above the amplifier noise level.

Figure 4.34 demonstrates the operation of the amplitude threshold comparator by means of a schematic block diagram and time waveforms.

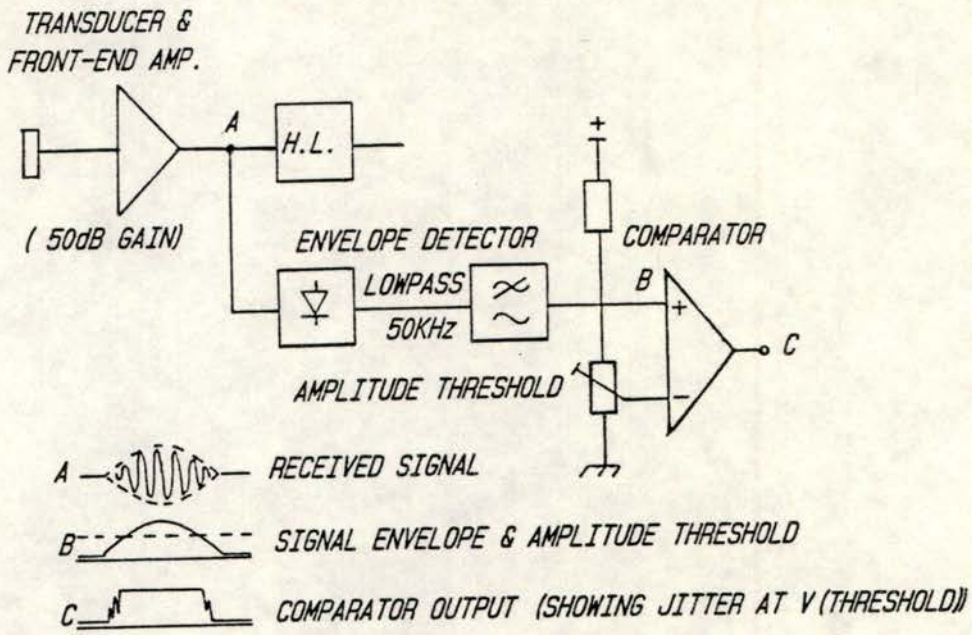

Figure 4.34: Schematic block diagram of the amplitude threshold detector illustrating its operation.

4.7.3. Output Synchronisation

Before describing the sampling and synchronisation of the circuit described by Figure 4.34 the relative output timing of the phase samples should be examined.

At the sampling instant the phase sample, acquired throughout the preceding sample interval, is stored in a register for display during the subsequent sample period. It is during this subsequent sample period that the various detection thresholds act upon the bearing information (which produces the display deflection (Sec 2.4)) by blanking the screen for the duration of rejected samples.

Obviously it is essential to coincide the threshold outputs with the phase display timing. The data processor, as mentioned previously, is an asynchronous device operating directly on the information in the phase registers and thus require no synchronisation.

Since the displayed bearing reflects the average phase measured during the previous sample interval, the amplitude threshold comparator should be sampled half-way through the phase acquisition period.

A delayed sampling-instant marker, available from the display generating circuit, is used to trigger an amplitude sample every sample period at the half-interval moment. This is again resampled by another flip-flop at the sampling instant thereby effectively delaying the amplitude threshold signal by half a sample interval.

Figure 4.35 traces the sequence of operations and their timing for a single phase sample from acquisition to display.

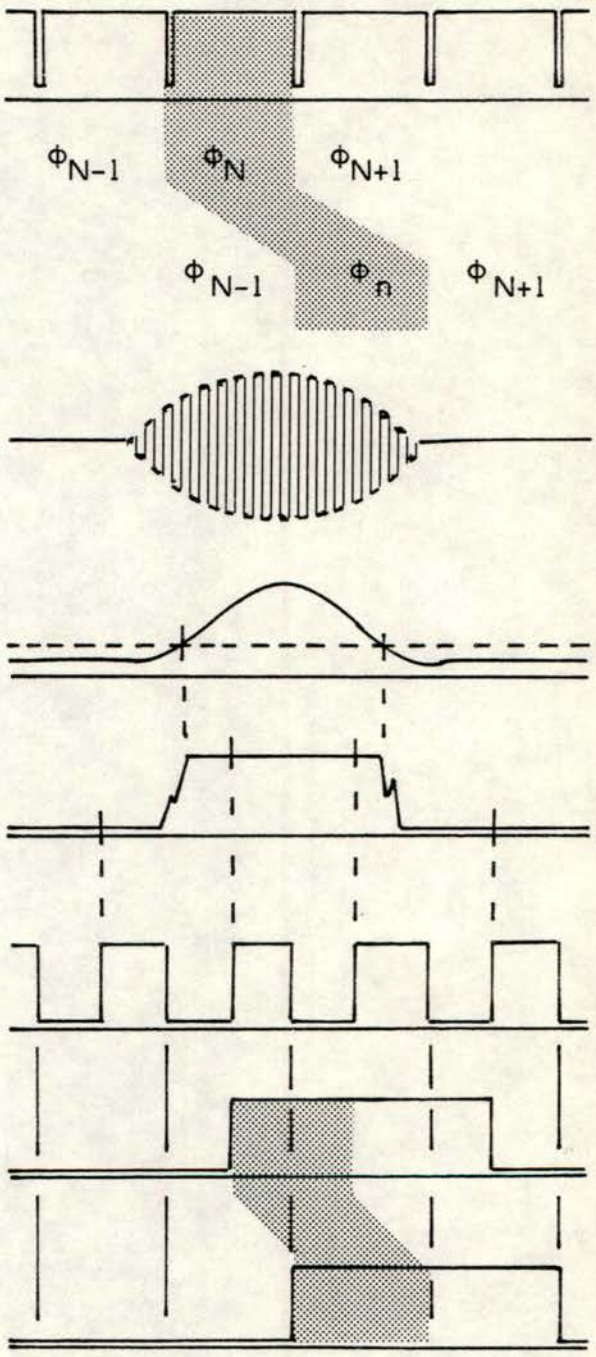

Figure 4.35: Timing diagram showing the synchronisation of the amplitude threshold detector with the display of phase samples.

4.7.4. Conclusion

Appendix B contains a detailed circuit diagram and description of operation for the amplitude threshold comparator.

The effect of amplitude threshold variation was investigated and the best compromise between loss of signal information and noise rejection was experienced for an amplitude threshold setting approximately 6 dB above the system noise level. It is however gratifying to note that even with this amplitude set at a minimum, implying that even amplifier thermal noise passes this test, the data processor detection rejected most of the spurious bearing samples caused by noise.

4.8. Display Generator

4.8.1. Introduction

This sonar system falls into the generic class of imaging sonars. Collins dictionary defines the term "image" as a "visual impression of something produced by a lens etc". Clearly the effectiveness of this class of sonars is then the likeness of the displayed image to the insonified field. This calls for the full usage of all the information extracted from the acoustic sector by the sonar display.

A θ-ϕ display technique was chosen and is produced by deflecting the single beam of an oscilloscope in the x-direction by the measured azimuth and y-direction by the measured elevation for each phase sample. The trace is synchronously blanked for samples failing the detector thresholds as the spot flies rapidly from one sample coordinate to the next.

This display type has the major advantage compared to conventional PPI displays in that it is "as the eye would see it". However, it is wasteful to lose the parameter most easily obtained by sonar which is range.

A novel stereoscopic display was developed, as an extension of the θ-ϕ format, which allows all three dimensions to be displaced simultaneously on a single screen. This section examined alternate display techniques and describes the generation of the real-time stereoscopic display.

4.8.2. Alternate Display Techniques

There were several fundamentally different approaches to the 3-D display requirements that were considered before choosing the stereoscopic presentation.

(a) B-Scan:

A bearing-range scan, B-scan, is easily implemented on a normal oscilloscope with the time base giving the range sweep and the y-deflection the bearing. Target detection is displayed by simultaneously blanking the beam for rejected phase samples.

Two adjacent B-scans, each operating as above, with one oscilloscope channel indicating azimuth and the other elevation displays all the sonar data available. This technique was used extensively as a diagnostic tool during development and improvements of the system. Figure 4.36 shows its implementation.

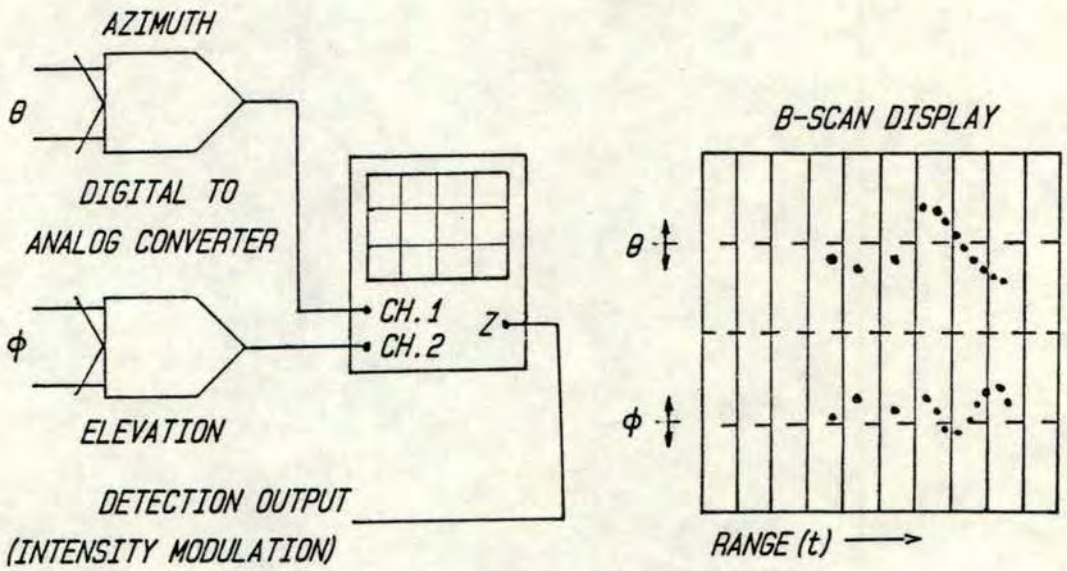

Figure 4.36: Implementation of a B-scan sonar display.

Its value was however realised not as a dual B-scan but rather displaying a combination of a single B-scan and a receiver signal amplitude. Using a delayed trigger with an expanded time base on the oscilloscope, the response of the system to specific echo signals was monitored.

Figure 4.37 shows a photograph of the oscilloscope screen taken during such a test where the accepted targets are significantly brighter than other samples in the picture. Note that only one transmission pulse period was captured to prevent overlaying of subsequent scan samples.

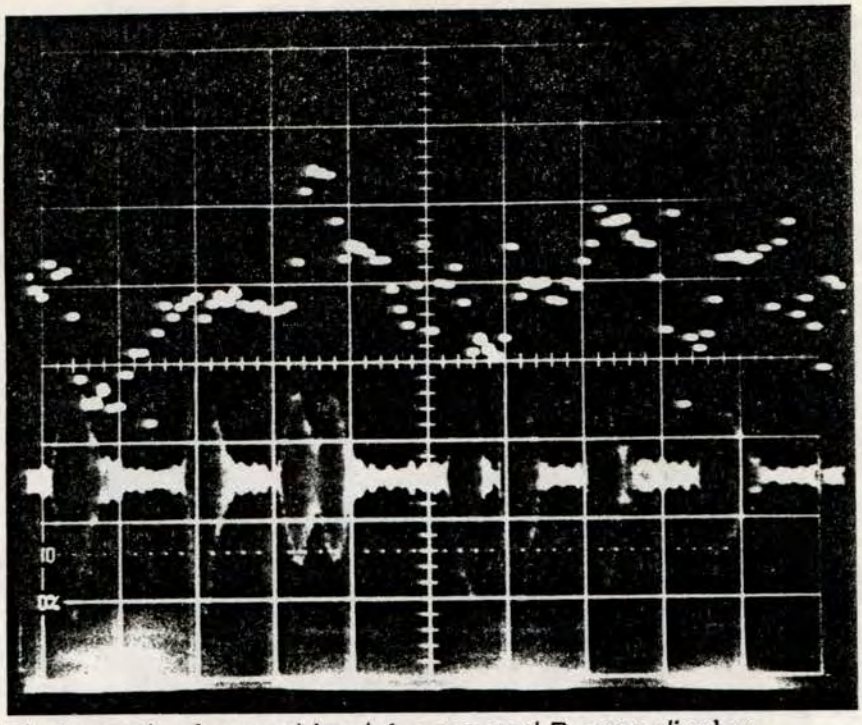

Figure 4.37: Photograph of a combined A-scan and B-scan display.

There are, however, drawbacks to this display type. It is very difficult to mentally combine a target shown on two traces into a single point projected into three dimensional space. Furthermore, if there is any target scintillation present on subsequent B-scans, association of the two bearing measurements for a single target becomes confusing.

(b) PPI Display:

A commonly used fire-control radar display method involves the presentation of the two bearings on "plan position indicator" screens. The only noticeable difference between this display and the preceding B-scan type is the fact that the target location is corrected by true polar coordinate representation.

Figure 3.38 shows this implemented on a single screen with the operational sectors forming pie-sections of a circular display.

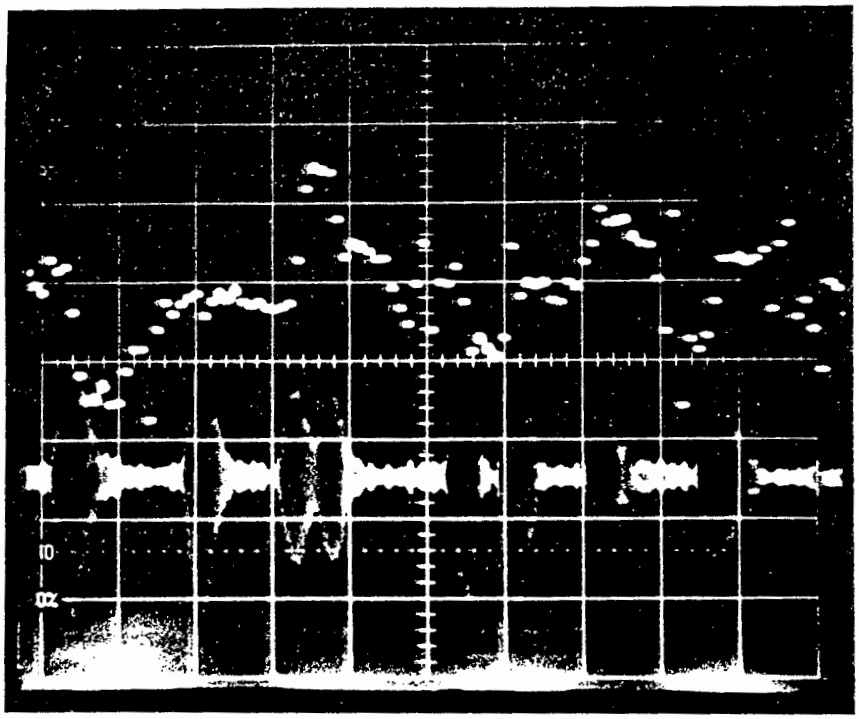

Figure 4.37: Photograph of a combined A-scan and B-scan display.

There are, however, drawbacks to this display type. It is very difficult to mentally combine a target shown on two traces into a single point projected into three dimensional space. Furthermore, if there is any target scintillation present on subsequent B-scans, association of the two bearing measurements for a single target becomes confusing.

(b) PPI Display:

A commonly used fire-control radar display method involves the presentation of the two bearings on "plan position indicator" screens. The only noticeable difference between this display and the preceding B-scan type is the fact that the target location is corrected by true polar coordinate representation.

Figure 3.38 shows this implemented on a single screen with the operational sectors forming pie-sections of a circular display.

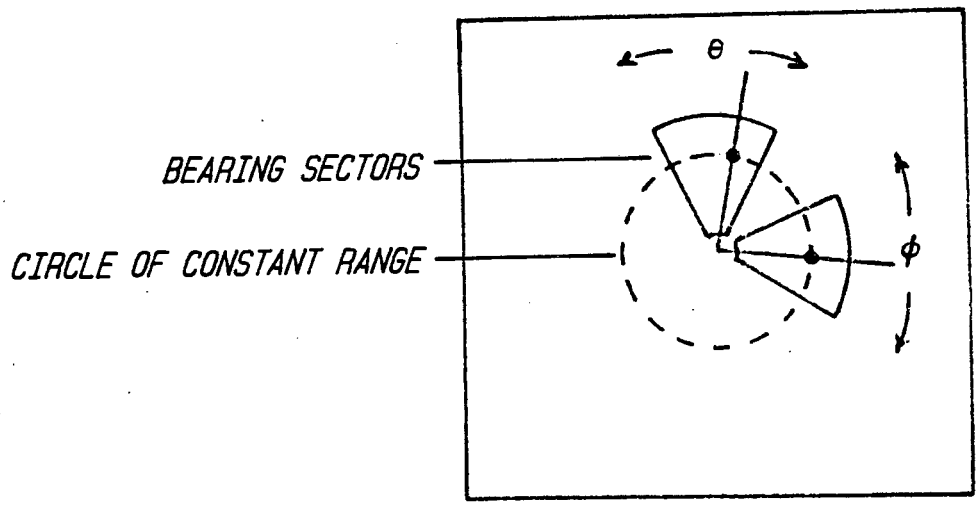

Figure 4.38: Plan position indicator display.

This display suffers the same drawbacks as the dual B-scan screen besides being more difficult to implement.

(c) Θ-ϕ Display:

For a display to faithfully reproduce a visual image, it must reconstruct the original distribution of information on the retina of the observer's eye.

Consider a target A lying on a bearing of Θ relative to "dead ahead" or boresight as shown in Figure 4.39. (The image of this point appears on the retina of the eye at a position determined by the angle Θ). If the target were only a highlight and the display reproduced a dot at A', then the image present on the retina would be identical to that of the real target.

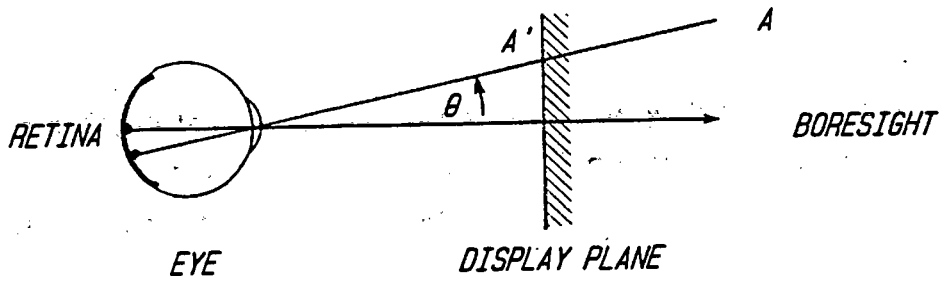

Figure 4.39: Visual image reconstruction.

Figure 4.40 demonstrates the principle of operation of this display on an oscilloscope in the x-y mode.

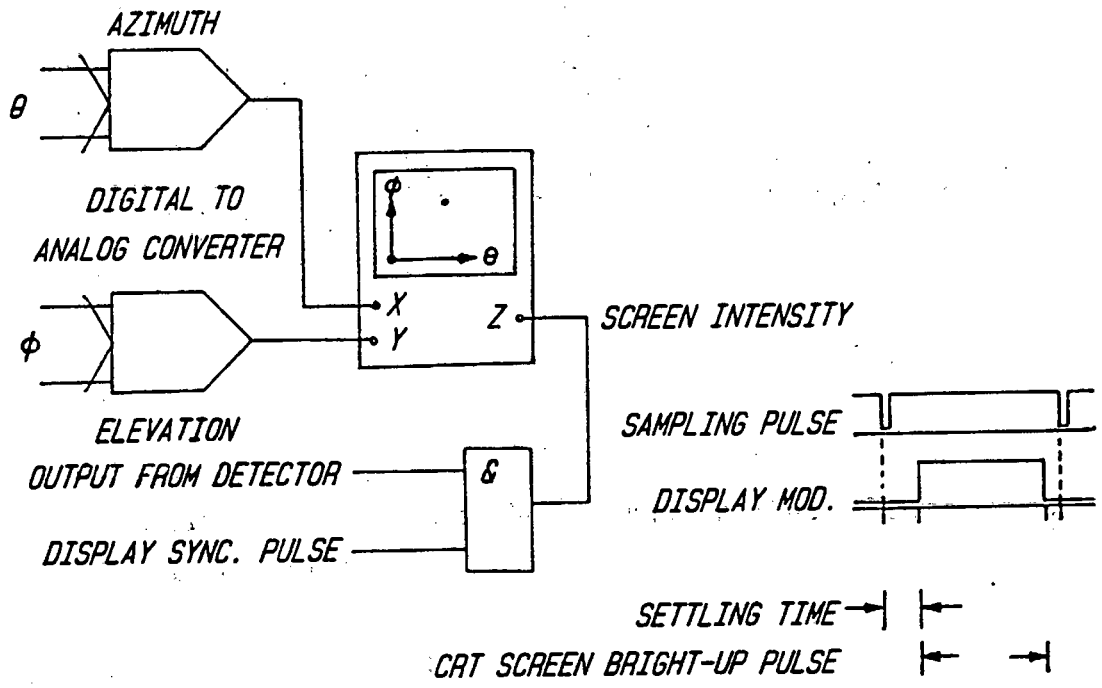

Figure 4.40: Schematic diagram of the implementation of a Θ-φ display.

The x and y display deflections are provided by the azimuth and elevation bearing measurements respectively, and the brightness control of the oscilloscope is modulated by a time signal, generated within the display circuit, which operates in conjunction with the detection thresholds.

Although the display succeeded in reproducing an image, it failed to display, simultaneously, the range information. As a result all the detected targets within the range gate were superimposed on the two dimensional screen in a somewhat confusing manner.

The image was found to be most decipherable for very short settings of the range gate where, by sweeping the gate delay, a moving crossectional slice through the sector was viewed, as shown in Figure 4.41.

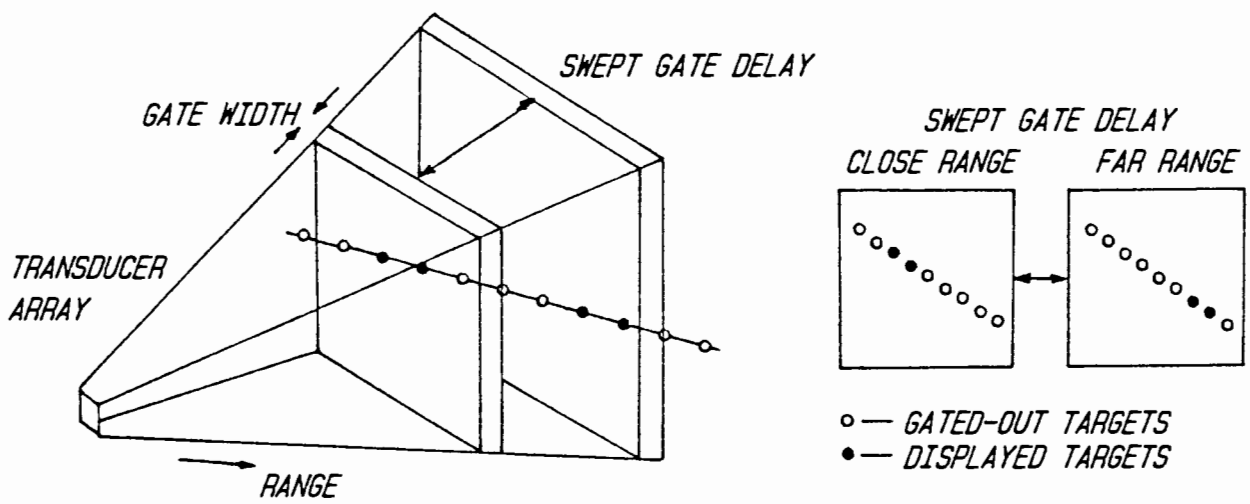

Figure 4.41: Operation of the Θ-φ display showing the effect of sweeping the delay of a short range gate.

(d) Vibrating Varifocal 3-D Display:

This method (Reference 24), in essence, involves the reflection of a two dimensional display by a thin film of mylar stretched over an airtight speaker cone. By driving the speaker and hence distorting the film to form alternately concave and convex mirror surfaces, the reflection of a Θ-φ display is "swept" into three dimensions. If the speaker drive were synchronised to the transmitting pulse, the range information would be available to the viewer as the apparent depth of the image.

The depth of this display is related to the radius of curvature of the (approximately) spherically distorted membrane. In practice, careful choice of the mirror-screen distance relative to the minimum radius of curvature for the mirror can produce a display with a depth of field in excess of one meter.

Figure 4.42 illustrates a varifocal-mirror display showing the image of a pointer for three different diaphram positions.

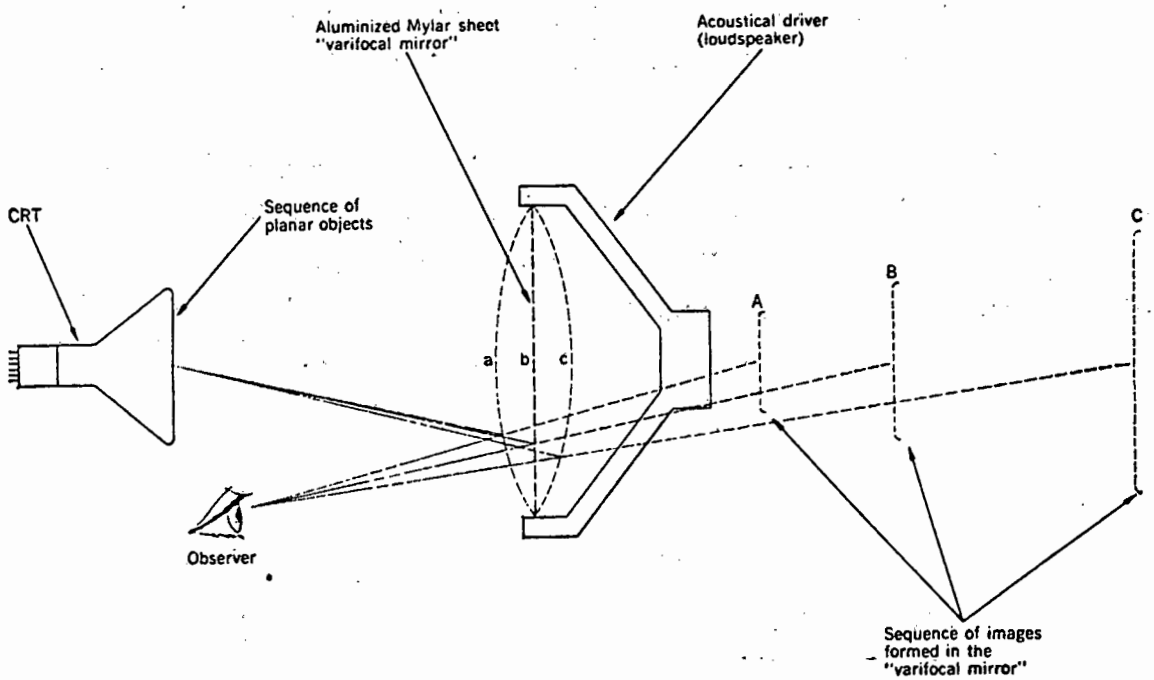

Figure 4.42: Operation of a varifocal-mirror display.

Despite the attractive features of this system it was not implemented on the 3-D sonar. However, from observation of an experimental setup demonstrating this device the following points were noted:

(i) This display technique suffers an inverted perspective, demonstrated in Figure 4.42, where an increase in depth implies an increasing image life. Although this is contrary to what one would normally expect, it could possible have been used to the sonars advantage by correcting for the increasing sector width subtended by an increasing range.

(ii) At pulse repetition rates of up to 30 Hz the display is very "loud", a disturbing phenomenon for the observer.

(iii) This display technique does not lend itself easily to the making of hard copies of results.

(e) Stereoscopic Displays

Like the vibrating varifocal mirror, this technique displays, in three dimensions, a Θ-ϕ display which in itself is only a two dimensional representation. A method of artificially generating a stereoscopic display was developed which conveys the additional dimension of range once again as the apparent image depth.

The stereoscopic effect results from a parallax between two images viewing an object from displaced positions. Figure 4.43 shows how the depth of objects A and B are captured on two images where the difference in depth is reconstructed from the small displacement A'B'. Thus, unlike the autostereoscopic vibrating varifocal mirror, the stereoscopic display requires two separate images.

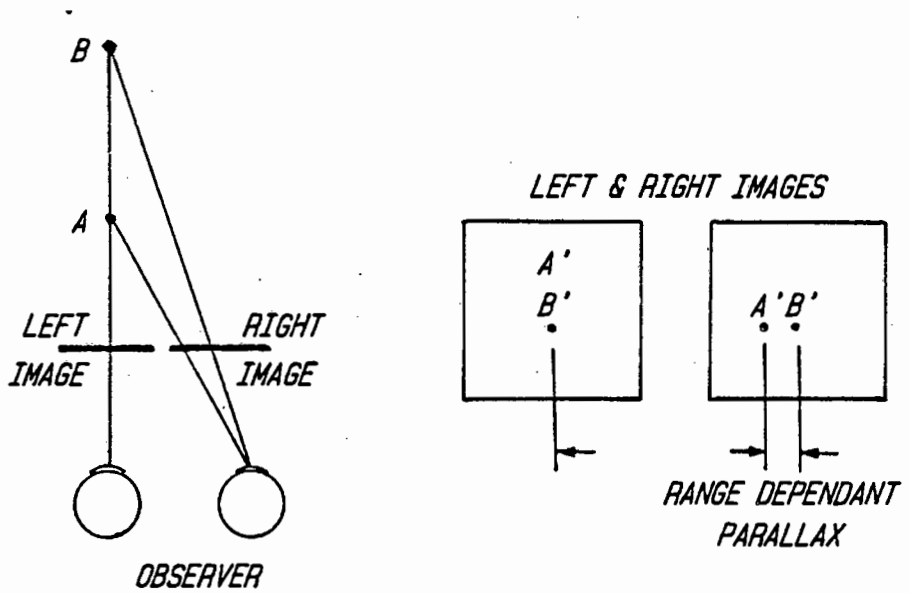

Figure 4.43: Diagram illustrating the principle of the stereoscopic effect.

Using the sonar system with a Θ-ϕ display the left hand image in Figure 4.44 is obtained. Stereoscopy is introduced by, in real time, displaying a second image in which the Θ coordinate of the displayed echoes are given a small lateral displacement which increases with time. A range dependant parallax is thus artificially created in the right hand image of Figure 4.44 thereby constituting a stereoscopic image pair.

The stereoscopic pair in Figure 4.44, when viewed through a stereoscope, reveals the three dimensionality of the spiral of targets receding into the page.

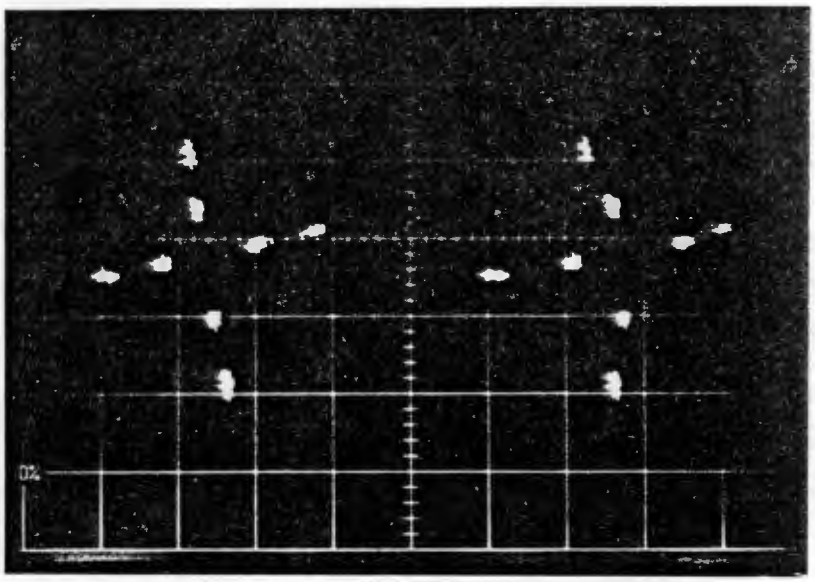

Figure 4.44: Photograph of a stereoscopic pair of images.

The stereoscopic display is implemented on a single beam oscilloscope by time multiplexing the screen dot deflections between the two images for each target echo. As before, the screen is blanked as the spot flies rapidly from one image to the other.

4.8.3. Implementation of the Stereoscopic Display

Figure 4.45 demonstrates the operation of the stereoscopic display generator by means of a schematic block diagram. The affect of the three internally generated timing waveforms are as follows:

(i) The linear ramp provides the time dependant parallax for the right hand image. Its slew rate is adjustable to allow enhancement of the range (depth) perception.

(ii) The DC offset prevents image overlap by providing an x-axis separation of the left and right images. This offset is also adjustable to compensate for the observers visual stereo accommodation.

(iii) The operation of the time multiplexing switches is clearly shown in the diagram. (The intrasample multiplexing time waveform is shown on a separate time axis since its operation is independent of range gating.)

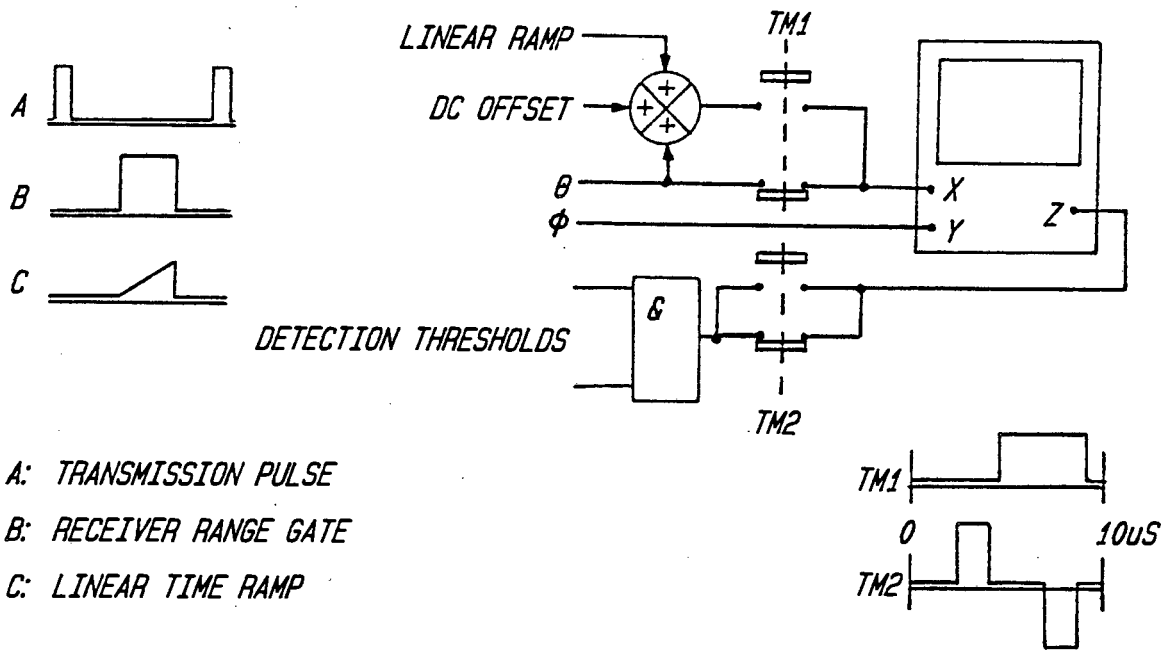

Figure 4.45: Schematic block diagram of the stereoscopic display generator.

4.8.4. Conclusion

Examples of stereoscopic images are shown, in Section 5, for targets designed to demonstrate the operation of the sonar systems as a whole. The display met, in every respect, the requirement to display all extracted information and succeeded in the task of transporting this information into a meaningful visual image.

An aspect of the displayed picture that is not immediately obvious from the above description, or the detailed circuit description in Appendix B, is the effect of visual integration. It should be bourne in mind that since this short range sonar has a high PRF, the display is updated at a rate of many hertz. (Analogous to screen persistence, visual memory has the effect of integrating sequentially displayed information.)

One is tempted to believe that a loss of target strength information would result from the binary nature of the screen intensity modulation and the phase-only operating principle of the sonar. This is not entirely so since, for strong targets, the regular detection and consistent "noise-free" bearing samples integrate in time to sharply defined bright highlights on the oscilloscope screen.

Likewise, weak targets appear as diffuse smudges which are distinct from random false detections by virtue of their stable three dimensional localisation.

Visual integration also serves to paint a composite picture in the presence of scintillating targets. Through this process, targets with overlapping echoes can be displayed simultaneously. This again emphasises that the limitations of this system are not as severe as they would first appear.

CHAPTER 5

RESULTS AND PROPOSALS FOR FUTURE WORK

5.1. Introduction

In this chapter, the performance of the system is evaluated and discussed for the experimental results obtained for two targets, namely:

A. A spiral of table tennis balls
B. A gravel bed.

5.2. Target A : A Spiral of Table Tennis Balls

A target was constructed that consisted of table tennis balls suspended in a spiral that decreased in radius with increasing range. A side elevation of the model is shown in Figure 5.1(a).

This model was constructed using a "cone" of nylon monofilaments connected from the rim of a bicycle wheel to a heavy mass at the apex. The table tennis balls were threaded on the monofilaments and the puncture holes sealed with epoxy.

The target was suspended vertically in a water tank and imaged from above. An optical photograph of the model, seen from the same position, is shown in Figure 5.1(b)

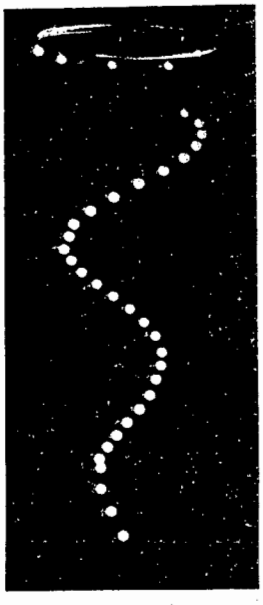

Figure 5.1(a): Photograph of the target A taken from a side view.

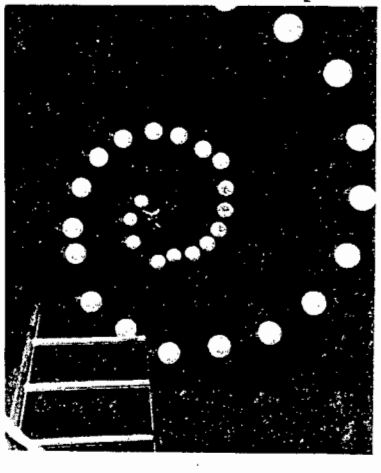

Figure 5.1(b): Photograph of the same target seen from above.

Using the 3-D imaging sonar the stereo image pair, shown in the photograph of the sonar display in Figure 5.2, was obtained. Apart from the omission, due to range gating, of some of the uppermost and three lowermost table tennis balls, there is an excellent correspondence with the optical photograph.

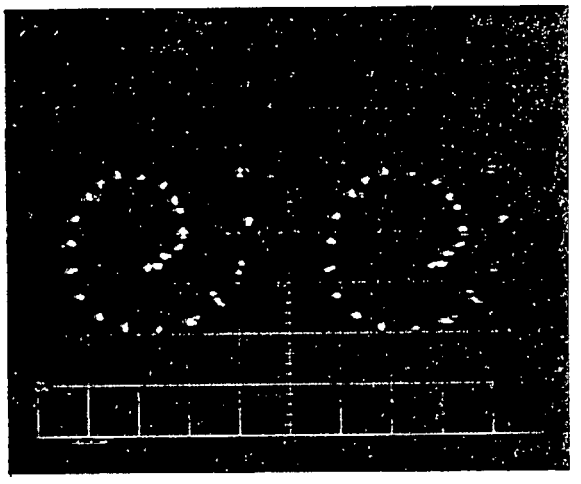

Figure 5.2: Displayed image of a spiral of table tennis balls.

The image produced in Figure 5.2 has a major advantage over conventional P.P.I. sonar displays in that it is "as the eye would see it" and is therefore easily interpreted. Viewed in a stereoscopic viewer, the spiral of table tennis balls are readily seen to recede into the distance.

5.3. Target B : A Gravel Bed

The aim of this test was to examine the performance of the system in situations which are less suited to the single wavefront criterion than an array of table tennis balls.

Figure 5.3 shows the experimental setup used to image a bed of gravel. The transducer array was mounted one metre above the bottom and angled to illuminate a "spot" of the smoothly racked gravel bed.

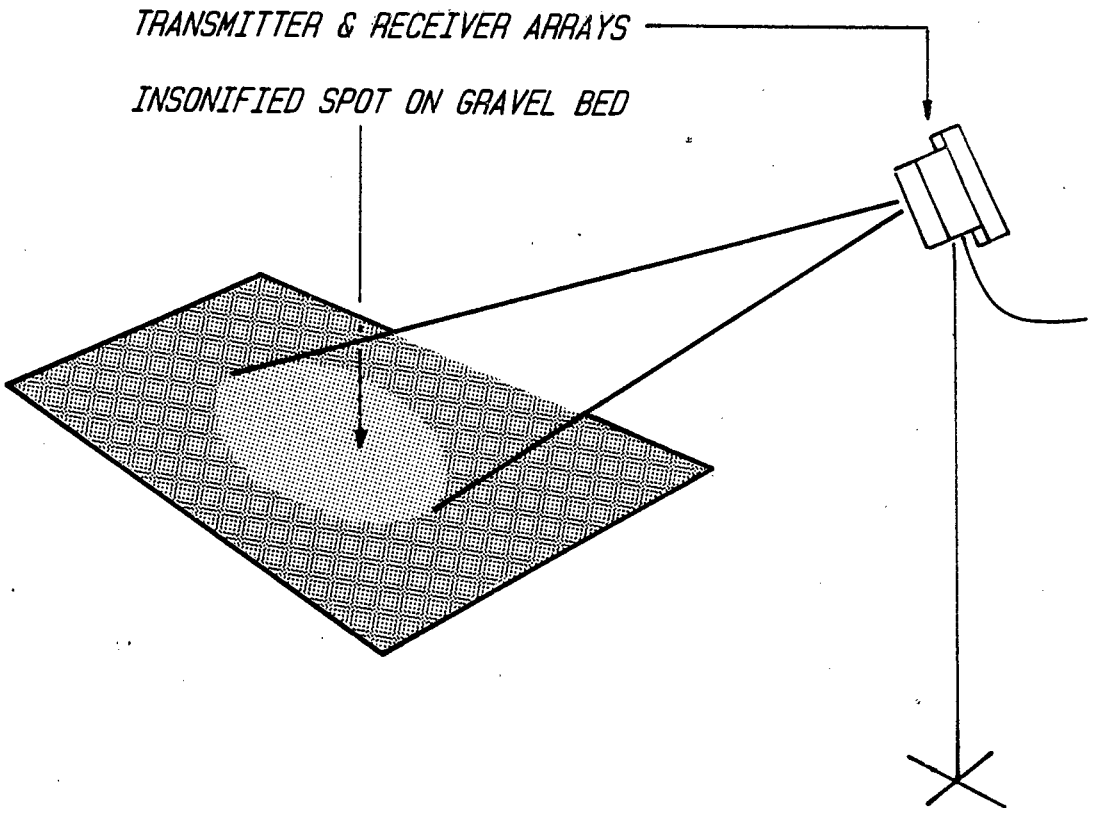

Figure 5.3: Experimental setup used to obtain images of a gravel bed.

Figure 5.4 shows an example of the image produced in which a flat granular surface is revealed. It will be noted that, in keeping with the single target requirement of the system, the gravel does, perhaps surprisingly, contain some dominant highlights which pass the threshold tests. (This occurs even though the gravel used in the experiment was graded.) Viewed stereoscopically, the flat topography of the gravel bed is apparent.

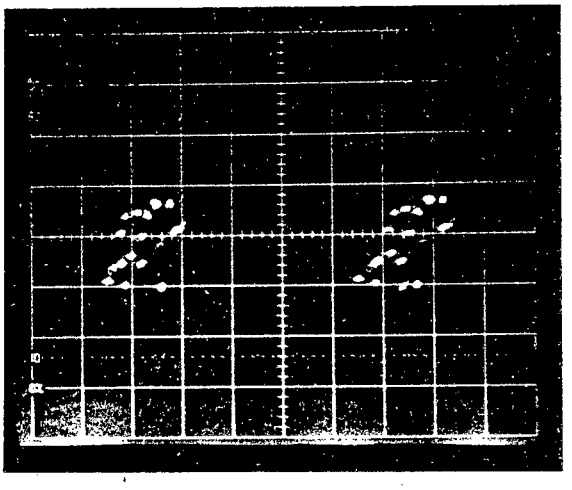

Figure 5.4: Sonar image of a bed of gravel.

The multiple target conditions occuring for this target presented an ideal opportunity to examine the effect of varying the phase error threshold. A sequence of pictures was taken while relaxing the phase threshold of the system.

Figure 5.5 shows the left-hand side of four images, each representing an integration of images over a period of 50 transmission pulses, for the various threshold setting.

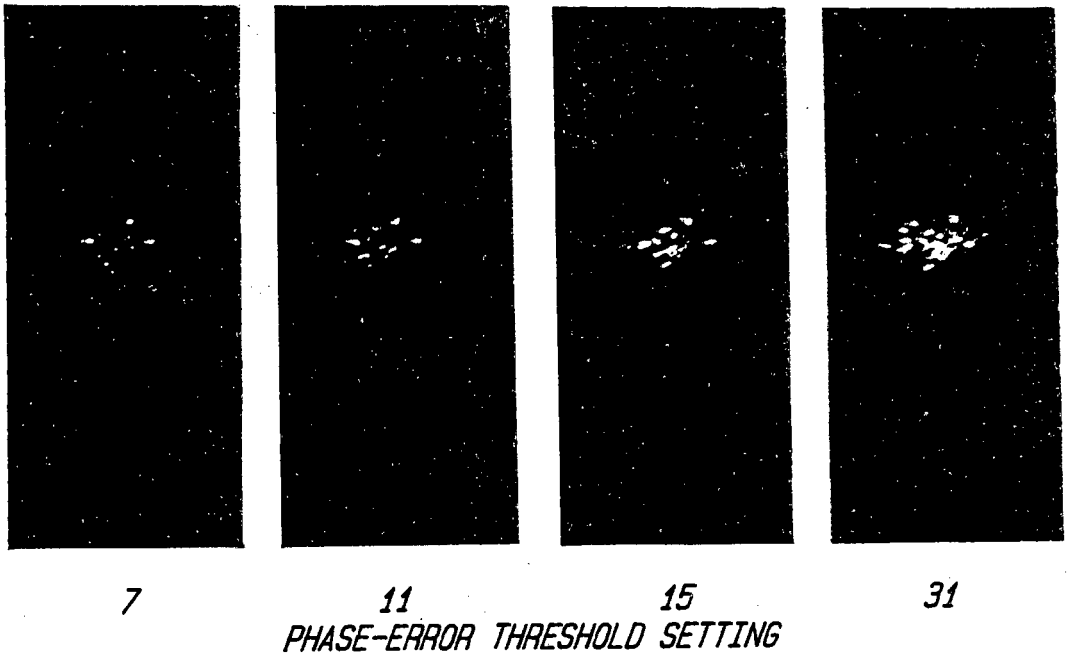

Figure 5.5: Images of a gravel bed showing the effect of varying the phase error threshold level.

In keeping with what one would expect, the images grow progressively noisier with decreased threshold stringency. This is indicated by the increased number of displayed samples and the increasing "fuzziness" of the displayed highlights.

5.4. Proposals for Future Work

The results obtained for the system exceeded expectations in almost every respect. There are however some aspects in the operation of the sonar that could be improved upon in future work.

It was demonstrated in Chapter 3 that the echo structure from immersed bodies, for high frequencies sound, is composed of discrete image pulses. The spread-out nature of these highlights gives rise to the probability that, at any range, only a single dominant echo source will be present.

As pointed out by Hudson (Reference 13), the probability of the required single target condition is increased by the fluctuation of target strengths occuring in underwater work. Variation in the echo strength arises from relative motion of target and sonar or disturbances of the acoustic field due to turbulence or surface scattering.

Such disturbances could be created by, for example, using multiple transmitter locations. If the transmitter transducer were either moved or various spatially distributed transmitters were operated in sequence, the resulting target fluctuations could lead to the display of even the weakest of overlapping echoes. In order to capture the time varying image produced by techniques exploiting target strength fluctuation an integrating display screen would have to be implemented. To this end, a memory map providing image integration and possibly more sophisticated signal processing could be envisaged.

Improvements, with the inevitable increased hardware complexity, would have to be balanced against the simplicity of the system achieved in its present state of development.

CHAPTER 6

CONCLUSION

A three dimensional imaging sonar system has been described with which stereoscopic pictures of targets have been obtained.

Details on the construction, evaluation and matching of the elements of the simple transducer array have been given. Low-noise preamplifier techniques have been examined and the results of the investigation are presented for assistance to future designers.

The phase-only principle of operation of this sonar has been introduced and the hard limiters and phase measuring hardware described, together with the system sequencing and synchronisation.

Signal detection is achieved by the simultaneous meeting of applied thresholds for array spatial variation, minimum signal to noise ratio and range gating. The small hard-wired data processor implementing detection on the two-axis phase samples is described along with the hardware required for amplitude threshold sampling.

Finally the concept of stereoscopic displays and the synthetic generation thereof was illustrated for the three dimensional sonar system.

Results obtained for water trials clearly demonstrate the viability of this simplified sonar. Since the system can only determine the angle of incidence of a single wavefromt at any time it is ideally suited to situations where there is a likelihood of no more than one dominant target echo in any range cell. An obvious application would be the imaging of fish shoals.

Theory on the formation of echoes for ultrasonic sound shows however that the limitations imposed by the required single target condition tend to be much less of a constraint than would initially be supposed. Due to the highlight composition of targets this system is, perhaps surprisingly, applicable to even complex target situations. For example, an image of a gravel bed has been obtained and reveals the surface topography.

LIST OF REFERENCES

1. Runciman, P., and Denbigh, P.N., "A three dimensional imaging sonar", Ultrasonics International 85, (1985), pp.300-305.

2. Dineen, G.P., and Reed, I.S., "An analysis of signal detection and location by digital methods", Trans. IRE IT-2, (1956), pp.29-35.

3. Tucker, D.G., "Underwater echo-ranging", J Brit. IRE 16, (1956), p.243.

4. Huggins, W.H., "A phase principle for complex frequency analysis and amplitude principles in signal processing", J. Acoust. Soc. Amer. 24, (1952), pp.582-589.

5. Middleton, D., and Huggins, W.H., " A comparison of the phase and amplitude principles in signal detection", Proc. Nat. Electron. Conf., Chicago, Ill.

6. Webb, G.D., Middleton, F.H., Gilbert, G, and Huggins, "A phase-filter applied to spectral phono-cardiography", IRE Conf. Instr. Atlanta, Ga. (Nov. 1955).

7. Piggot, M.T., Whitmarsh, D.G., and Brown, J.J. Jr., "Scanned line hydrophone method for determining angle of arrival of sound in water", J. Acoust. Soc. Amer. 34, (1962), pp.318-328.

8. Rudnick, P., "Small signal detection in the DIMUS array", J. Acoust. Soc. Amer. 32, (1960), pp.871-877.

9. Nairn, D., "Theoretical possibility of a digital sonar system", Proc. IERE Symp. Signal Processing Radar Sonar Directional Syst. (Jul. 1964).

10. Nairn, D., "Clipped digital technique for the sequential processing of sonar signals", J. Acoust. Soc. Amer. 44, (Nov. 1968), Vol. 5, p.1267.

11. Griffiths, J.W.R., and Creasey, D.J., "A digital sonar system", J. Soc. Instr., (Aug. 1966), Vol. 43, pp.534-535.

12. Creasey, D.J., and Braithwaite, H.B., "Experimental results of a sonar system with a digital processing unit", Applied Acoustics. 2, (1969), p.39.

13. Hudson, J.E., "Monte-Carlo simulation of an active sonar", The Radio and Electronic Engineer. 5, (Nov. 1970), Vol. 40, pp.265-271.

14. Freedman, A., "A mechanism of acoustic echo formation", Acoustica, (1962), Vol. 12, pp.10-21. also "The high frequency echo structure of some simply body shapes", Acoustica, (1962), Vol. 12, pp.61-70.

15. Urick, R.J., "Principles of underwater sound (3rd ed)". McGraw-Hill, (1983).

16. Kinsler, L.E., Frey, A.R., Coppens, A.B., and Sanders, J.V., "Fundamentals of Acoustics (3rd Ed)", John Wiley & Sons, (1982), pp.344-369.

17. Mason , W.P., "Piezo-electric crystals and their application to ultrasonics", van Nostrand, (1949). also "Physical Acoustics IA", Academic Press, (1964).

18. Roy, S., "Minimisation of mutual coupling in transducer elements", SAAI Congress on Acoustics, (Oct. 1985), Vol. 1.

19. Mellen, R.H., "Thermal-noise limit in the detection of underwater acoustic signals", J. Acoust. Soc. Am. 24, (1952), p.478.

20. Texas Instruments, "The transistor and diode data book". (1973).

21. Horowitz, P., and Hill, W., "The art of electronics", Cambridge University Press, (1980), pp.286-299.

22. Green, J., "An electro-optic inshore survey aid", M.Sc. Thesis, University of Cape Town, (Jun. 1980).

23. Denbigh, P.N., "A bathymetric side-scan sonar", Ultrasonics International 79, (1979), pp.321-326.

24. Rawson, E.G., "Vibrating varifocal mirrors for 3-D imaging", IEEE spectrum, (Sep. 1969), pp.37-43.

25. Millman, J., "Microelectronics : Digital and analog circuits and systems", McGraw-Hill, (1979).

APPENDIX A

THE ECHO FORMATION FOR A BRICK

In this section the high frequency echo structure of the brick, used as a target in Chapter 3, is evaluated.

Figure A.1 shows the front elevation of the target as seen by the sound source. The total area of projection towards the source is seen to be contributed to by three connected lamina.

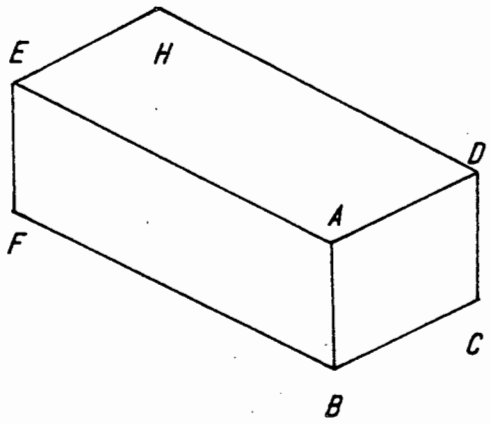

Figure A.1: Front view of the brick showing the three lamina.

Figure A.2 illustrates the echo formation for the brick insonified by a short pulse of high frequency sound, the results of which are summarised in Table A.1.

TABLE A.1.

Image Pulse	Range Relative to Point A [mm]	$\left\lvert \frac{E\, r_m^2}{M_i} \right\rvert$ [x 10^{-4}]	Relative Image Pulse $20 \log [\frac{E_i}{E_1}]$ [dB]
E1	0	1,0	0
E2	35	0,75	-2.5
E3	60	0.63	-4.0
E4	95	0,38	-8.5
E5	135	0,63	-4.0
E6	169	0,38	-8.5
E7	195	0,24	-12

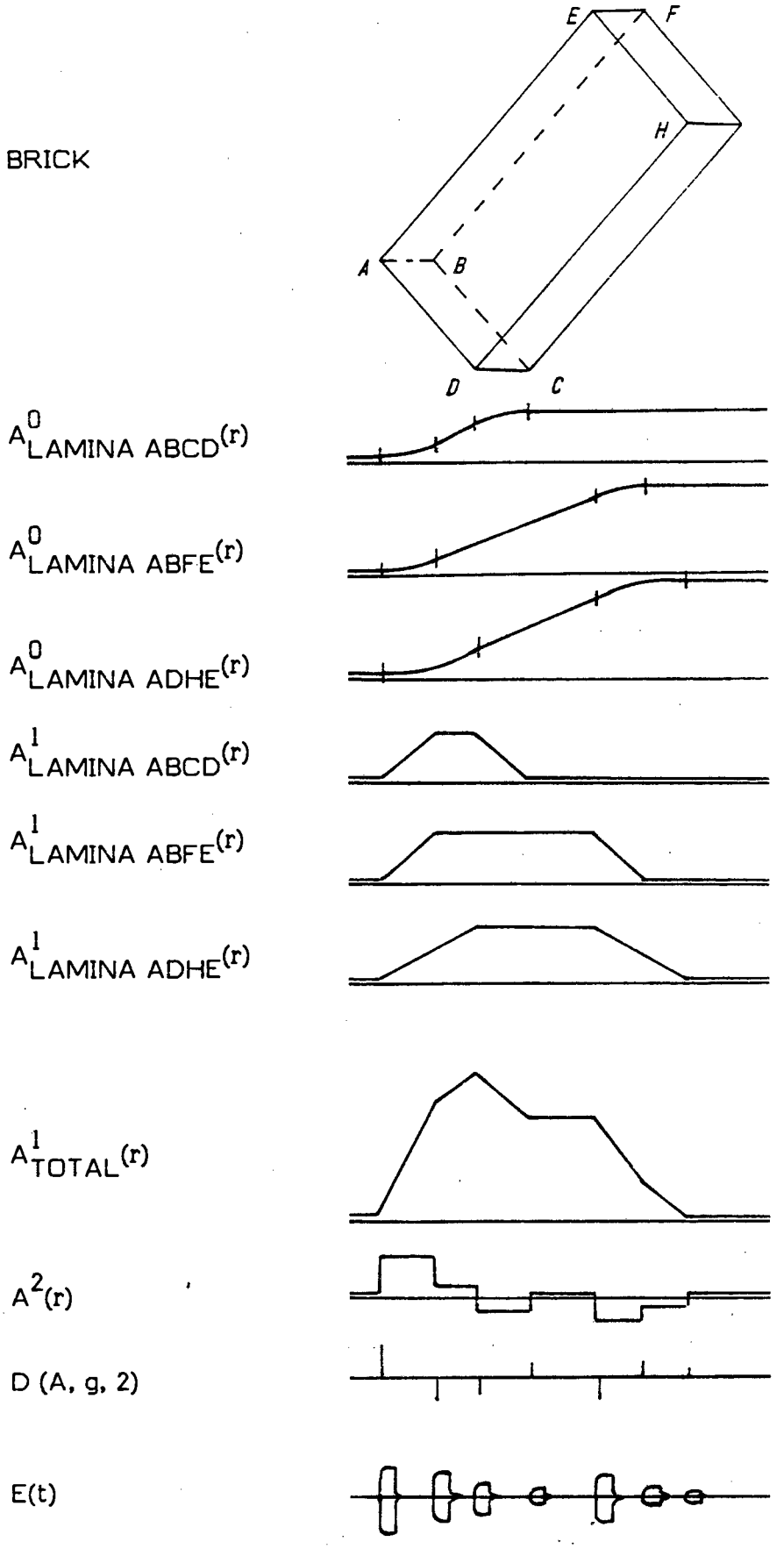

Figure A.2: Echo formation for an air-filled foam brick.

APPENDIX B

CIRCUITRY

B.1. INTRODUCTION

This appendix deals with the circuitry that was introduced in Chapter 4 where the implementation of the system was examined.

Since for most subsystems, the operational requirements, synchronisation and alternate methods of approach have already been discussed, it leaves only the detailed circuit diagram and circuit operation to be presented.

B.2. PREAMPLIFIER AND ZERO-CROSSING DETECTOR

Figure B.1 shows the circuit diagram of the preamplifier and hard limiter for a single channel of which four identical such circuits were made on separate boards.

Extreme care was taken in the layout and design of each board to minimise noise and unwanted feedback due to the large overall voltage gain and small signal level present at its input. For example, the top side of the double-sided circuit board is left unetched to provide a continuous earth-plane. Further precautions taken in this regard include power supply regulation and decoupling for every element of the circuit on each board.

The front-end amplifier has been dealt with, in detail, in Section 4.3 and as such needs no further explanation save to mention that its output is buffered by a transistor in an emitter follower configuration. Besides providing a low impedance source to the subsequent amplifier, the front-end voltage gain roll-off at high frequencies, and the AC coupling of the buffer, combine to effect a bandpass function to the first stage gain.

The next element, the MC1590G, is a standard RF/IF integrated-circuit amplifier which provides a large signal gain over a wide frequency band. The current passing into pin 2 controls the gain reduction of the amplifier and, though normally used as an AGC control, is used here to trim the gain of the amplifiers to provide equal output for all four channels at this point.

The output of this amplifier is conveniently provided by a non-saturating open-collector transistor where the choice of load impedance sets the voltage gain characteristics of the stage. This device thus offers not only an easily implemented

active bandpass filter by means of a parallel RLC tuned circuit, but also lends itself to symmetrical clipping by clamping the voltage swing on the inductor with diodes. (Adjustment of the potcore's airgap allows frequency tuning and phase balancing of the amplifiers.)

The actual choice of component values for the tank circuit is determined by not only the filter centre frequency, but also the bandwidth and voltage gain required for this device.

The resistance, at centre frequency, is required to be approximately 15 kΩ to ensure a voltage gain of 45 dB. However, since the voltage at pin 6 of the amplifier must equal the supply voltage (for symmetrical clipping), this load resistance is provided by the parallel combination of the capacitively coupled biasing resistors of the output buffer.

Given the damping resistance of the RLC circuit and the required fractional bandwidth of the filter, the value of the inductor can be calculated (and hence the capacitance value) as follows:

$$R = \left(\frac{1}{27} + \frac{1}{33}\right)^{-1} \qquad (k\Omega)$$

$$= 14.9\ k\Omega.$$

The fractional bandwidth required is 10%, thus the quality factor, Q, is:

$$Q = \left(\frac{1}{\text{Fractional bandwidth}}\right)$$

$$= 10$$

For a parallel RLC circuit,

$$Q = \frac{R}{\omega_0 L}$$

thus

$$L = \frac{14\,900}{2 \times \pi \times 490\,000 \times 10}$$

$$= 0.48\ mH.$$

The value of the capacitor is then:

$$C = \frac{1}{L \omega_0^2}$$

$$= 220 \text{ pF}.$$

Finally, hard limiting was achieved with the TBA120S, an integral FM circuit which includes an IF strip containing eight cascaded limiting amplification stages. The output of this device is level shifted and made compatible to TTL logic voltage levels by a fast comparator, the LM710C.

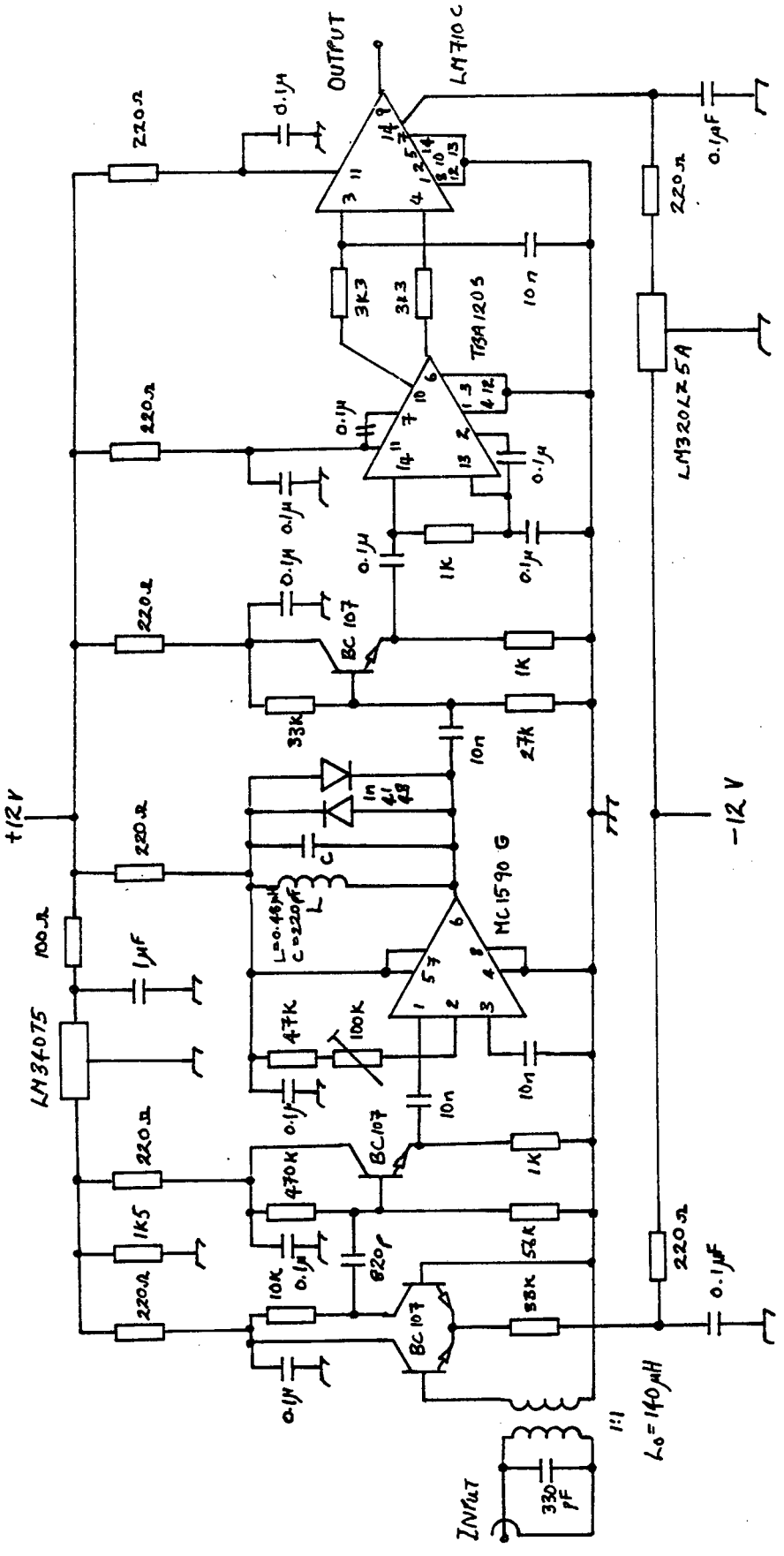

Figure B.1: Circuit diagram of the preamplifier and hard limiter.

B.3. SYSTEM SEQUENCER

Figure B.3 shows the circuit diagram of the system sequencer which fulfills two separate tasks, that of system synchronisation and system timing.

The system clock is provided by a 16 MHz square-wave signal generator. The sequencer conditions this input to a TTL compatible clock signal with a Schmitt trigger inverter which drives a further hierarchy of inverters to increase the fanout. The sampling pulses are generated by frequency dividing the system clock by a factor of 160, thus initiating the acquisition of a sample every 10 μs. (The negative-going sampling pulses are denoted by $\bar{s}$ throughout the system hardware.)

The system timing generator was implemented using a hard-wired digital design technique known as an algorithm state machine (ASM) (Reference 25). This method requires that the controlling algorithm of the device be written first step-wise, then symbol-wise before implementing the algorithm with J-K flip-flop hardware.

The controlling algorithm for the system timing generator is divided into two separate parts:

A. The interpulse and transmitting pulse period generator.
B. The receiver gate delay and width generator.

A. <u>The interpulse and transmitting pulse period generator</u>

ALGORITHM

(1) Trigger monostable timers T1 and TX and proceed to next step when T1 ends.

(2) Trigger monostable timer T2 and proceed to first step when T2 ends.

ASM TRANSLATABLE ALGORITHM

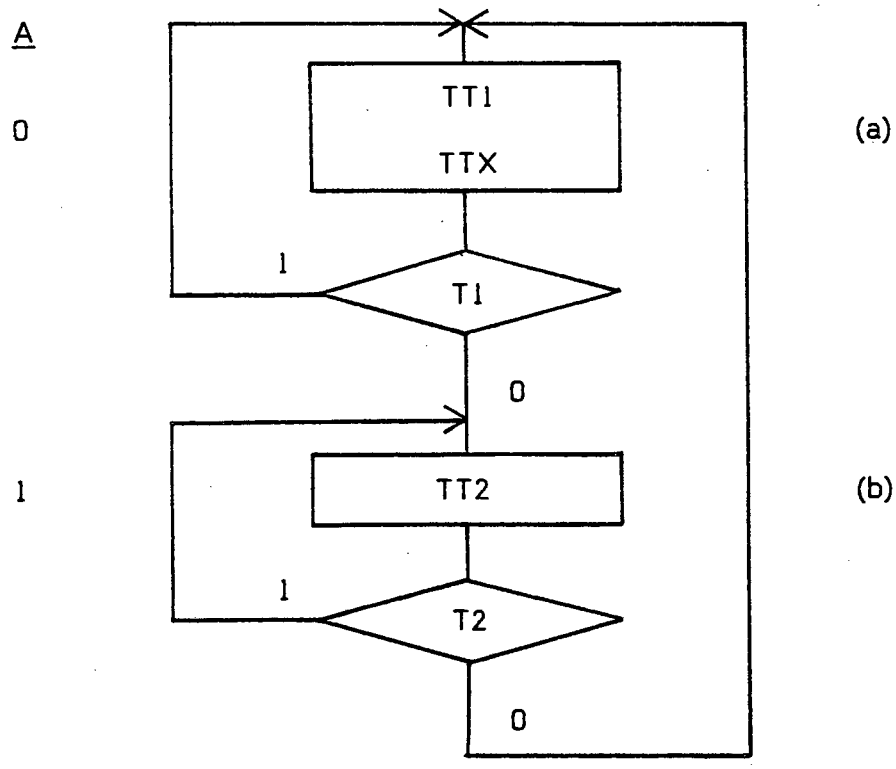

T1 Monostable timer 1 output

TT1 Trigger monostable timer 1

(These symbols are used for all four timers)

TX Transmitting pulse period timer output

(which is used to gate a 490 kHz sine-wave signal generator)

TTX Trigger monostable providing TX

ASM DESIGN

Using the ASM design procedure, the above algorithm is translated to a J-K flip-flop design as follows:

State assignment

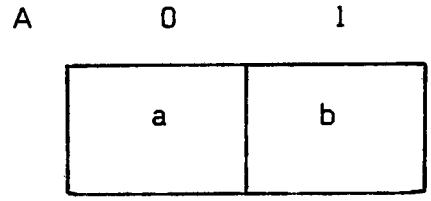

$a = \bar{A}$

$b = A$

State variable

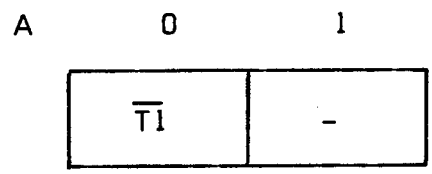

$J_A = \overline{T1}$ $K_A = \overline{T2}$

The algorithm of the interpulse and transmitting pulse period generator then translates to the circuit shown in Figure B.2.

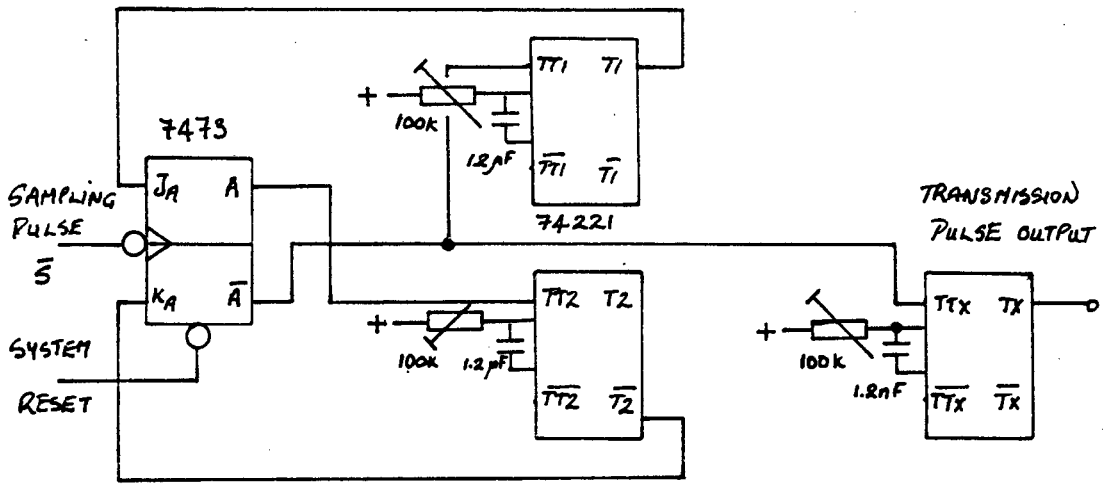

Figure B.2: Circuit diagram of the interpulse and transmitting pulse period generator.

In this circuit, the logical "clock" is provided by the sampling pulses ($\bar{s}$) thereby synchronising the operation of this device to the sampling instants.

B. The receiver gate delay and width generator

ALGORITHM

(1) Using the negative-edge trigger of the monostable timers T3 and T4, trigger timer T3 at the end of the transmitting pulse period and proceed to next step.

(2) Trigger monostable timer T4 when T3 ends and then proceed to the first step.

ASM TRANSLATABLE ALGORITHM AND DESIGN

It was chosen not to present these design phases since they closely resemble the previous timing generator.

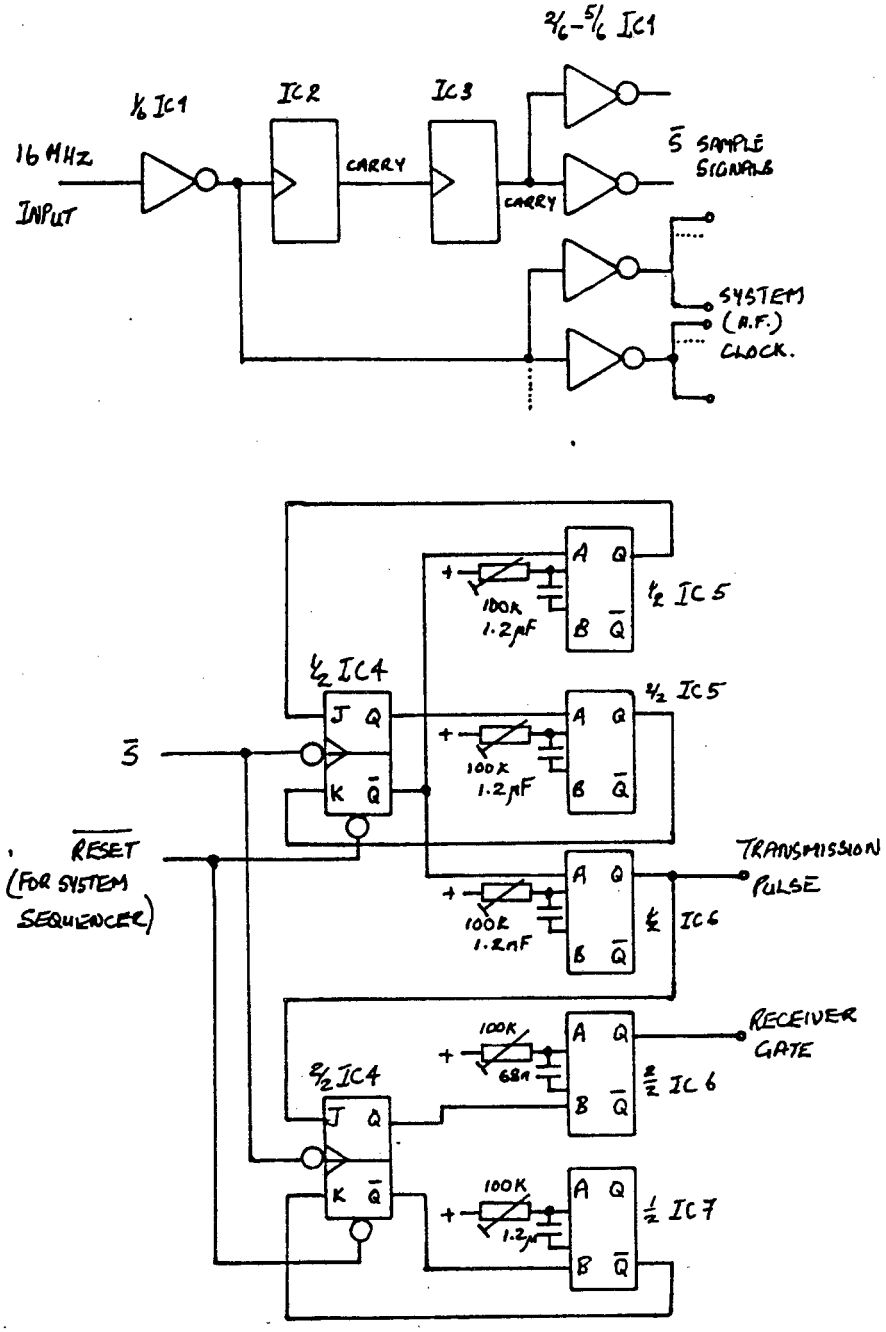

IC	SERIAL #
1	S7414
2	LS74163
3	LS74162
4	LS7473
5	LS74221
6	LS74221
7	LS74221

Figure B.3: Circuit diagram of the system sequencer.

B.4. DIGITAL PHASE METER

Figure B.4 shows the circuit diagram of the digital phase meter. This circuit consists of phase measuring hardware under the control of a hard-wired digital controller. The operation of the phase measuring circuit has been dealt with, in detail in Section 4.5, and therefore warrants no further description.

The controller consists of two independent devices, namely:

A. The sample controller.
B. The phase-measurement controller.

These controllers were implemented using the ASM design technique. (The operation of the phase meter control logic becomes self-evident in the design procedure detailed below.)

A. Sample controller routine

ALGORITHM

(1) Proceed to next step when a sample pulse, from the system sequencer, sets the sample latch.

(2) Reset the sample latch, reset the receiver cycle-counter and reset the delay logic.

(3) Maintain the reset commands of the previous step and load the phase count into the phase register.

(4) Set the receiver cycle-counter latch and clear the phase counters, then proceed to step (1).

B. Phase-measurement controller

(1) Stop the phase-counter until the receiver cycle-counter latch is set.

(2) Reset the receiver cycle-counter latch.

(3) Same as (2).

(4) Proceed to step (1).

Before continuing with the design, the choice of logical "clocks" for each controller should be pointed out.

Both of these controllers are sequential (synchronous) logic devices requiring a "clock" pulse in order to proceed from one step to the next. In the case of the sample controller, the 16 MHz system clock is used allowing a rapid restoring of the phase measuring routine after saving the previous phase sample at the sampling instant.

However, in the case of phase-measurement controller, the hard-limited signal from one receiver is used. This in effect acts as a received cycle counter, allowing only three duty cycle periods to contribute to the total phase/delay count.

ASM TRANSLATABLE ALGORITHM

A. Sample controller routine

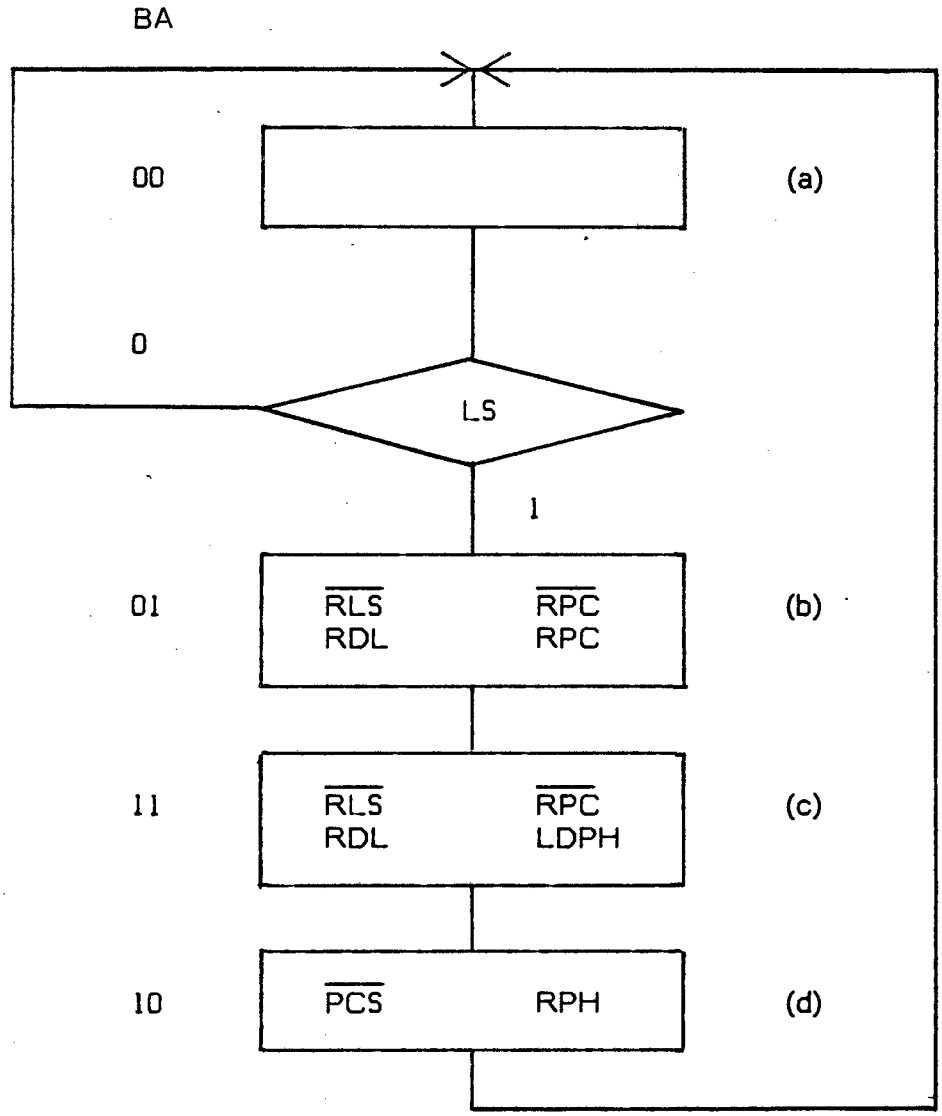

LS	Sample latch output
RLS	Reset the sample latch
RPC	Reset the receiver cycle-counter
RDL	Reset the delay logic
LDPH	Load the phase count into the phase register
PCS	Set the receiver cycle-counter latch
RPH	Reset the phase counters.

B. Phase-measurement controller routine

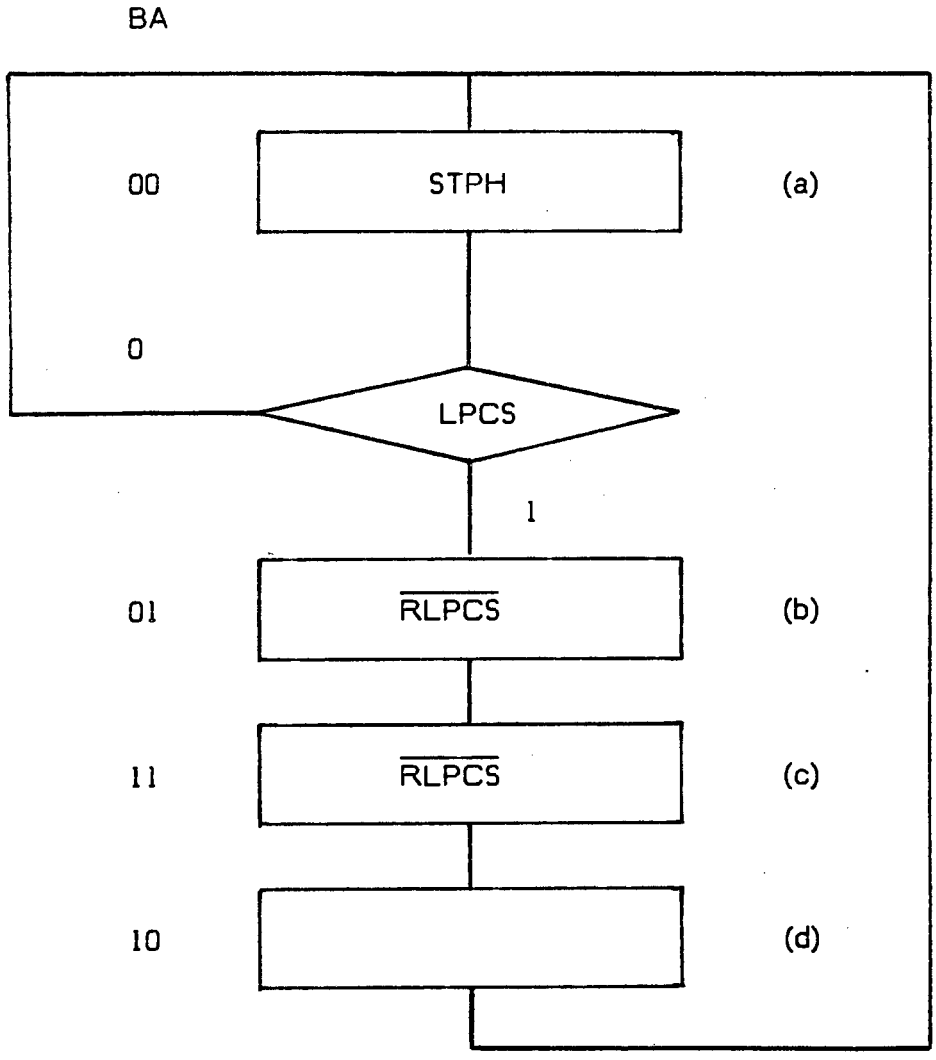

STPH Stop the phase-counter

LPCS Receiver cycle-counter latch output

RLPCS Reset the receiver cycle-counter latch.

ASM DESIGN

Using the ASM design procedure, the above algorithms can be translated to J-K flip-flop hardware as shown in Appendix B.3. Since both algorithms are of the same form, only the sample controller design will be presented here.

State assignment

A / B	0	1
0	a	b
1	d	c

$a = A.B$

$b = A.\bar{B}$

$c = \bar{A}.\bar{B}$

$d = \bar{A}.B$

State variable

A / B	0	1
0	LS	-
1	0	-

A / B	0	1
0	-	0
1	-	1

$J_A = LS.\bar{B}$

$= \overline{\overline{LS}+B}$

$K_A = B$

State variable

A / B	0	1
0	0	1
1	-	-

A / B	0	1
0	-	-
1	1	0

$J_B = A$

$K_B = \bar{A}$

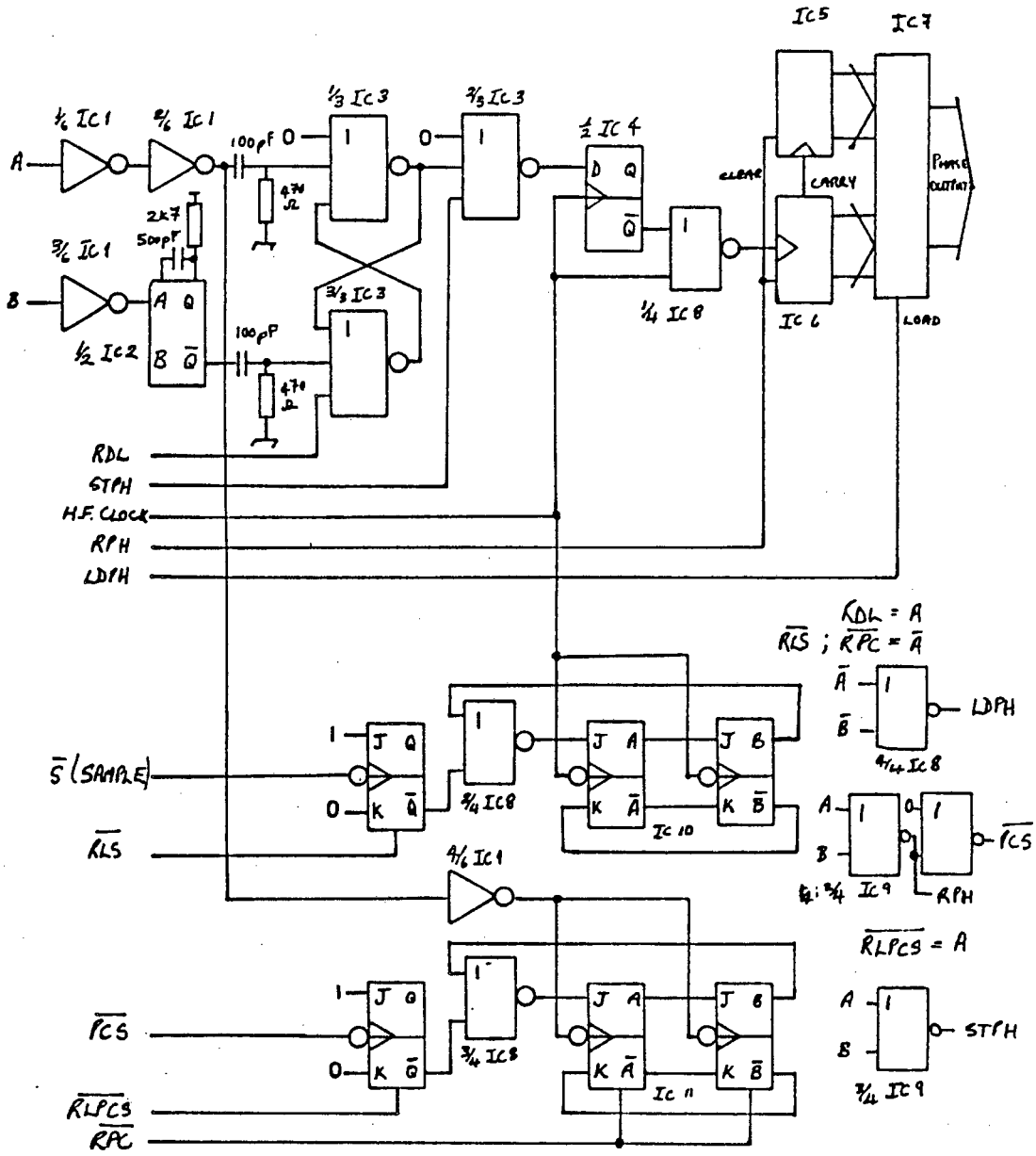

IC	SERIAL #
1	S7414
2	LS74221
3	LS7427
4	LS7474
5	LS74163
6	LS74163
7	LS74377
8	LS7402
9	LS7402
10	LS7473
11	LS7473

Figure B.4: Circuit diagram of the digital phase meter.

B.5. DATA PROCESSOR

Figure B.5 shows the circuit diagram of the data processor which consists of two identical boards. The operation of each of these boards can be summarised as follows:

(i) The output of this circuit can be directly expressed as a logical combination of its inputs and therefore requires no controlling circuitry.

(ii) The phase samples present at the input to each board are in the form of two latched seven-bit binary words.

(iii) Provision is made for the addition, to one phase word, of a constant offset.

(iv) This offset is a four-bit binary word, externally input by switch settings, which is added to the least significant bits of the latched phase sample.

(v) The two phase words are added and the sum output to the display generator where it provides a screen deflection proportional to the average bearing of the sample pair.

(vi) At the same time, the absolute value of the difference between the phase words is compared to an error threshold quantity. (This maximum allowable phase-difference error threshold is externally entered by switch setting.)

(vii) Should the difference in phase samples be less than the applied threshold, then a detection bit is set which is output for subsequent signal detection.

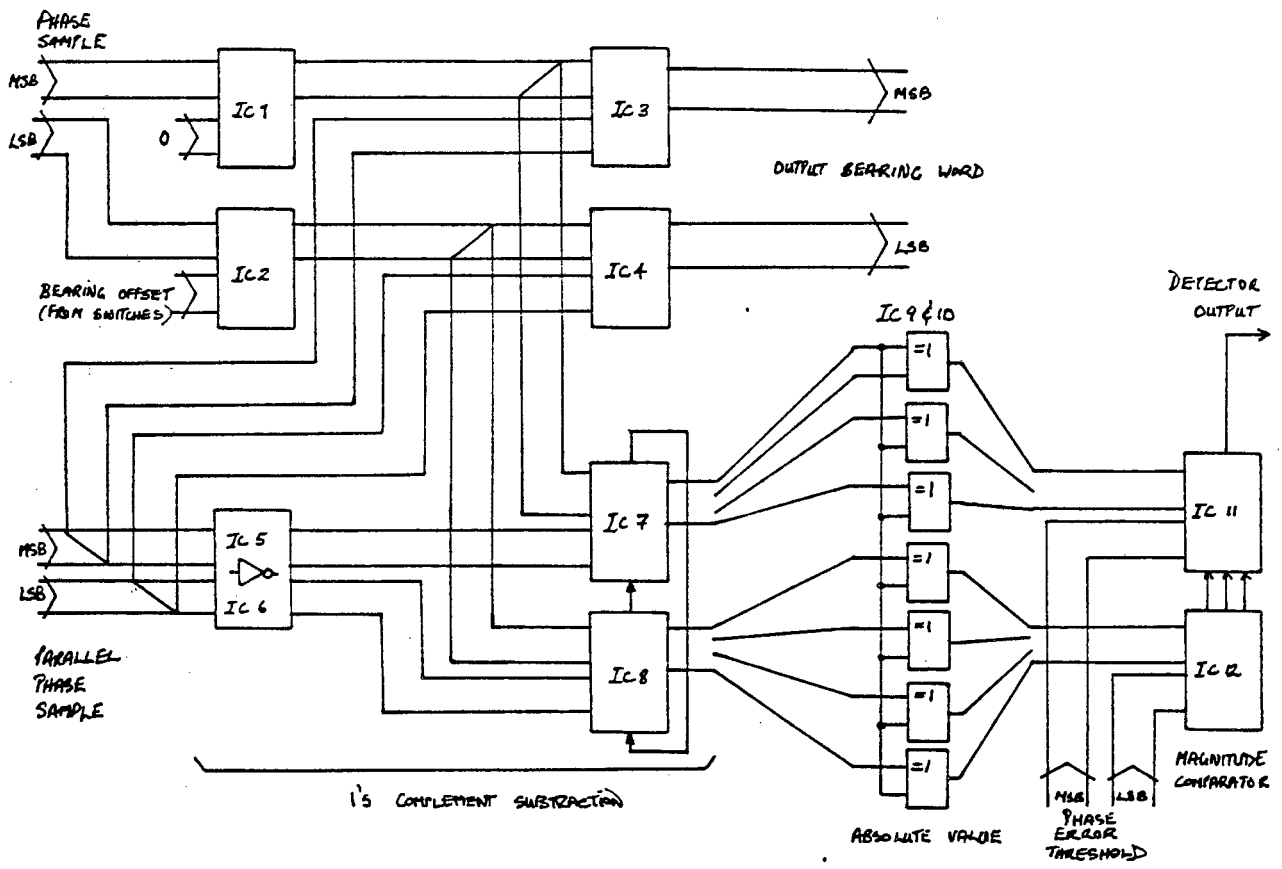

IC	SERIAL #
1, 2, 3, 4, 7, 8	LS7483
5, 6	LS7404
9, 10	LS7486
11, 12	LS7485

Figure B.5: Circuit diagram of the data processor.

B.6. AMPLITUDE THRESHOLD DETECTOR

Figure B.6 shows the circuit diagram of the amplitude theshold detector.

The amplitude of the received signal is compared, after linear amplification and envelope detection, with a preset voltage level. The output of the comparator is then sampled, first at the half-interval moment, and then resampled at the sampling instant, thus effectively delaying the output of the amplitude threshold detector to coincide with the display of the extracted phase samples.

Implemented on the same circuit board is the logical AND'ing of all the detection threshold outputs. The output of this gate, by ensuring that all the threshold conditions are simultaneously met, represents the overall signal detection for the system and is made available to the display generator for subsequent screen modulation.

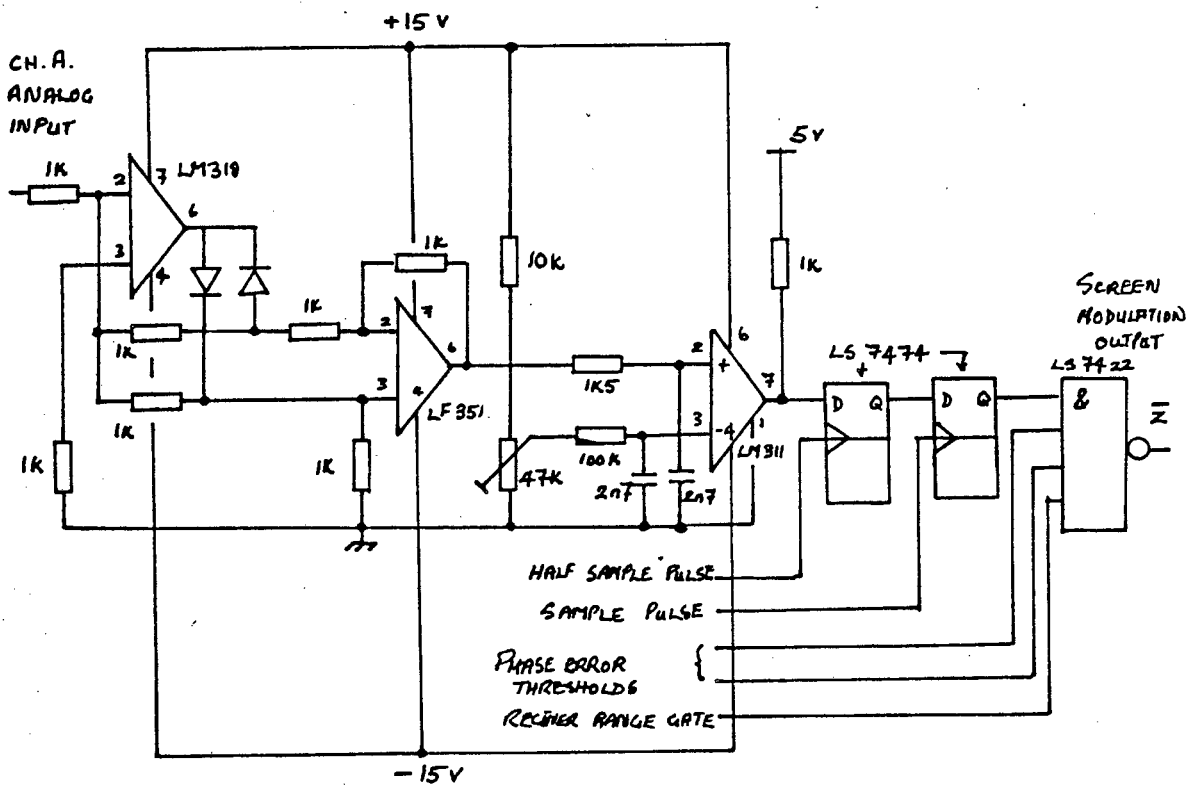

Figure B.6: Circuit diagram of the amplitude threshold detector.

B.7. DISPLAY GENERATOR

Figure B.7 shows the circuit diagram of the stereo display generator. The principle of this digitally realised circuit, demonstrated in Figure 4.45, can be summarised as follows:

(i) This circuit operates only on the azimuth part of the bearing samples.

(ii) Its function is to synthetically generate a second bearing sample that, when displayed with the measured sample on a θ-ϕ display, will constitute a stereo image pair.

(iii) The X-deflection of the display is time multiplex between the two azimuth values for each bearing sample.

(iv) The image separation is externally input by switches which, while the receiver gate signal is low, is repeatedly loaded into a register.

(v) When the receiver gate signal goes high, the contents of register are incremented, by an amount preset by switches, at every sampling instant thus providing a range dependant parallax for the right-hand image.

(vi) This combined parallax and image separation offset is multiplexed with a zero offset, and alternately added to the measured azimuth bearing thus producing two dots for each sample.

(vii) Cascaded monostable timers provide the multiplex control signal and screen bright-up pulses which allow settling time for the digital-to-analogue voltage converters.

(viii) The final screen modulation is determined by AND'ing the bright-up pulses with the detection signal.

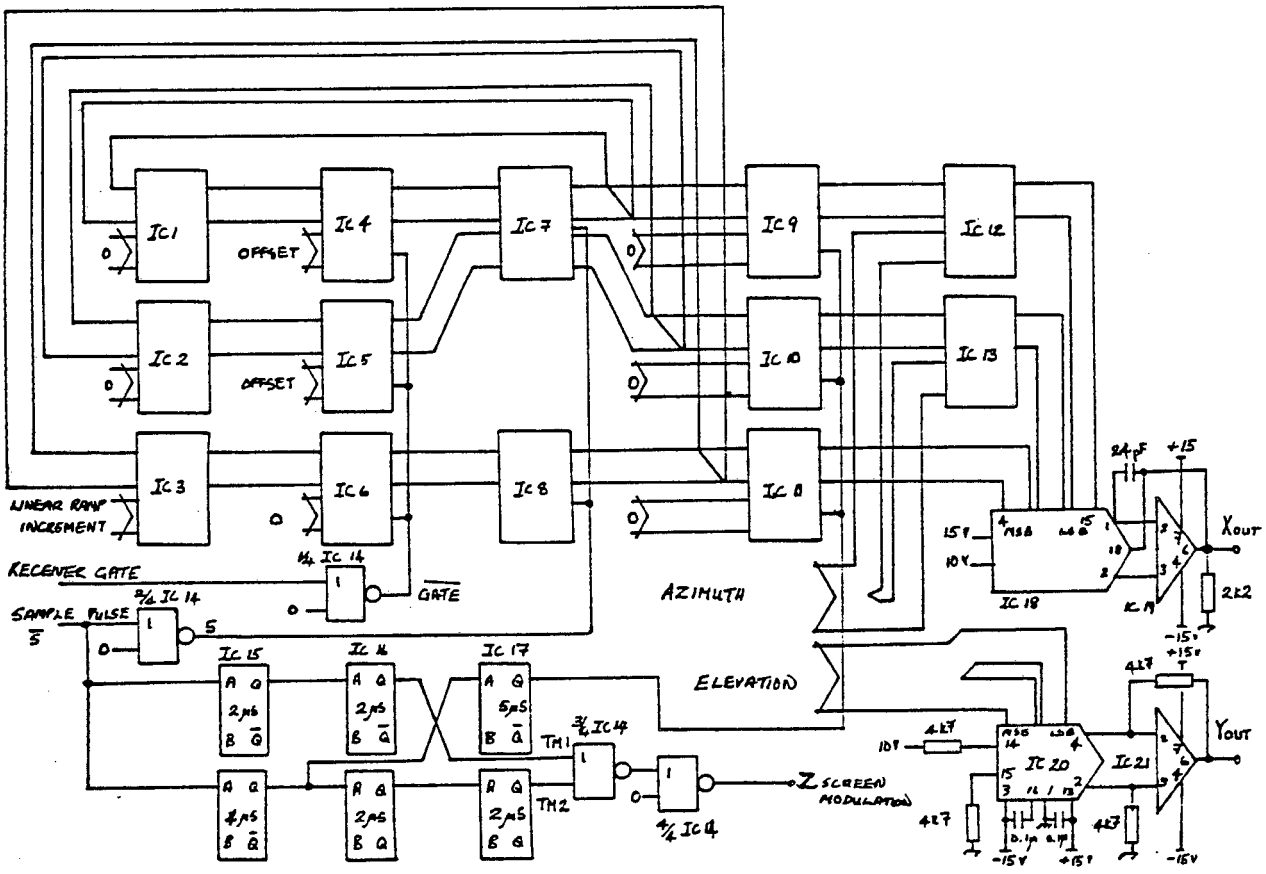

IC	IC SERIAL#
1, 2, 3, 12, 13	LS7483
4, 5, 6, 9, 10, 11	LS74157
7, 8	LS74377
15, 16, 17	LS74221
14	LS7402
18	DAC 1220 (12 bit)
20	DAC 0800 (8 bit)
19, 21	LF351

Figure B.7: Circuit diagram of the display generator.